

UNIVERSIDADE FEDERAL DO ABC
Programa de Pós-Graduação em Nanociências e Materiais
Avançados

Alexandre Olivieri Kraus

VACÂNCIA E EFEITOS DE TENSÃO
BIAXIAL EM FILMES FINOS DE NaNbO_3 :
UM ESTUDO DE PRIMEIROS PRINCÍPIOS

Santo André

2021

Alexandre Olivieri Kraus

VACÂNCIA E EFEITOS DE TENSÃO BIAxIAL EM FILMES FINOS DE NaNbO_3 : UM ESTUDO DE PRIMEIROS PRINCÍPIOS

Dissertação apresentada ao curso de pós-graduação em Nanociências e Materiais Avançados da Universidade Federal do ABC como requisito parcial à obtenção do título de Mestre em Nanociências e Materiais Avançados. Grande Área: Ciências Exatas e da Terra. Área de Avaliação: Astronomia / Física. Subárea: Física. Especialidade: Física Da Matéria Condensada.

Orientador: Prof. Dr. Jeverson Teodoro Arantes Jr.

Santo André

2021

Sistema de Bibliotecas da Universidade Federal do ABC
Elaborada pelo Sistema de Geração de Ficha Catalográfica da UFABC
com os dados fornecidos pelo(a) autor(a).

Kraus, Alexandre Olivieri

VACÂNCIA E EFEITOS DE TENSÃO BIAxIAL EM FILMES FINOS DE
NaNbO₃ : UM ESTUDO DE PRIMEIROS PRINCÍPIOS / Alexandre Olivieri
Kraus. — 2021.

90 fls. : il.

Orientador: Jeverson Teodoro Arantes Junior

Dissertação (Mestrado) — Universidade Federal do ABC, Programa de Pós-Graduação
em Nanociências e Materiais Avançados, Santo André, 2021.

1. Perovskitas. 2. Fotocatálise. 3. Primeiros princípios. 4. Vacâncias. 5. Filmes
finos. I. Arantes Junior, Jeverson Teodoro. II. Programa de Pós-Graduação em
Nanociências e Materiais Avançados, 2021. III. Título.

Este exemplar foi revisado e alterado em relação à versão original, de acordo com as observações levantadas pela banca examinadora no dia da defesa, sob responsabilidade única do(a) autor(a) e com a anuência do(a) (co)orientador(a).

Santo André , 2 de Agosto de 2021 .

Alexandre Olivieri Kraus Alexandre Oliu
Nome completo e Assinatura do(a) autor(a)

Jerson Peres
Nome completo e Assinatura do(a) (co)orientador(a)




MINISTÉRIO DA EDUCAÇÃO


Fundação Universidade Federal do ABC

Avenida dos Estados, 5001 – Bairro Santa Terezinha – Santo André – SP
CEP 09210-580 · Fone: (11) 4996-0017

FOLHA DE ASSINATURAS

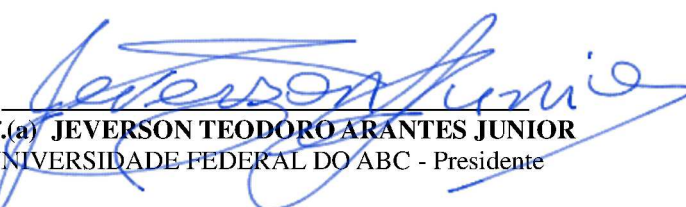
Assinaturas dos membros da Banca Examinadora que avaliou e aprovou a Defesa de Dissertação de Mestrado do candidato, ALEXANDRE OLIVIERI KRAUS realizada em 25 de Junho de 2021:

P/ 
Prof.(a) **CEDRIC ROCHA LEAO**
UNIVERSIDADE FEDERAL DO ABC

P/ 
Prof.(a) **PAULA HOMEM DE MELLO**
UNIVERSIDADE FEDERAL DO ABC

Prof.(a) **MARCIO GUSTAVO DI VERNIERI CUPPARI**
UNIVERSIDADE FEDERAL DO ABC

Prof.(a) **PEDRO ALVES DA SILVA AUTRETO**
UNIVERSIDADE FEDERAL DO ABC


Prof.(a) **JEVERSON TEODORO ARANTES JUNIOR**
UNIVERSIDADE FEDERAL DO ABC - Presidente

* Por ausência do membro titular, foi substituído pelo membro suplente descrito acima: nome completo, instituição e assinatura

This study was financed in part by the Coordenação de Aperfeiçoamento de Pessoal de Nível Superior – Brasil (CAPES) – Finance Code 001

RESUMO

A conversão de energia solar em energia química por meio da fotocatalise da molécula de água oferece uma rota limpa para a produção de gás hidrogênio. Embora o NaNbO_3 seja um fotocatalisador, absorve luz no UV menos abundante, limitando severamente a atividade fotocatalítica. Com simulações de primeiros princípios, investigamos os efeitos da formação de vacâncias e estados de superfície na estrutura cristalina e eletrônica do NaNbO_3 ortorrômbico para aumentar sua atividade fotocatalítica. O controle das condições químicas de síntese permitem privilegiar um tipo de vacância: ambientes ricos em O privilegiam a vacância de Na, enquanto os pobres em O privilegiam a vacância de O. Porém tanto a vacância de Na quanto de O inserem estados profundos dentro da banda proibida, possivelmente agindo como armadilhas de carga. Em outra abordagem, a de filme fino nanométrico orientado em [100] e terminado em NaNbO , formou-se estados de superfície metalizados. Mostramos que a tensão biaxial pode modular o excesso de cargas em camada atômica de superfície, mas não recupera o caráter semicondutor. Esta estrutura eletrônica contrasta com o NaTaO_3 em filme fino equivalente, que permaneceu semicondutor tanto sem, quanto com tensão biaxial. A eletronegatividade do metal de transição desempenhou um papel essencial nisso pois o cátion Ta exigiu significativos rearranjos iônicos para redistribuição de cargas, enquanto que o Nb pôde manter hibridizado com a banda de condução.

Palavras-chave: Perovskitas. Fotocatálise. Primeiros princípios. Vacâncias. Filmes finos.

ABSTRACT

Solar energy conversion into chemical energy through water-splitting photocatalysis offers a clean route for hydrogen gas production. Albeit NaNbO_3 has water-splitting activity, its less abundant UV light absorption severely limits its photocatalytic activity. We investigate, with first-principles simulations, the point defect's and surface states' impact on the orthorhombic NaNbO_3 crystalline and electronic structure for improved photocatalytic activity. Chemical environment control can select which vacancy is favorably formed: on O-rich conditions, Na vacancies are favored, while for O-poor conditions the O vacancies are. However, both vacancy defects insert deep energy levels inside the band gap, likely acting as charge traps. On another approach, the bulk cleavage at $[100]$ direction formed a NaNbO terminated nanometric thin-film with metallic surface states. We have shown that biaxial strain can modulate the surface atomic layer's charge excess but could not recover the bulk's semiconductor character. This electronic structure contrasts with the similar NaTaO_3 , which remained semiconductor at relaxed and strained states on equivalent thin-film orientation. Transition metal electronegativity played an essential role at this, as Ta cation required major atomic rearranges for charge redistribution while on Nb cation charge remained hybridized with conduction bands.

Keywords: Perovskites. Photocatalysis. First-principles. Vacancies. Thin-films.

CONTENTS

1	INTRODUCTION	11
2	METHODS AND METHODOLOGY	17
2.1	Density Functional Theory	17
2.1.1	Atomic Positions Optimization	19
2.1.2	Exchange-correlation Potential Form	20
2.1.3	Projector-augmented Waves and Valence Electrons	21
2.1.4	Charge Counting With The Atoms In Molecules Theory	22
2.2	Crystal Structure's Properties Evaluation	23
2.3	Vacancy Formation Energy Calculation	24
2.3.1	Corrections to Finite-Sized Supercell Artifacts	28
2.4	Thin-film Structure And Properties	30
2.4.1	Biaxial Strain Effects on Thin-film Properties	32
3	RESULTS AND DISCUSSION	33
3.1	The NaNbO₃ Bulk Structure	33
3.2	The Vacancy Formation on Bulk	35
3.2.1	Neutral Defects	35
3.2.2	Charged Defects	37
3.2.3	Vacancy Formation Energies	38
3.3	The [100]-oriented, NaNbO Terminated Thin-film	42
3.3.1	Surface Effects' Sensibility To Slab Width	46
3.3.2	Biaxial Strain Effects	49
3.3.3	Comparison With NaTaO ₃ Thin-film	51
4	CONCLUSIONS	57
	References	59

APPENDIX	73
APPENDIX A – SUPPORTING INFORMATION	75
APPENDIX B – NUMERICAL CONVERGENCES	85

1 INTRODUCTION

The increase in energy demand and the need to substitute traditional energy sources for environmentally sustainable ones drive the search for new materials and processing techniques. The generation of $\text{H}_2(\text{g})$ through the water-splitting reaction can be the ideal source as it generates a high-density fuel from abundant water without toxic side-products. However, the reaction's activation energy is high, requiring catalyst use to scale up gas production in industrial quantities. For this purpose, certain semiconductors can catalyze the water-splitting reaction when exposed to sunlight, producing $\text{O}_2(\text{g})$ at the anode and $\text{H}_2(\text{g})$ at the cathode [1, 2] for storage on other materials. For this role, the semiconductor's band structure must have compatible electronic properties and optical responses to photocatalyze the water-splitting reactions. The material absorbs light, generating an electron-hole pair that is conducted to the semiconductor's surface.

Water-splitting catalysis requires that the conduction band minimum (CBM) be more energetic than the H^+ / H_2 potential, while the valence band maximum (VBM) to be less energetic than the $\text{O}_2 / \text{H}_2\text{O}$ (Fig. 1). As a consequence, electrons have a driving force to interact with reactants at the semiconductor's surface. The photocatalytic activity also depends on other factors, e.g. electron-hole recombination rate, charge mobility, and the active sites' presence at surface [3]. Semiconductors catalyze the water-splitting reactions in three steps:

1. An electron-hole pair is generated through light absorption;
2. The pair is split apart and transported to the surface;
3. The photogenerated charges interact with adsorbed reactants through the active site.

At the cathode, the semiconductor's excited electrons reduce H^+ to H_2 , promoting the hydrogen evolution reaction (HER):

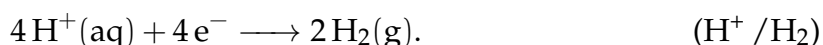
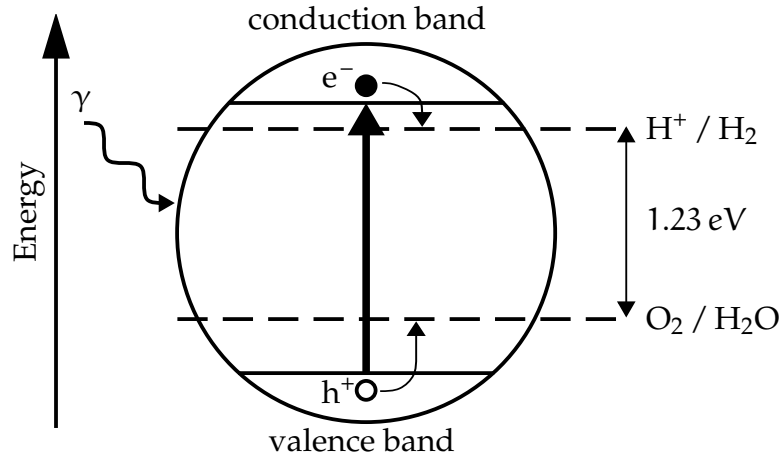
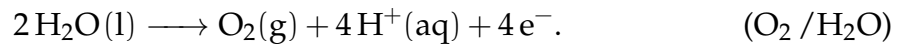


Figure 1 – A semiconductor absorbing light, generating an electron-hole pair. Mobile electrons can catalyze the HER if its energy is higher than the H^+ / H_2 reaction's potential, while holes catalyze the OER when its energy is lower than the O_2 / H_2O potential. Chemical potentials from reference [4].



On the other hand, holes capture electrons released by the oxygen evolution reaction (OER) at the anode:



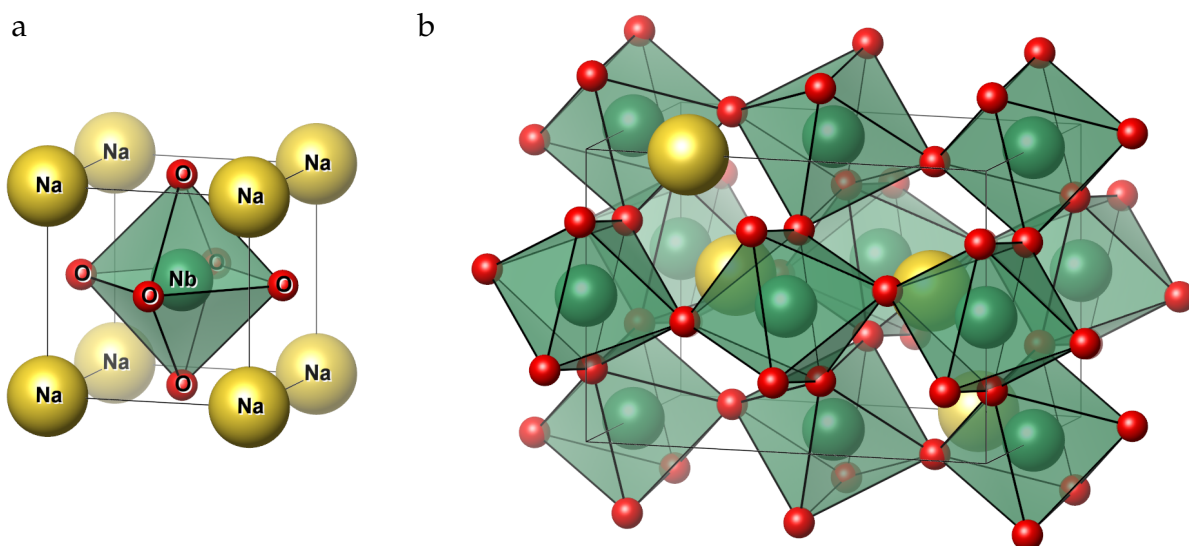
The commonly researched titanium dioxide (TiO_2) and strontium titanate ($SrTiO_3$) require platinum electrodes to generate $H_2(g)$ [5]. Both have good catalytic activity and underwater durability, but their band gap — 3.0 [1] and 3.6 eV [6] respectively — restricts optical transitions to the UV spectrum. The absorption spectrum inside the UV region is undesirable as most light on Earth's surface is on the visible spectrum, requiring association with adequate visible-spectrum absorbing semiconductors or materials' properties manipulation through processing methods. Candidates fit for one or two steps associated with complementary materials to overcome individual limitations, giving photocatalytic tandem cells. Association with more materials generally increases the manufacture's complexity and cost [7], while material processing can overcome the band gap's problem with more straightforward, cheaper approaches.

Promising single-material candidates that excel on all three steps must have an adequate electronic structure for optical transitions, good charge separation and transport properties, and plenty of active sites at their surface. Processing techniques have been shown to activate the photocatalytic activity on TiO_2 [8], $SrTiO_3$ [9] and other semiconductors, but pristine sodium tantalate ($NaTaO_3$) [10, 11] and sodium niobate ($NaNbO_3$) [12–14] have demonstrated native photocatalytic activity under UV light,

attracting the community's efforts. Currently, their absorption spectrum on UV limits the niobates/tantalates application on water-splitting. However, crystal structure modifications promise improvements in photocatalytic activity through enhanced charge carrier concentrations.

SrTiO_3 , NaTaO_3 , and NaNbO_3 compounds belong to the perovskite family of crystal structures. These double metal oxides' crystal structure arranges two distinctly sized cation metals with oxygen, or other anions, in likewise manner to the calcium titanate (CaTiO_3) structure — the perovskite mineral. The ideal, highly symmetric cubic perovskite structure (Fig. 2a) has the first metal on the cell's corners. Typically it is the largest of three species, being an alkaline or rare-earth metal. The second metal occupies the cell's geometric center. It is smaller than the first metal, being a transition metal on most perovskites. Finally, the anion is found on the cubic faces' center, bonding with both cations. Twelve anions bond with the first cation on the cubic structure, while six of them bond with the second cation, forming a dodecahedron and octahedron, respectively. However, most metal combinations are not stable on cubic structure, but as orthorhombic (Fig. 2b) or tetragonal phases due to geometrical restrictions and the chemical environment around the cations [15]. Actual cation saturation becomes smaller with reducing crystal symmetry. A significant number of metals can be accommodated as a perovskite, giving many different materials and properties, including

Figure 2 – Perovskites can have a cubic ($\text{Pm}\bar{3}\text{m}$) (a) or less symmetric structures such as the orthorhombic one (Pmna) (b), depending on environmental conditions and the species' atomic radius ratio.



many photocatalytic semiconductors [16, 17].

From these, both tantalate and niobate perovskites stand out due to their photocatalytic activity, even with 4.0 [11] and 3.4 eV [18] band gaps, respectively. Literature is rich with strategies to change NaTaO_3 properties with impurity insertion, nanometric material processing, and control of surface orientation. Great reviews on most relevant works are on [15, 19], but description on induced changes over crystalline and electronic structures is still growing [20–23]. The intimate description between crystal, electronic structures and photocatalysis for NaNbO_3 is rather smaller than NaTaO_3 , as it produces less $\text{H}_2(\text{g})$ than NaTaO_3 [24]. However, vacancy control has been shown to increase NaNbO_3 water-splitting activity on visible spectrum [25], justifying this point defect's microscopic description.

Vacancy formation is an integral part of a crystal's thermodynamical equilibrium. Thermal energy breaks bonds, freeing atoms/ions and creating vacancies, interstices, and antisites that introduce local deformations on the crystal lattice. The removed species' chemical potential significantly impacts defect concentration on vacancy formation as it determines the thermodynamical driving force for mass exchange between the defect hosting's lattice and external reservoir. Controlling vacancy formation depends on the material's precursors concentration, being central on photocatalyst semiconductor synthesis as it can either poison catalyst activity through charge trapping or enhance it with an improved concentration of free charge carriers.

Defect states are classified according to their associated wavefunction [26]. Shallow defect states come from sites that weakly bind electrons, giving an associated delocalized wavefunction and transition energy levels accessible from thermal energy alone. Consequently, shallow defect states contribute to material's conductivity by increasing the number of available charges without strong mobile charge scattering, boosting photocatalytic activity under adequate conditions. On the other hand, substantial lattice distortions form electronic states highly localized at the defect center with energy levels closer to the band gap's middle point. These, named deep defects, also permit sub-gap excitations but require energies beyond the thermal domain, "trapping" charge carriers at the defect center. As a result, deep defects reduce the material's conductivity and charge available for photocatalysis.

Chemical interactions between the material and its surroundings occur through the surface, offering an alternative approach to semiconductor's properties modification. The selection of the surface's orientation, termination, and defects' concentration changes the oxide semiconductor's electronic properties and photocatalytic activity [27]. The oxide bulk's cleavage on selected orientations leaves a charge excess or deficiency. Consequently, its free energy raises, driving either an atomic rearrangement — a surface reconstruction — or an electronic band's change — an electronic reconstruction [28]. There is no clear distinction between both categories, as surface reconstruction changes electronic band structure and electronic reconstruction alter bond lengths [29]. The first places defect states inside the band gap by altering bonding-antibonding states' separation in a similarly to point defects. The second minimizes free energy by altering electron counting on surface species, inserting holes at the valence band's top or electrons at the bottom of the conduction band. Nevertheless, surface or band structure reconstructions could benefit photocatalytic activity depending on the ground state band structure.

We simulated Na and O vacancy formation on varying supercell sizes and chemical environments, allowing for the formation energies extrapolation to dilute vacancy concentrations, minimizing errors introduced by the supercell approach. We also described the insertion of surface states inside the band gap by nanometric thin-film formation. To modify the thin-film's electronic structure, we investigated the biaxial strain influence on surface states. Finally, we compared NaNbO_3 and NaTaO_3 thin-films on equivalent terminations, demonstrating the transition metal's electronegativity influence on thin-film's electronic structure.

2 METHODS AND METHODOLOGY

The NaNbO_3 pristine and point-defect properties were modeled with the quantum mechanical framework from DFT. DFT gives tools to approximate solutions for the many-body Schrödinger equation at given atomic species and positions inside a simulation cell (supercell), allowing the interpretation of NaNbO_3 response to defects and surface formations. Eigenfunctions and eigenvalues obtained at the iterative evaluation end are interpreted as electron density distribution and energy, respectively. The chosen DFT implementation in the *Vienna Ab initio Simulation Package* (VASP) [30, 31] software also optimizes atomic positions and supercell's parameters to minimize the system's total energy, giving its ground state configuration at given simulation conditions and accuracy. Correlation between crystal structure and electronic properties supports interpreting the projected density of states (pDOS), band structure, and charge distribution in terms of bonding distances, angles, and geometric descriptors. Next, DFT fundamental aspects are introduced, followed by the methodologies employed to evaluate vacancy's impact on bulk properties and biaxial strain's impact on the thin-film electronic properties. Post-processing of simulation data, and also most plot generation on figures through the text, were done with python scripts. Their source code is available at the author's public repository hosted on GITHUB® with URL on footnote¹.

2.1 Density Functional Theory

The DFT overcomes the many-body modeling difficulties by solving an equivalent problem of a single electron inside a potential that approximates both many-body and Pauli exclusion effects. This framework is richly described elsewhere [32, 33]; here, this theory is briefly introduced. Describing the electronic behavior with the Schrödinger equation depends on the system's Hamiltonian. In condensed matter

¹ <https://github.com/o-aleoli>

context, this Hamiltonian has the form:

$$\hat{H} = \underbrace{-\frac{\hbar^2}{2m_e} \sum_i^N \nabla_i^2}_{\text{kinetic energy } \hat{T}} + \underbrace{\frac{1}{2} \frac{1}{4\pi\epsilon_0} \sum_{i \neq j}^N \frac{q_e^2}{\|\mathbf{r}_i - \mathbf{r}_j\|}}_{\text{electron-electron interactions } \hat{U}} + \underbrace{\sum_{i,I}^{N,M} \frac{Z_I q_e^2}{\|\mathbf{r}_i - \mathbf{R}_I\|}}_{\text{nucleus-electron } \hat{V}_N} - \underbrace{\sum_I^M \frac{\hbar^2}{2M_I} \nabla_I^2 + \frac{1}{2} \frac{1}{4\pi\epsilon_0} \sum_{I \neq J}^M \frac{Z_I Z_J q_e^2}{\|\mathbf{R}_I - \mathbf{R}_J\|}}_{\text{ion-ion interactions}}. \quad (2.1)$$

Where m_e is the electron mass, q_e the elementary charge, and $\mathbf{r}_i, \mathbf{r}_j$ the i -th and j -th electrons position-spin coordinates ($\mathbf{r} + \sigma$), respectively. M_I, Z_I , and \mathbf{R} are parameters for each one of M atomic nuclei.

As-is, inserting this \hat{H} on time-independent Schrödinger equation deter its solution due to electron-electron (\hat{U}) and nucleus-electron interactions. The electronic response to the atomic rearrange is considered instantaneous (Born–Oppenheimer approximation) to separate the nucleus-electron interactions. This allows the nuclei degrees of freedom treatment as parameters in total energy calculation, making $\frac{1}{2} \frac{1}{4\pi\epsilon_0} \sum_{I \neq J}^M \frac{Z_I Z_J q_e^2}{\|\mathbf{R}_I - \mathbf{R}_J\|} = E_{II}$ constant and \hat{V}_N an fixed potential. The Born–Oppenheimer approximation comes from the fact that atomic nuclei inertia is much greater than electrons' one: electrons' response is much more intense than nuclei's for equivalent electrostatic potential change. However, electron-electron interactions can not be separated on this formulation, requiring an approximation for many-body interactions and the Pauli exclusion's effects.

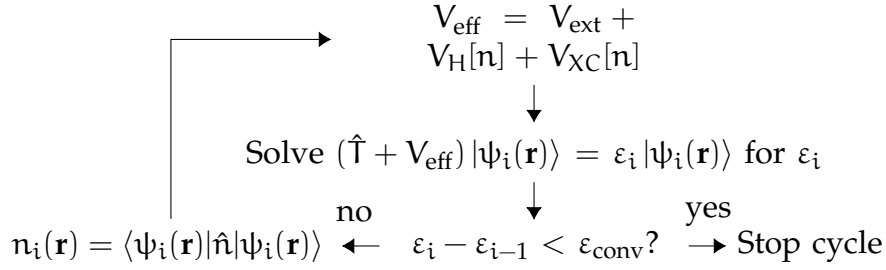
The Kohn–Sham many-body problem approach [34] first solves an auxiliary problem build from each one of the system's single-electron in an effective local potential. Then, from the system's wavefunction, it is generated a many-body problem's electron density function. A new effective local potential then comes from the generated electron density, requiring the Kohn–Sham equation's solution in a self-consistent scheme (Fig. 3) with a stop criterion. The effective local potential $V_{\text{eff}}(\mathbf{r}; n(\mathbf{r}))$ have form:

$$V_{\text{eff}}(\mathbf{r}; n(\mathbf{r})) = V_N(\mathbf{r}) + V_H(\mathbf{r}; n(\mathbf{r})) + V_{XC}(\mathbf{r}; n(\mathbf{r})), \quad (2.2)$$

where both the Hartree potential² $V_H(\mathbf{r}; n(\mathbf{r})) \equiv \frac{\delta E_H[n(\mathbf{r})]}{\delta n(\mathbf{r})}$ and the exchange and cor-

² The Hartree energy comes from the electrostatic interaction between the electron density with itself:
 $E_H[n(\mathbf{r})] = \frac{1}{2} \frac{1}{4\pi\epsilon_0} \int \int d^3r d^3r' \frac{n(\mathbf{r})n(\mathbf{r}')}{\|\mathbf{r} - \mathbf{r}'\|}.$

Figure 3 – The self-consistent cycle is used to calculate energetic eigenvalues and KS orbital wavefunctions.



relation potential³ $V_{\text{XC}}(\mathbf{r}; n(\mathbf{r})) \equiv \frac{\delta E_{\text{XC}}[n(\mathbf{r})]}{\delta n(\mathbf{r})}$ are electron density $n(\mathbf{r})$ functionals. The non-interacting electron' wavefunction $\psi_i(\mathbf{r})$ solve the Kohn–Sham equation (KS), giving the non-interacting spin-dependent energy ϵ_i^σ :

$$[\hat{T} + V_{\text{eff}}(\mathbf{r}; n(\mathbf{r}))] \psi_i(\mathbf{r}) = \epsilon_i^\sigma \psi_i(\mathbf{r}). \quad (2.3)$$

From $\psi_i(\mathbf{r})$ for each one of the system's electrons comes the electron density $n(\mathbf{r})$:

$$n(\mathbf{r}) = \sum_{i=1}^N \|\psi_i(\mathbf{r})\|^2, \text{ requiring } \langle \psi_i(\mathbf{r}, \sigma) | \psi_j(\mathbf{r}, \sigma') \rangle = \delta_{ij} \delta_{\sigma\sigma'}, \quad (2.4)$$

where δ_{ij} are the delta functions. The Kohn–Sham approach is successful in solving the many-body problem thanks to the equivalence between the system's wavefunction and electron density given in the Hohenberg–Kohn theorems [35] and to the \hat{U} substitution for $V_{\text{XC}}(\mathbf{r}; n(\mathbf{r}))$ and $V_{\text{H}}(\mathbf{r}; n(\mathbf{r}))$ in their analytical form. All simulations on this work stopped the self-consistent scheme at differences smaller than 1×10^{-7} eV.

2.1.1 Atomic Positions Optimization

Translating the many-body problem into many independent-electron problems is valid only on ground state conditions, requiring energy minimization. As V_{ext} uniquely defines the system, then the total energy's minimization comes from the nuclei rearrangement (relaxation) inside the supercell until a numeric criterion is achieved. This minimization comes from the force (Hellmann–Feynman) theorem [36]:

$$\mathbf{F}_I = -\frac{\partial E_T}{\partial \mathbf{R}_I}, \text{ where } E_T = T[n(\mathbf{r})] + \int d^3r V_{\text{ext}}(\mathbf{r})n(\mathbf{r}) + E_{\text{H}}[n(\mathbf{r})] + E_{\text{II}} + E_{\text{XC}}^\sigma[n^\sigma(\mathbf{r})]. \quad (2.5)$$

The NaNbO_3 supercell with 20 atoms was build from the conventional orthorhombic cell classified in the Pmna space group and fully relaxed until forces

³ Until this dissertation's defense, no analytical form for the exchange and interaction energy E_{XC} is known. Approximations are discussed in Section 2.1.2.

were smaller than $5 \text{ meV } \text{\AA}^{-1}$. After full relaxation, its lattice parameters became $a = 5.62$, $b = 7.90$ and $c = 5.55 \text{ \AA}$. Comparison with experimental measurements [37] gave divergences of $+1.1\%$, $+0.9\%$ and $+1.4\%$ for a , b and c lattice parameters, respectively. Evaluation of total energy in respect to the supercell's volume assured the conventional cell's relaxed geometry (Fig. 36 in Appendix B). Vacancy formation simulations were done on supercells made from $1 \times 1 \times 1$ (19 atoms), $2 \times 2 \times 2$ (159 atoms), and $3 \times 3 \times 3$ (539 atoms) repetitions of NaNbO_3 conventional cell. Atomic positions were allowed to relax on fixed supercell geometry until forces were smaller than $5 \text{ meV } \text{\AA}^{-1}$. Finally, slab supercells with 86 atoms, modeling the thin-film configuration, also were relaxed with fixed supercell geometry and force criteria of $5 \text{ meV } \text{\AA}^{-1}$. Total energy variation with surface-perpendicular lattice parameters assured the thin-film's strain-free configuration (Fig. 40 in Appendix B).

2.1.2 Exchange-correlation Potential Form

Although the KS equation exactly describes the electronic behavior, this depends on the $V_{\text{XC}}^\sigma(\mathbf{r})$ exact form, which is unknown. Tentative formulations for $V_{\text{XC}}^\sigma(\mathbf{r})$ assumes a sufficiently-smooth $n^\sigma(\mathbf{r})$ to equate the exchange-correlation potential to a exactly-defined one from an one-electron homogeneous free electron gas: the local spin density approximation (LSDA). Slowly-changing density description can be done with density gradients on $V_{\text{XC}}^\sigma(\mathbf{r})$, giving the generalized-gradient approximations (GGA). One of these approximations, the Perdew–Burke–Erzerhof GGA (PBE-GGA) [38], describes $E_{\text{XC}}^\sigma[n^\sigma(\mathbf{r})]$ functional from interpolated homogeneous electron gas Monte Carlo simulations, expressing condensed matter properties with great agreement to experimental values. An exception is made for the band gap value, which frequently is 50% smaller than experimental evaluations [39]. As $E_{\text{XC}}^\sigma[n^\sigma(\mathbf{r})]$ is obtained from the N -electron $n^\sigma(\mathbf{r})$, it includes a self-interaction factor which can not be completely corrected, giving excessive wavefunction delocalization, and no way to corretely obtain the derivative discontinuities of electron bands in respect to their filling.

Both quantitative band gap description and conduction band energy level estimation with PBE-GGA were not expected to be close to experimental values. Also, point defect and surface formations require bond cleavage, giving fractional band occupation, which would also be affected by self-interaction error. Then, electronic

properties interpretation was made in the light of Ligand Field Theory, ionic bonding, and literature description of transition metal oxide surface formation. Closer correlation to experiments can be obtained from beyond-DFT approaches. However, many of them are computationally prohibitive for large supercells [39], and the approaches comparable to DFT computational cost require either tuning parameters for convergence with experimental measurements or also computationally intensive parameter convergence [40].

2.1.3 Projector-augmented Waves and Valence Electrons

KS wavefunctions encode the information for all system's electrons. However, the contribution from electrons below the valence layer to chemical interactions is negligible. Their substitution for adequate wavefunctions can reproduce the core-screening effect on valence electrons with reduced computational cost. *VASP* software implements projector-augmented waves (PAW) [31, 41] to describe the valence electrons' states $|\psi_i\rangle$ from pseudo-wavefunctions' states $|\tilde{\psi}_i\rangle$ combined with their spheric projections $\langle p_{\mathbf{R}_m} | \tilde{\psi}_{i\mathbf{R}_m} \rangle$ into nuclei positions \mathbf{R}_I :

$$|\psi_i\rangle = |\tilde{\psi}_i\rangle + \sum_m \sum_I \langle p_{I\mathbf{m}} | \tilde{\psi}_{iI\mathbf{m}} \rangle (|\psi_{iI\mathbf{m}}\rangle - |\tilde{\psi}_{iI\mathbf{m}}\rangle). \quad (2.6)$$

m summation is done over all core states. PAW builds $|\psi_i\rangle$ on real space from plane waves in the reciprocal space (\mathbf{k}), with Wigner-Seitz cell volume Ω , and reciprocal lattice vectors \mathbf{G} :

$$\langle \mathbf{r} | \psi_i \rangle = \frac{1}{\Omega^{1/2}} \sum_{\mathbf{G}}^{G_{\text{MAX}}} C_{i\mathbf{k}\mathbf{G}} \exp [i (\mathbf{k} + \mathbf{G}) \cdot \mathbf{r}]. \quad (2.7)$$

The cutoff energy parameter limits the plane-wave expansion:

$$E_{\text{cut}} = \frac{\hbar^2}{2m_e} |\mathbf{G}_{\text{MAX}}|^2 \implies |\mathbf{G}_{\text{MAX}}| = \sqrt{\frac{2m_e}{\hbar^2} E_{\text{cut}}}. \quad (2.8)$$

The general self-consistent routine (Fig. 3) implemented in *VASP* begins with PAW generated from isolated atoms all-electron calculations, being updated to optimize total energy under the system's conditions. Here, all NaNbO_3 simulations were done with a cutoff of 520 eV, adequate to describe Na, Nb and O core regions within 10 meV accuracy.

PAW construction and electronic properties' evaluation are done on crystal lattice's reciprocal space. Consequently, a \mathbf{k} -points lattice suit for calculations must

be dense enough to converge total energy without bias — well-representing features from crystal symmetries. Reciprocal lattices used were built with Monkhorst–Pack method [42], embedding crystal’s symmetry points. NaNbO₃ pristine conventional cell was evaluated with a $7 \times 5 \times 7$ mesh (48 points), converging the total energy within 10 meV (Fig. 37 on Appendix B). As defect formation was simulated on supercells with increasing volume, k-point density obtained from pristine bulk was preserved. Vacancy formation on $2 \times 2 \times 2$ supercells used a $3 \times 3 \times 3$ k-point mesh (14 points). Vacancy formation on $3 \times 3 \times 3$ supercells were modeled with a single \mathbf{k} -point at $(\frac{1}{7} \frac{1}{5} \frac{1}{7})$. The Γ point was avoided as other studies found that error from shallow defect levels’ electronic repulsions were larger at Γ [43–45]. Slab models for thin-film and surface simulations used a $1 \times 5 \times 5$ \mathbf{k} -points mesh due to supercell’s small reciprocal length on X direction to mitigate spurious surface interactions.

2.1.4 Charge Counting With The Atoms In Molecules Theory

The system’s ground state wavefunction gives all information about it at defined conditions. However, it gives no framework to evaluate atom-centered observables, such as valence charges. The Atoms in Molecules theory developed by Richard F. W. Bader [46] evaluate the topological features of charge density, giving a first-principles method to extract atom-averaged observables from the system’s wavefunction.

As the electron-nucleus electrostatic interactions dominate condensed matter at laboratory conditions, $n(\mathbf{r})$ topology encodes the nuclei charges and positions. The critical points of $n(\mathbf{r})$ scalar field can help recover information about individual atoms. V_{ext} induces discontinuities at $n(\mathbf{r})$ similarly to a local maximum — but discontinuous —, while the path that connects two local maxima contains a saddle point. As these saddle points mark negative curvatures in two directions, they limit a basin region around local maxima, allowing the definition of a bonding atom without *ad hoc* postulations. Furthermore, saddle points define zero-flux surfaces, satisfying variational principle requirements that describe observables inside the constrained regions’ volume. Nonetheless, we refrain from additional development of Bader’s theory, as it will be used only to evaluate the charge inside Bader’s volume by integrating $n(\mathbf{r})$. We use the Henkelman Group’s code [47–50] to evaluate the Bader’s charge from converged charge density file generated with *VASP* routines.

2.2 Crystal Structure's Properties Evaluation

Most perovskites' valence and covalent bands are sensible to the octahedron's geometry formed by six vertex oxygens and a central transition metal [51, 52]. Herein, both NbO_6 internal and neighboring-octahedra arranges were evaluated for each system. Octahedral geometry was described with Baur's distortion index [53], measuring how much each individual Nb–O bond length $d_{\text{Nb-O}i}$ deviates from the average $\overline{d_{\text{Nb-O}}}$:

$$\Delta_d = \frac{1}{6} \sum_{i=1}^6 \frac{|d_{\text{Nb-O}i} - \overline{d_{\text{Nb-O}}}|}{\overline{d_{\text{Nb-O}}}}. \quad (2.9)$$

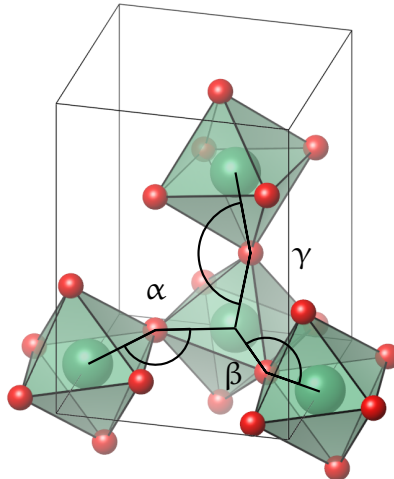
Ideal octahedra have $\Delta_d \rightarrow 0\%$, as all Nb–O bonds are equivalent, while distorted octahedra have significant Δ_d , indicating a prejudice on p – d orbitals overlap and a raise on bonding-antibonding energy difference.

Selected thin-film [100]-orientation formed NbO_4 tetrahedra, their geometric changes were evaluated with a planarity index P_L :

$$P_L = \frac{\langle \theta \rangle}{180^\circ}. \quad (2.10)$$

Octahedral rotations also were evaluated, as their relative spatial configuration affects band dispersions [51]. Average O–Nb–O angles $\langle \theta \rangle$ were compared with ideal 180° , configuration for optimal p – d orbital overlap. Nb–O–Nb angles were measured following the conventional cell's crystallographic directions $[\bar{1}01]$, $[101]$ and $[010]$; then averaged in α , β and γ respectively (Fig. 4).

Figure 4 – The angles γ defined for $[010]$ direction, β for $[10\bar{1}]$ and α for $[101]$. The same directions are taken in slab bond's evaluation.



2.3 Vacancy Formation Energy Calculation

A *vacancy* is defined as an unoccupied atomic site at the crystal lattice. We adopted the Kröger–Vink notation [54] with a slight change: an X specie vacancy with charge q was shortly noted as v_X^q for improved readability. Herein, sodium ($v_{\text{Na}}^0, v_{\text{Na}}^{1-}$) and oxygen ($v_{\text{O}}^0, v_{\text{O}}^{2+}$) vacancies were simulated and compared. The Nb vacancy was beyond our scope due to its high formation energy [55], making it less useful for NaNbO₃ properties change.

Vacancy formation energy ΔE_f was obtained by comparing the single point defect supercell's total energy $E_T(v_X^q; L)$ with the pristine bulk's total energy $E_T(\text{bulk}; L)$. Additionally, the vacancy formation process transferred ($n_X < 0$) an X specie to a mass reservoir with chemical potential μ_X [56–59]:

$$\Delta E_f(v_X^q; L) = E_T(v_X^q; L) - E_T(\text{bulk}; L) - n_X \mu_X + q \varepsilon_F + E_c. \quad (2.11)$$

Correction term E_c fixed excessive wavefunction delocalization effect on total energy evaluation. The later paragraphs will further explain the E_c evaluation. If a point defect were ionized to q state, then q electrons were transferred to (or from) a mass reservoir with a chemical potential $\mu_e = \varepsilon_F$, where ε_F is the Fermi level. However, ε_F obtained from DFT does not carry physical meaning because it is used as a numeric tool for correct energy band filling. According to the Fermi-Dirac statistics, the Fermi level pinpoints the energy which a hypothetical band would have, at any temperature, to be half-filled [60]. In a thermodynamical context, this quantity gives the electronic chemical potential. For an electron's canonical ensemble without thermal contributions, the Fermi level approaches the CBM value for both intrinsic and dilute-doped semiconductors [61]. Fermi levels used on all ionized defects were obtained from pristine supercell and reference was taken from its VBM. Fermi levels used on all ionized defects were obtained from pristine supercell with reference taken from its VBM.

Formation energy has been shown to depend on the distance between the vacancy center and its images L , varying with the supercell's volume [45, 62]. As so, ΔE_f was calculated comparing supercells with the same volume. By adding entropic and pressure-volume terms, it becomes possible to express vacancy formation enthalpies and their kinetics. Entropic terms can be evaluated from the harmonic oscillator approach, yet they are commonly disregarded as their contribution does not change qualitative

conclusions at the same time they have high computational cost [63]. The pressure-volume term was also disregarded as it typically has insignificant contributions at room conditions.

It was expected that the removal of the Na atom would leave neighboring O with a charge deficiency, imposing acceptor-like states on the host's electronic structure. While the removal of the O atom partially filled the valence of the neighboring cation, imposing donor-like states. Both defect bands would be partially filled and flat in the dilute limit. Nevertheless, these bands assume the host's dispersion when simulated on supercells due to their hybridization with similar-energy host bands, affecting total energy evaluation and band occupation numbers [63, 64]. Correction term E_c fix the defect band dispersion effect on total energy by comparing n -band energy $\epsilon_n(\mathbf{k})$ with either pristine host's CBM (ϵ_{CBM}) or VBM (ϵ_{VBM}) depending if the defect band is donor-like or acceptor-like in nature, respectively:

$$E_c = \begin{cases} -\sum_{\mathbf{k},n} w_{\mathbf{k}} f_{\mathbf{k},n} (\epsilon_n(\mathbf{k}) - \epsilon_{\text{CBM}}), & \text{if donor-like or} \\ \sum_{\mathbf{k},n} w_{\mathbf{k}} (1 - f_{\mathbf{k},n}) (\epsilon_n(\mathbf{k}) - \epsilon_{\text{VBM}}), & \text{if acceptor-like.} \end{cases} \quad (2.12)$$

Where the sum was taken for all \mathbf{k} -points and partially filled donor (acceptor) defect bands n . $w_{\mathbf{k}}$ is the \mathbf{k} -th point integration weight and $f_{\mathbf{k},n}$ the n -th band filling factor. It was also expected that Na^{1+} (O^{2-}) ion removal would leave filled (empty) defect bands, which could not affect total energy evaluation from the excessive dispersion perspective. Other finite-sized supercell artifacts — quantum mechanical, elastic, and electrostatic defect-image interactions — were treated by fitting a scaling law and extrapolating it to $L \rightarrow \infty$. More details on Section 2.3.1.

Solving KS equations by using a GGA-PBE approximation for the E_{XC} is successful in describing most solid's crystal properties, total-energy-dependent properties, and even some qualitative energy band features. Nevertheless, it also poorly describes excited electronic states which, on point defect formation context, impairs transition levels' description of vacancy ionization. Nevertheless, it also poorly describes excited electronic states, which impairs transition levels' description of vacancy ionization on point defect formation context. Transition levels' evaluation is essential on defect level classification as shallow or deep, and it is also central on defect level study with spectroscopy techniques [65]. A naive approach would infer these transition levels from

KS energy levels, but, for thermodynamical transitions, it is also possible to approach this quantity from the vacancy's $\Delta E_f(v_X^q; L \rightarrow \infty)$ difference when $\varepsilon_F = \varepsilon_{VBM}$ [66]. For the Na transition from v_{Na}^0 to v_{Na}^{1-} :

$$\varepsilon_{Na}(0/1-) = \frac{\Delta E_f(v_{Na}^0; L \rightarrow \infty)_{\varepsilon_F=0} - \Delta E_f(v_{Na}^{1-}; L \rightarrow \infty)_{\varepsilon_F=0}}{(-1) - 0}. \quad (2.13)$$

The transition from v_O^0 to v_O^{2+} :

$$\varepsilon_O(0/2+) = \frac{\Delta E_f(v_O^0; L \rightarrow \infty)_{\varepsilon_F=0} - \Delta E_f(v_O^{2+}; L \rightarrow \infty)_{\varepsilon_F=0}}{2 - 0}. \quad (2.14)$$

Altering the species and electron quantities changes the reference energy level used by DFT routines to calculate bands' energy levels. The average lattice potential far from the defect center, which should describe the pristine bulk's potential, differs from the reference pristine crystal potential by a constant. This difference can be used to align the defective supercell's electronic structure to the pristine one, allowing the correct evaluation of a charge transfer with an electron reservoir. Indeed, the pristine crystal potential behavior was recovered in larger supercells (Fig. 26 and 27 in Appendix A). However, in $1 \times 1 \times 1$ supercells, it was not recovered (Fig. 28 on Appendix A), making the pristine crystal potential comparison inadequate. As so, the potential alignment was not performed for any ΔE_f calculation. Deviations from the pristine crystal potential were approached with the scaling law extrapolation, as the vacancy-images interactions were responsible for this behavior [62].

For NaNbO_3 under stoichiometric conditions, each element's chemical potential equilibrates with the stable perovskite's potential (zero superscripts), leaving two unknown potentials. A first approach is to assume an equilibrium with O_2 molecule and Na, Nb metals in solid bulk structure:

$$\mu_{\text{NaNbO}_3}^0 = \mu_{\text{Na}} + \mu_{\text{Nb}} + 3\mu_{\text{O}} \implies \begin{cases} \mu_{\text{O}} = \frac{1}{3}(\mu_{\text{NaNbO}_3}^0 - \mu_{\text{Na}}^0 + \mu_{\text{Nb}}^0) \\ \mu_{\text{Na}} = \mu_{\text{NaNbO}_3}^0 - \mu_{\text{Nb}}^0 - 3(\frac{1}{2}\mu_{\text{O}_2}^0) \end{cases}. \quad (2.15)$$

As vacancy formation heavily depends on synthesis's chemical conditions, it is essential to model the chemical potential effect on vacancy formation energy. Modeling was done by substituting $\frac{1}{2}(\mu_{\text{O}}^0)$, μ_{Na}^0 and μ_{Nb}^0 for intermediary compounds given by O–Na–Nb ternary diagram (Fig. 5). From the Open Quantum Materials Database (OQMD) [67, 68], we have three stable metal oxides for Na and Nb and no known intermediary

compounds from Na–Nb mixtures. Compounds' chemical potentials were obtained from compounds' total energy converged with respect to the k-points mesh (Fig. 38 on Appendix) and compared to experimental values (Tab. 1). No variation on the crystalline phase was considered to obtain the chemical potentials, as their crystal phase does not change at room conditions. Regions from A to I in Fig. 5 gave the following chemical potentials:

$$\begin{cases} \mu_{\text{NaNbO}_3}^0 = \mu_{\text{Na}} + \mu_{\text{Nb}} + 3\mu_{\text{O}} \\ \mu_{\text{NaO}_2}^0 = \mu_{\text{Na}} + 2\mu_{\text{O}} \\ \mu_{\text{O}} = \frac{1}{2}\mu_{\text{O}_2}^0 \end{cases} \Rightarrow \begin{cases} \mu_{\text{Na}} = \mu_{\text{NaO}_2}^0 - \mu_{\text{O}_2}^0 \\ \mu_{\text{Nb}} = \mu_{\text{NaNbO}_3}^0 - \mu_{\text{NaO}_2}^0 - \frac{1}{2}\mu_{\text{O}_2}^0 \\ \mu_{\text{O}} = \frac{1}{2}\mu_{\text{O}_2}^0 \end{cases} \quad (1.A)$$

$$\begin{cases} \mu_{\text{NaNbO}_3}^0 = \mu_{\text{Na}} + \mu_{\text{Nb}} + 3\mu_{\text{O}} \\ \mu_{\text{NaO}_2}^0 = \mu_{\text{Na}} + 2\mu_{\text{O}} \\ \mu_{\text{Na}_2\text{O}_2}^0 = 2\mu_{\text{Na}} + 2\mu_{\text{O}} \end{cases} \Rightarrow \begin{cases} \mu_{\text{Na}} = \mu_{\text{Na}_2\text{O}_2}^0 - \mu_{\text{NaO}_2}^0 \\ \mu_{\text{Nb}} = \mu_{\text{NaNbO}_3}^0 + \frac{1}{2}\mu_{\text{Na}_2\text{O}_2}^0 - 2\mu_{\text{NaO}_2}^0 \\ \mu_{\text{O}} = \mu_{\text{NaO}_2}^0 - \frac{1}{2}\mu_{\text{Na}_2\text{O}_2}^0 \end{cases} \quad (1.B)$$

$$\begin{cases} \mu_{\text{NaNbO}_3}^0 = \mu_{\text{Na}} + \mu_{\text{Nb}} + 3\mu_{\text{O}} \\ \mu_{\text{Na}_2\text{O}}^0 = 2\mu_{\text{Na}} + \mu_{\text{O}} \\ \mu_{\text{Na}_2\text{O}_2}^0 = 2\mu_{\text{Na}} + 2\mu_{\text{O}} \end{cases} \Rightarrow \begin{cases} \mu_{\text{Na}} = \mu_{\text{Na}_2\text{O}}^0 - \frac{1}{2}\mu_{\text{Na}_2\text{O}_2}^0 \\ \mu_{\text{Nb}} = \mu_{\text{NaNbO}_3}^0 - 2\mu_{\text{Na}_2\text{O}}^0 - \frac{5}{2}\mu_{\text{Na}_2\text{O}_2}^0 \\ \mu_{\text{O}} = \mu_{\text{Na}_2\text{O}}^0 - \frac{1}{2}\mu_{\text{Na}_2\text{O}_2}^0 \end{cases} \quad (1.C)$$

$$\begin{cases} \mu_{\text{NaNbO}_3}^0 = \mu_{\text{Na}} + \mu_{\text{Nb}} + 3\mu_{\text{O}} \\ \mu_{\text{Na}_2\text{O}}^0 = 2\mu_{\text{Na}} + \mu_{\text{O}} \\ \mu_{\text{Na}}^0 = \mu_{\text{Na}} \end{cases} \Rightarrow \begin{cases} \mu_{\text{Na}} = \mu_{\text{Na}}^0 \\ \mu_{\text{Nb}} = \mu_{\text{NaNbO}_3}^0 - 3\mu_{\text{Na}_2\text{O}}^0 + 5\mu_{\text{Na}}^0 \\ \mu_{\text{O}} = \mu_{\text{Na}_2\text{O}}^0 - 2\mu_{\text{Na}}^0 \end{cases} \quad (1.D)$$

$$\begin{cases} \mu_{\text{NaNbO}_3}^0 = \mu_{\text{Na}} + \mu_{\text{Nb}} + 3\mu_{\text{O}} \\ \mu_{\text{Na}}^0 = \mu_{\text{Na}} \\ \mu_{\text{Nb}}^0 = \mu_{\text{Nb}} \end{cases} \Rightarrow \begin{cases} \mu_{\text{Na}} = \mu_{\text{Na}}^0 \\ \mu_{\text{Nb}} = \mu_{\text{Nb}}^0 \\ \mu_{\text{O}} = \frac{1}{3} \left(\mu_{\text{NaNbO}_3}^0 - \mu_{\text{Na}}^0 - \mu_{\text{Nb}}^0 \right) \end{cases} \quad (1.E)$$

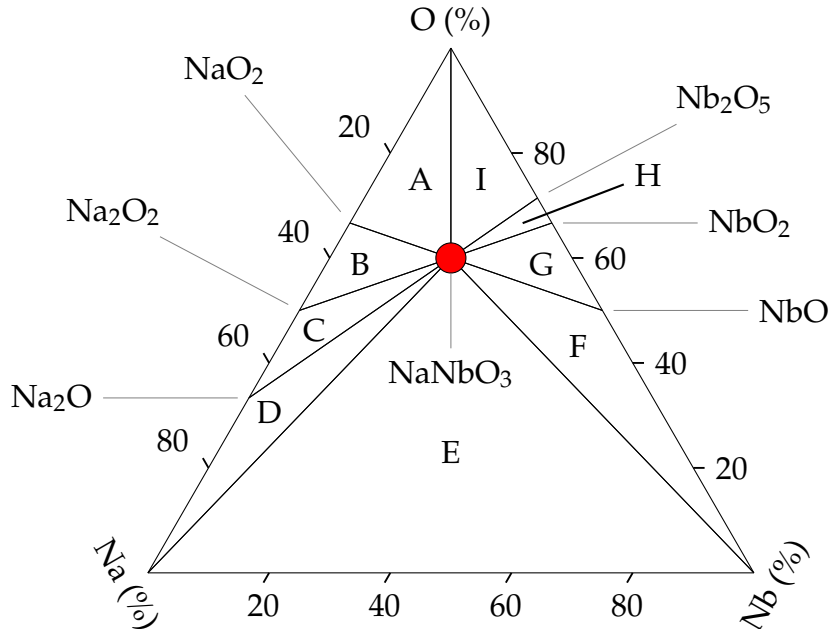
$$\begin{cases} \mu_{\text{NaNbO}_3}^0 = \mu_{\text{Na}} + \mu_{\text{Nb}} + 3\mu_{\text{O}} \\ \mu_{\text{Nb}}^0 = \mu_{\text{Nb}} \\ \mu_{\text{NbO}}^0 = \mu_{\text{Nb}} + \mu_{\text{O}} \end{cases} \Rightarrow \begin{cases} \mu_{\text{Na}} = \mu_{\text{NaNbO}_3}^0 - 3\mu_{\text{NbO}}^0 + 2\mu_{\text{Nb}}^0 \\ \mu_{\text{Nb}} = \mu_{\text{Nb}}^0 \\ \mu_{\text{O}} = \mu_{\text{NbO}}^0 - \mu_{\text{Nb}}^0 \end{cases} \quad (1.F)$$

$$\begin{cases} \mu_{\text{NaNbO}_3}^0 = \mu_{\text{Na}} + \mu_{\text{Nb}} + 3\mu_{\text{O}} \\ \mu_{\text{NbO}}^0 = \mu_{\text{Nb}} + \mu_{\text{O}} \\ \mu_{\text{NbO}_2}^0 = \mu_{\text{Nb}} + 2\mu_{\text{O}} \end{cases} \Rightarrow \begin{cases} \mu_{\text{Na}} = \mu_{\text{NaNbO}_3}^0 + \mu_{\text{NbO}}^0 - 2\mu_{\text{NbO}_2}^0 \\ \mu_{\text{Nb}} = 2\mu_{\text{NbO}}^0 - \mu_{\text{NbO}_2}^0 \\ \mu_{\text{O}} = \mu_{\text{NbO}_2}^0 - \mu_{\text{NbO}}^0 \end{cases} \quad (1.G)$$

$$\begin{cases} \mu_{\text{NaNbO}_3}^0 = \mu_{\text{Na}} + \mu_{\text{Nb}} + 3\mu_{\text{O}} \\ \mu_{\text{NbO}_2}^0 = \mu_{\text{Nb}} + 2\mu_{\text{O}} \\ \mu_{\text{Nb}_2\text{O}_5}^0 = 2\mu_{\text{Nb}} + 5\mu_{\text{O}} \end{cases} \Rightarrow \begin{cases} \mu_{\text{Na}} = \mu_{\text{NaNbO}_3}^0 + \mu_{\text{NbO}_2}^0 - \mu_{\text{Nb}_2\text{O}_5}^0 \\ \mu_{\text{Nb}} = 5\mu_{\text{NbO}_2}^0 - 2\mu_{\text{Nb}_2\text{O}_5}^0 \\ \mu_{\text{O}} = \mu_{\text{Nb}_2\text{O}_5}^0 - 2\mu_{\text{NbO}_2}^0 \end{cases} \quad (1.H)$$

$$\begin{cases} \mu_{\text{NaNbO}_3}^0 = \mu_{\text{Na}} + \mu_{\text{Nb}} + 3\mu_{\text{O}} \\ \mu_{\text{Nb}_2\text{O}_5}^0 = 2\mu_{\text{Nb}} + 5\mu_{\text{O}} \\ \mu_{\text{O}_2}^0 = 2\mu_{\text{O}} \end{cases} \Rightarrow \begin{cases} \mu_{\text{Na}} = \mu_{\text{NaNbO}_3}^0 - \frac{1}{2}\mu_{\text{Nb}_2\text{O}_5}^0 - \frac{1}{4}\mu_{\text{O}_2}^0 \\ \mu_{\text{Nb}} = \frac{1}{2}\mu_{\text{Nb}_2\text{O}_5}^0 - \frac{5}{4}\mu_{\text{O}_2}^0 \\ \mu_{\text{O}} = \frac{1}{2}\mu_{\text{O}_2}^0 \end{cases} \quad (1.I)$$

Figure 5 – The O–Na–Nb ternary diagram showing the stable intermediary compounds and regions used to calculate ΔE_f .



2.3.1 Corrections to Finite-Sized Supercell Artifacts

Vacancy simulation using supercells exploits well-tested and efficient DFT software implementations. However, simulated defects interact with images generated by

Table 1 – The stable crystalline phase of each intermediary compound is used to vary the chemical potential.

Compound	Stable Configuration	
O ₂	gas	
Na	P6 ₃ /mmc	[69]
Na ₂ O	Pm $\bar{3}$ m	[70]
Na ₂ O ₂	P $\bar{6}$ /2m	[71]
NaO ₂	I/41	[72]
Nb	Im $\bar{3}$ m	[73]
NbO	Pm $\bar{3}$ m	[74]
NbO ₂	I4 ₁ /a	[75]
Nb ₂ O ₅	C2/m	[76]

the periodic boundary conditions, significantly affecting the formation energy, electronic energy levels, and wavefunction localization. Spurious interactions can be quantum mechanical, elastic, electrostatic or magnetic in nature [66]. Elastic, electrostatic, and magnetic interactions vanish with volume increase as they become increasingly screened by neighboring species. Defect-images wavefunction overlap vanishes with their distance increase. These finite-sized supercell artifacts' influence on ΔE_f can be corrected by post-processing approaches [66, 77] or modelled to give ΔE_f extrapolated for infinite-sized supercells using a fitted equation [62].

Studies on semiconductors with varying band gap sizes and point defects have shown that finite-sized supercell artifacts on ΔE_f closely resembles a scaling law with $a_1 L^{-1}$ and $a_3 L^{-3}$ terms [62]:

$$\Delta E_f(v_X^q; L) = \Delta E_f(v_X^q; L \rightarrow \infty) + a_1 L^{-1} + a_3 L^{-3}. \quad (2.16)$$

The first term gives the vacancy formation energy extrapolated to an infinite-sized supercell, while a_1 and a_3 are fitting parameters. Here, L represents the supercell's characteristic size, obtained from its volume $\Omega^{1/3} = L$. From the finite-sized supercell artifacts' nature, these fitting parameters can be correlated to a collection of distance-dependent phenomena — such as quantum mechanical — or volume-dependent phenomena — such as electrostatic and elastic artifacts. Still, a_1 and a_3 have no physical interpretation.

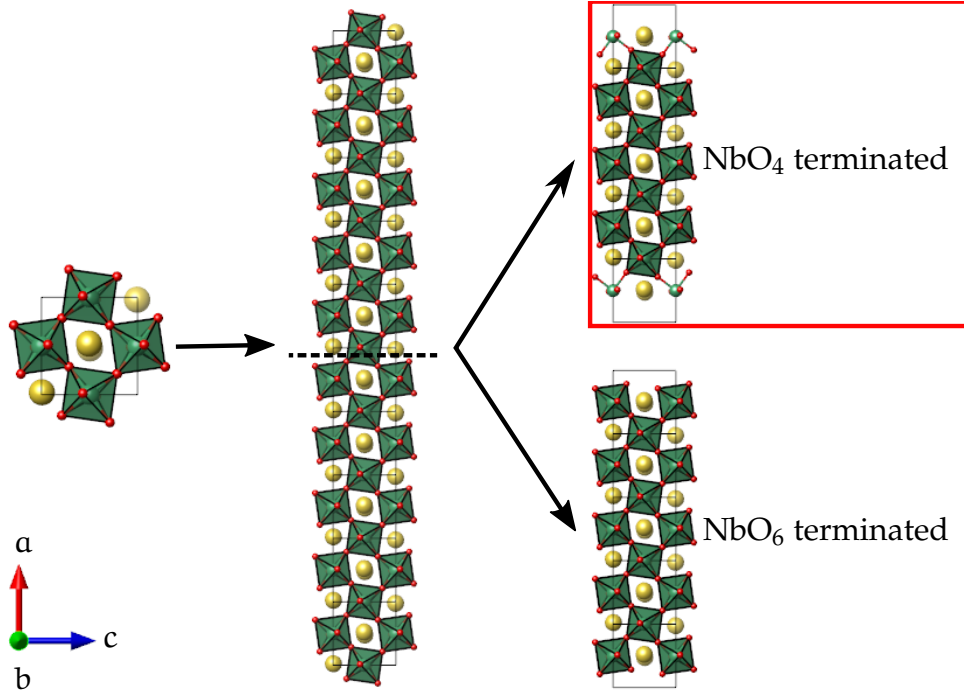
On the other hand, the Freysoldt–Neugebauer–Van de Walle (FNV) [77] scheme deals with the α_3 constant, correcting finite-sized supercell’s electrostatic artifacts. For this, finite-sized supercell’s electrostatic interactions can be modeled as a point charge at the defect center with a gaussian electrostatic potential screened by the host’s dielectric constant.

Herein, finite-sized supercell artifacts were corrected by fitting Eq. 2.16 to a $(\Delta E_f(v_X^q; L), L^{-1})$ dataset for each v_X^q . Chosen supercell sizes were $1 \times 1 \times 1$, $2 \times 2 \times 2$, and $3 \times 3 \times 3$ with 19, 159, and 539 atoms and $L^{-1} = 0.16, 0.08$ and 0.05 \AA^{-1} , respectively. We also employed the FNV scheme for the v_O^{2+} defect on $3 \times 3 \times 3$ supercell, obtaining a corrected ΔE_f . For this, we calculated the pristine NaNbO_3 static ion-clamped dielectric matrix using the density functional perturbation theory [78, 79] with the same previously used simulation parameters. In addition, ΔE_f extrapolation requires equivalence between defects, as so, vacancy sites with the exact point symmetry were chosen. For the orthorhombic (Pmna) NaNbO_3 conventional cell, its 20 lattice positions belong to the mmm point group. All Na atoms are at 4c Wyckoff positions, requiring no special attention for symmetry equivalence. However, O can be at 8d (in-plane) or 4c (out of plane) positions, which have different ΔE_f values on other perovskites [80]. In this study, one O at 4c is removed from each supercell.

2.4 Thin-film Structure And Properties

As seen on vacancy simulation, attention to finite-sized supercell artifacts also must be taken to thin-film simulations. Surface effects are evaluated with slabs built to reproduce surface orientation and termination by manipulating the conventional cell’s structure into a supercell symmetric over the surface plane [81]. Isolated surface effects’ studies seek to overcome finite-sized supercell artifacts by using adequate vacuum sizes for wavefunction decay across it and enough atomic layers for bulk wavefunction recovery at the slab’s middle plane. This recovery is enforced by fixing atomic positions inside a region with the same size and composition as the bulk conventional cell. Nanometric thin-film’s simulation differs from the surface’s approach as an interaction between the two slab surfaces is imposed by design to change bulk’s properties, allowing all atomic positions to relax.

Figure 6 – The slab building process from the conventional cell (thin black boxes) to non-stoichiometric NbO_4 and NbO_6 terminated slabs by cleaving on (100) plane (thick dashed black line). Herein, NbO_4 terminated slab (red square) was analyzed.



Herein, slabs were oriented on $[100]$ direction, commonly obtained on orthorhombic crystal epitaxial growth [82] and on suspended particles [83]. Growth conditions' control can form non-stoichiometric terminations. The NaNbO_3 terminations on (100) planes can have O-rich ($\text{NaNbO}_{3+2/9}$) or O-poor ($\text{NaNbO}_{3-2/9}$) compositions, resulting in NbO_6 terminated and NbO_4 terminated surfaces respectively (Fig. 6). Composition changes also induce formal charges on the surface. NbO_6 terminated surfaces have $4-$ formal charge, while NbO_4 terminated have $4+$, both prompting charge-compensating phenomena. NbO_4 terminated thin-films were simulated on slabs with one (22 atoms), three (86 atoms), and five (146 atoms) conventional cell's repetitions on $[100]$ direction with 15 \AA vacuum width. Termination's choice was based on cation exposure, which could offer active sites for photocatalysis. Strain-free lattice parameters perpendicular to $[100]$ were determined under total energy minimization for three-cells slab (Fig. 40 in Appendix B), giving $b = 7.98$ and $c = 5.06 \text{ \AA}$, both 1% greater than bulk's. After total structural relaxation, the thin-film's structural parameters, pDOS, band structure, and charge counting with the AIM approach were evaluated.

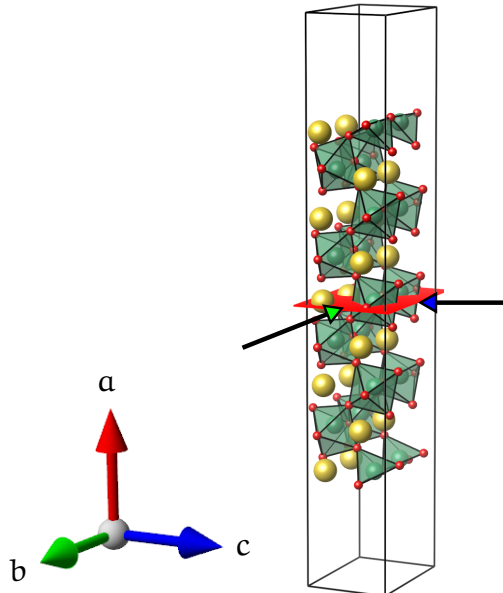
2.4.1 Biaxial Strain Effects on Thin-film Properties

A thin-film deposition process allows for biaxial strain states modulation, which can change how the system responds to formal charge compensation [84, 85]. Nanometric thin-film deposition over adequate substrates has been shown to achieve tractions over 4% [86]. However, extreme tension states often introduce unwanted strain-relieving defects on thin-film lattice and could trigger phase transformations. Herein, biaxial strain states were modeled on $[-5\%, 5\%]$ interval in 1% steps, probing both small strain states and film's properties trend with high strains, probing the crystal structure's limits before phase transformation. Real biaxial strain states varies on film's orientation, but a simplifying $\epsilon_b = \epsilon_c = \epsilon$ assumption were made without prejudice to results:

$$\epsilon = \frac{b - b_0}{b_0} = \frac{c - c_0}{c_0}. \quad (2.17)$$

Where b_0 and c_0 are the bulk lattice parameters perpendicular to $[100]$, while b and c to achieve strain state ϵ (Fig. 7). Comparisons were made to the ground state thin-film by evaluating geometric and electronic properties.

Figure 7 – The biaxial strain plane (red) defined with b (green) and c (blue) lattice parameters.



3 RESULTS AND DISCUSSION

3.1 The NaNbO_3 Bulk Structure

After total relaxation of atomic positions and lattice parameters, we plotted both NaNbO_3 orthorhombic phase's band structure and projected density of states (pDOS) (Fig. 8) for comparison with vacancy-containing and thin-film systems. DFT level of theory described an indirect band gap of 1.91 eV, which is smaller than experimental 3.42 eV [87] due to its well known limitations underestimation [88]. On light absorption, excited electrons would be promoted from the valence band maximum (VBM) on the $\Gamma - Z$ line to the conduction band minimum (CBM) at Γ . The perovskite's electronic structure can be divided into three segments with distinct orbital composition: the uppermost valence band segment with an O 2p character, the conduction band's first half with non-bonding Nb $4d_{xy}$, $4d_{xz}$ and $4d_{yz}$ character, and its last half with antibonding Nb $4d_{x^2-y^2}$ and $4d_{3z^2-r^2}$ energy levels. As the O atom is the most electronegative on the perovskite, both Na–O and Nb–O bonds' electronic density are centered on it, making the atom the major contributor to VBM. According to the Ligand Field Theory (LFT), the ligands' electrostatic potential with octahedral symmetry divides the five empty Nb 4d orbitals into two groups.

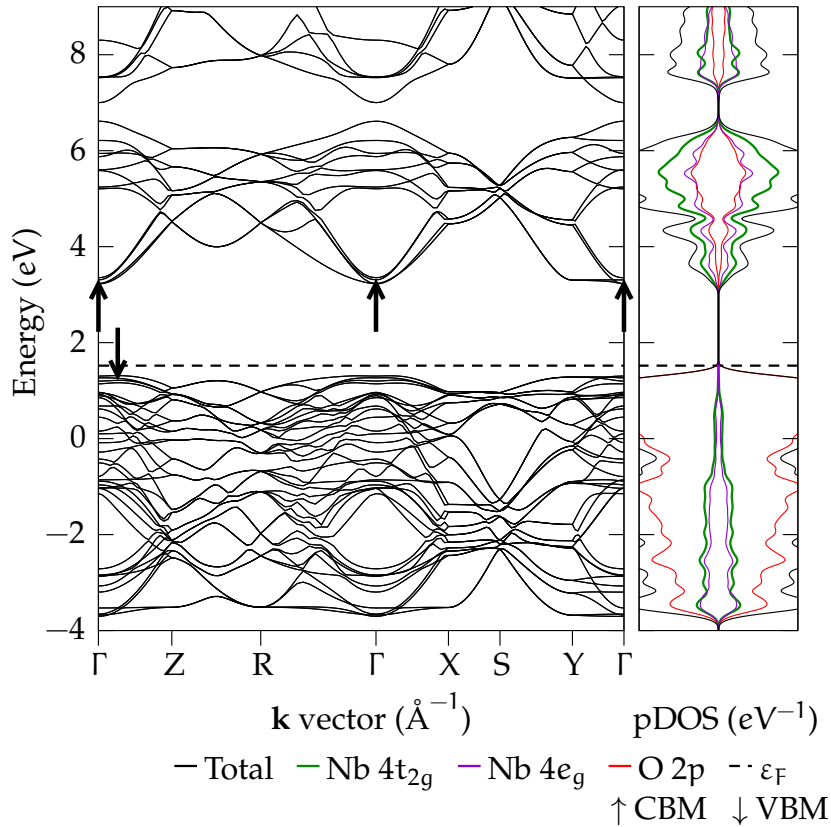
LFT models bonding between two atoms as the constructive interaction between atomic orbitals and a charge transfer culminating in molecular orbitals (MO) [89]. σ type interactions occur over a symmetry axis and are more intense than those over a symmetry plane, called π type interactions. Accordingly, σ interactions govern the chemical complex's electronic structure, while π interactions perturb the MOs [90]. The octahedral symmetry's (O_h) σ interactions acts on Nb 4d orbitals, breaking their isolated-atom degeneracy in two:

- E_g . Coming from $4d_{x^2-y^2}$ and $4d_{3z^2-r^2}$ orbital interactions with O 2p. Where the first Nb orbital interacts with O $2p_x$ and $2p_y$ and the second Nb orbital interact only with O $2p_z$. Both interactions form double degenerate $4e_g$ bonding and antibonding MO;

T_{2g} . As $4d_{xy}$, $4d_{xz}$ and $4d_{yz}$ orbitals are not symmetric to O 2p orbitals, they do not interact and no bonding, or antibonding, MOs are formed. Instead, a non-bonding $4t_{2g}$ MO is formed.

Next, we present our simulations on geometrical and electronic changes caused by point defects and nanometric thin-film surface formation. The thermodynamical equilibrium is correlated to these defects so that their presence will impact every NaNbO_3 application. Also, defect formation directly impacts the system's electronic structure, affecting its photocatalytic activity and performance. To understand these changes, we compared the properties mentioned above with the described pristine relaxed bulk.

Figure 8 – Relaxed NaNbO_3 band structure and pDOS showing the lowermost conduction band composition by Nb 4d levels and uppermost valence band composition by O 2p levels. The up and down arrows point to CBM and VBM, respectively. The horizontal dashed line marks the Fermi level.



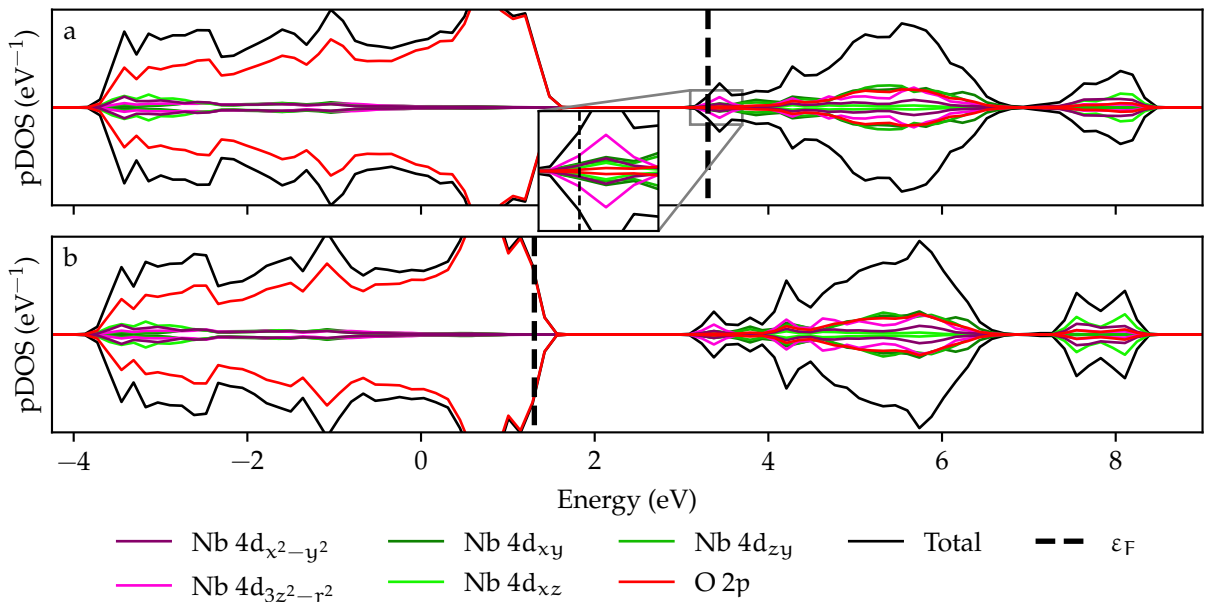
3.2 The Vacancy Formation on Bulk

Vacancy formation control offers an intrinsic way of band structure modification. Defects' influence on host's electronic structure was evaluated on fully-relaxed $3 \times 3 \times 3$ supercell, as spurious defect-image interactions were smaller than on $1 \times 1 \times 1$ and $2 \times 2 \times 2$ supercells (Fig. 26, 28 and 26). Firstly, neutral defects formation was analyzed; then, charged defects. At last, the vacancy formation energy was obtained from Eq. 2.16 fitting for each analyzed point defect and chemical equilibrium in Fig. 5. We discussed which point defect would be more common on the real orthorhombic NaNbO_3 , its impact on the host's electronic structure, and how it would affect the perovskite's water-splitting performance. Limits to the extrapolation method were also discussed.

3.2.1 Neutral Defects

A single apical O atom removal from orthorhombic NaNbO_3 left partially-filled Nb $4d_{3z^2-r^2}$ energy levels 27 meV below the host's conduction band (Fig. 9a). On the other hand, v_{Na}^0 formation left uppermost O 2p defect levels on host's valence band partially depleted (Fig 9b), with energy levels just 10 meV higher than the VBM. Thermodynamical transition levels were obtained for comparison with these KS energy levels. Na–O cleavage while maintaining charge neutrality left neighboring O charge-

Figure 9 – v_{O}^0 (a) and v_{Na}^0 (b) pDOS showing defect level presence inside the band gap. On (a), the Nb–O bond cleavage partially filled the defect levels (see inset graph), while on (b) the Na–O cleavage inserted holes on VBM.



deficient, lowering the Fermi level. On the other hand, Nb–O bond cleavage returned previously shared valence electrons back to Nb 4d defect levels, raising the Fermi level. An O atom removal also cleaved highly ionic Na–O bonds, but antibonding Na 3s orbitals remained empty as their energy were greater than antibonding Nb 4d orbitals. Next, we compared the $3 \times 3 \times 3$ relaxed atomic positions to the pristine bulk.

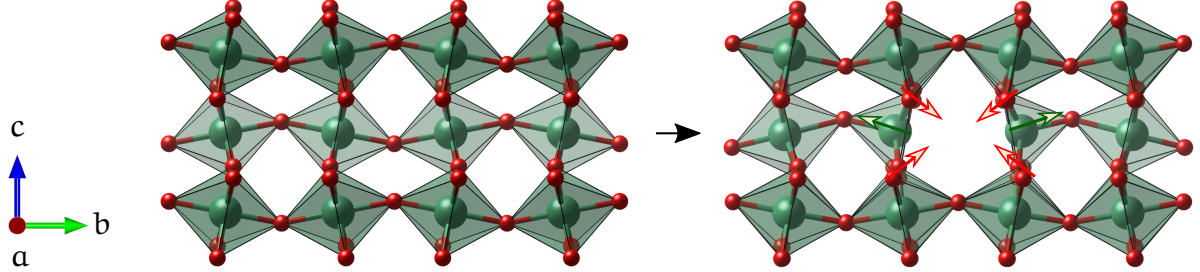
Lattice's response on defect formation was more intense on its nearest neighbors, so we evaluated the distances between the defect center and its first neighbors along with the nearest NbO₆ octahedral angles (Tab. 2). On v_O^0 formation, Nb atoms approached the apical O far from the defect center, while equatorial O moved away from Nb and towards the defect center (Fig. 10). On the other hand, lattice response to v_{Na}^0 formation was significantly smaller. The O atom removal cleaved two partially covalent Nb–O bonds, transforming neighboring octahedra into NbO₅ square-base pyramids. As Nb–O bonds have significant ionic character, their cleavage unbalanced charge distribution and drove the NbO₅ atomic rearrange. The reduction on p – d orbital repulsion from the O_h symmetry break lowered the Nb 4d_{3z²–r²} energy levels below the host's CBM. Atomic displacements agreed with previously discussed differences between bonds: Nb–O cleavage required more significant atomic rearrangement than Na–O, as charge previously shared with O returned to antibonding orbitals. More significant deformations at neighboring lattice came to redistribute charge between remaining Nb–O bonds at the expense of p – d orbital overlap.

The small changes on the host's lattice, the defect-associated wavefunction

Table 2 – The vacancy formation effects on first neighbors' geometry compared to the unrelaxed (pristine) structure.

	v_O^0			v_{Na}^0		
	Unrelaxed	Relaxed	Change	Unrelaxed	Relaxed	Change
d_{v-Na} (Å)	2.810	2.884	+3%	3.951	3.961	+0.2%
d_{v-Nb} (Å)	2.013	2.268	+13%	3.421	3.386	–1%
d_{v-O} (Å)	2.847	2.703	–5%	2.803	2.851	+2%
α [010] (°)	163	164	+1%	163	167	+2%
β [10 $\bar{1}$] (°)	164	152	–7%	164	165	+0.4%
γ [101] (°)	164	176	+7%	164	164	0%

Figure 10 – Projection on the (100) plane of the neighboring atomic arrangement before (left) and after (right) the v_O^0 formation. O atoms (red) approached the vacancy, while Nb atoms (green) retreated from it. Na atoms omitted for clarity.



delocalization, and defect level's proximity to the host's bands would be associated with shallow defect formation on semiconductors [66]. Nevertheless energy levels associated with v_O defect can not be classified from these pieces of information alone as KS energy levels are underestimated. If partially filled v_O^0 defect levels could behave as shallow donor levels; they would increase free charge density at room conditions. An increase in photocatalytic activity by n-type doping has been shown on other transition-metal oxides [91], as filled defect state levels were close to the host's CBM [92].

3.2.2 Charged Defects

A two-electron removal from the O vacancy (Fig. 11a) and a single-electron addition to the Na vacancy (Fig. 11b) altered both vacancies' defect level population, placing the Fermi level close to the VBM. The Nb $4d_{3z^2-r^2}$ defect level became empty with two electron removal on v_O^{2+} formation, while the O 2p level became fully occupied with a single electron addition on v_{Na}^{1-} formation. The band gap description within DFT is problematic, requiring either corrections or post-DFT approaches for adequate p – d orbital repulsion description. Shortcomings on formation energy can be reasonably modeled and compensated with post-processing, but quantities as the band gap and point defect level's energy inside the band gap require further studies with post-DFT methods.

Charged defect's formation effect on first-neighbors' positions was equivalent to neutral defects's influence (Tab. 7 in Appendix A). Shallow defects behave in hydrogenic-like character, weakly binding charges to the vacancy center, as so, their ionization would not drive atomic displacements for compensation. Next, the formation energy

evaluated with $1 \times 1 \times 1$, $2 \times 2 \times 2$, $3 \times 3 \times 3$ supercells were analyzed.

3.2.3 Vacancy Formation Energies

Supercell's volume increase made vacancy centers distance from their images, for $L \rightarrow \infty$, this would result in ΔE_f values without finite-sized supercell artifacts. $\Delta E_f(L \rightarrow \infty)$ estimation for each defect and chemical equilibrium was done by first calculating Eq. 2.11 on $1 \times 1 \times 1$, $2 \times 2 \times 2$, and $3 \times 3 \times 3$ supercells. Then, Eq. 2.16 was fitted to describe the formation energy trend, obtaining the extrapolated value $\Delta E_f(v_X^q; L \rightarrow \infty)$ at each chemical equilibrium provided by NaNbO_3 ternary diagram (Fig. 29 at Appendix A demonstrates the fitting for $\text{O-NaNbO}_3\text{-NaO}_2$ equilibrium).

Extrapolated ΔE_f for v_{Na}^0 (2.49 eV, Fig. 12a) and v_{O}^0 (5.32 eV, Fig. 12b) on O-rich conditions agreed with observed sodium volatility phenomenon in NaNbO_3 growth [93]. Removal of an Na atom cleaves weaker, more ionic bonds than an O atom removal, which breaks Nb–O bonds with relevant covalent character. Na vacancy then required negligible lattice distortions to compensate for the additional free energy from broken bonds. The highly oxidizing environment further eases the Na removal. At the same time, it raises the required energy for O removal. Also, other first-principles findings on similar niobates (ANbO_3) and varying chemical conditions [94] qualitatively

Figure 11 – v_{O}^{2+} (a) and v_{Na}^{1-} (b) pDOS showing defect levels inside the band gap. Inset graph give details about the empty v_{O}^{2+} defect levels.

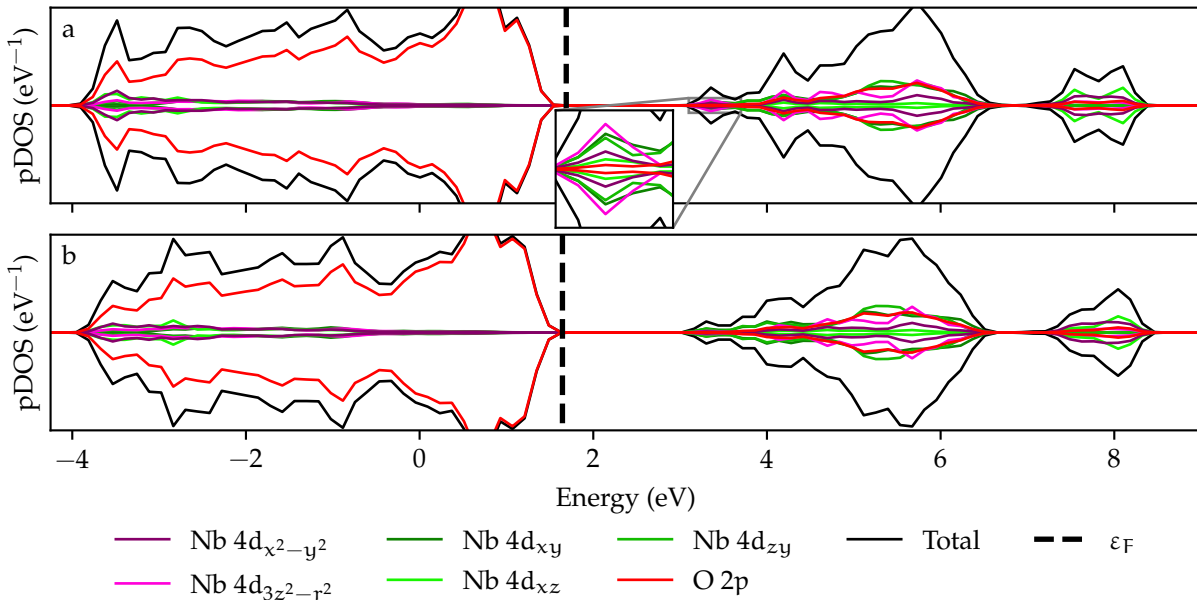
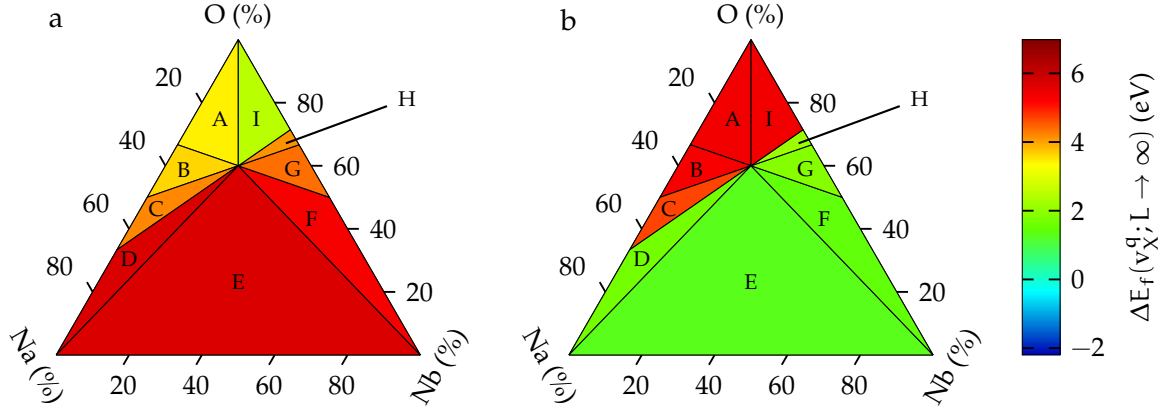


Figure 12 – $\Delta E_f(v_X^q; L \rightarrow \infty)$ for $v_X^q = v_{Na}^0$ (a) and v_O^0 (b) on varying chemical equilibria. Minimal formation energy for v_{Na}^0 at region I was 2.49 eV. Minimal formation energy for v_O^0 at region E was 1.27 eV.

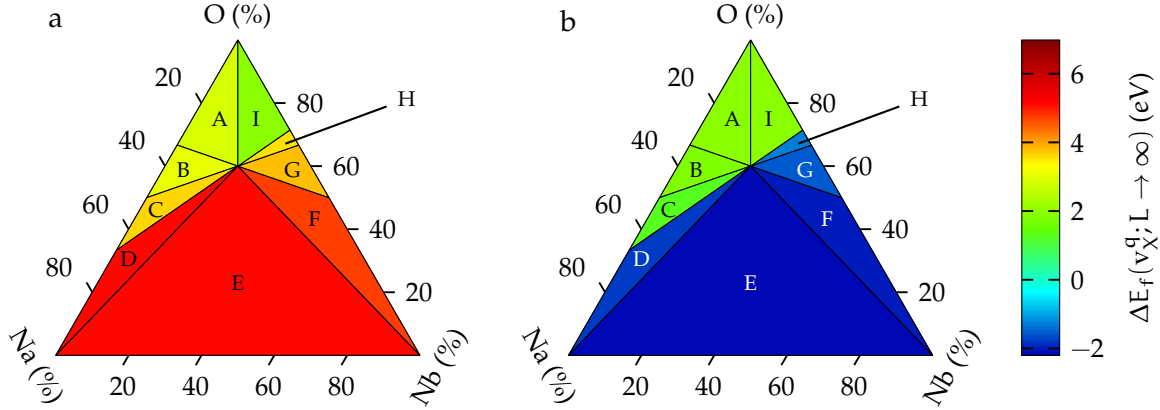


agree with observed trend for v_{Na}^0 : at O-rich conditions, A = Na, K, Li atom removal was energetically more favorable than O atom removal (Fig. 30a on Appendix A). Neutral vacancy formation energies evaluated from the single-supercell approach were smaller than ours, albeit still comparable, due to previously discussed finite-sized supercell artifacts. On O-poor conditions, the ΔE_f trend inverts: v_O^0 formation was energetically more favorable than A atom removal, herein being minimal as 1.27 eV on O-poor conditions. On varying chemical conditions, v_O^0 formation on orthorhombic $NaNbO_3$ were comparable to cubic $NaNbO_3$, $KNbO_3$, and $LiNbO_3$ formations due to equivalent Nb–O bonding on A atom change (Fig. 30b on Appendix A).

Although no relevant lattice relaxation was observed compared to neutral vacancy formation, band filling effects altered ΔE_f making ionized vacancy defects energetically more favorable than neutral states. For the v_{Na}^{1-} , it reduced to 1.92 eV at chemical equilibrium I (Fig. 13a); while for v_O^{2+} , it lowered to –2.14 eV at chemical equilibrium E (Fig. 13b). Contrast between neutral and charge defects at the same chemical conditions gave an 23 % reduction for Na vacancies and an 268 % decrease for O vacancies. For all evaluated chemical equilibria, v_{Na}^0 were more favorable than v_{Na}^{1-} while for O vacancies the ionized state were favored over the neutral.

From these $\Delta E_f(v_X^q; L \rightarrow \infty)$, a better approach for the vacancy energy level evaluation could be done. The thermodynamical transition level for the Na vacancy was $\varepsilon_{Na}(0/1-) = 1.33$ eV, while for the O vacancy it was $\varepsilon_O(0/2+) = 3.62$ eV. On DFT band gap (1.91 eV), $\varepsilon_{Na}(0/1-)$ pointed to a v_{Na} deep defect level at its upper half

Figure 13 – $\Delta E_f(v_X^q; L \rightarrow \infty)$ for $v_X^q = v_{Na}^{1-}$ (a) and v_O^{2+} (b) on varying chemical equilibria. Minimal formation energy for v_{Na}^{1-} at region I was 1.92 eV. Minimal formation energy for v_O^{2+} at region E was -2.14 eV.



but $\varepsilon_O(0/2+)$ was inside the conduction band. On experimental band gap (3.42 eV), $\varepsilon_{Na}(0/1-)$ places the defect level on its first half, which is reasonable for an deep acceptor-like defect level but $\varepsilon_O(0/2+)$ was still 0.2 eV more energetic than the CBM. Transition levels outside the band gap suggest charge states which can not be reached, limiting O defect ionization to the v_O^{1+} state.

The considerable $\Delta E_f(v_O^{2+}; L \rightarrow \infty)$ reduction and a transition level inside the host's conduction band could point to either a DFT modeling problem or an unstable vacancy state. The ΔE_f problem persists with the commonly adopted Freysoldt–Neugebauer–Van de Walle (FNV) correction for charged defects simulated with GGA-PBE [77]. On the $3 \times 3 \times 3$ supercell, where the crystal potential approaches the pristine behavior far from the defect (last row of Fig. 27 in Appendix A), v_O^{2+} corrected formation energy was -2.21 eV at chemical equilibrium E – being even further from positive values – with associated thermodynamical transition level $\varepsilon_O(0/2+) = 3.42$ eV – a few dozens of meV above experimental CBM.

Studies analyzing O vacancy formation both on other niobates [94, 95] and on transition metal oxides [96, 97] also obtained negative formation energies on O-poor conditions. Because of this, it seems reasonable to relate the negative formation energy to the DFT precision on defect level description. An underestimation on p – d orbital repulsion directly impacts the antibonding Nb 4d energy levels, erroneously describing them as less energetic than experimentally described. Because of this, ε_F would also be underestimated, as it is defined at the CBM on $T \rightarrow 0$.

The experimental band gap use on formation energy would be enough to describe an positive value of $\Delta E_f(v_O^{2+}; L \rightarrow \infty) = 0.88 \text{ eV}$. This rough estimation with improved ε_F could be further refined by new simulations using band gap correction methods such as meta-GGA. The meta-GGA methods implement second-order terms to the LDA exchange-correlation potential [98], requiring computational efforts comparable to the GGA-PBE to achieve band gaps closer to experimental values. However, $\varepsilon_O(0/2+)$ would still be placed inside the conduction band, as meta-GGA corrections would be similar for v_O^0 and v_O^{2+} defects.

Vacancy formation energy evaluation with Eq. 2.11 depends on two assumptions: that μ_X and ε_F are independent variables, and that μ_X change occurs without effects on transition energy levels, pinning ε_F on them. Under a closer look, μ_X change should affect ε_F : chemical potential variation affects defect concentration that, on finite temperatures, alters the number of free charge carriers on valence and conduction bands, determining the system's Fermi level. For v_O^{2+} then, μ_O evaluated at E through H equilibria could leverage defect concentration on high enough values for the two assumptions violation, raising ε_F enough to make $\Delta E_f(v_O^{2+}; L \rightarrow \infty) \geq 0$. Fermi levels $\geq 2.55 \text{ eV}$ should progressively turn $\Delta E_f(v_O^{2+}; L \rightarrow \infty)$ positive with μ_O decrease from H equilibrium, becoming $\varepsilon_F \geq 3.05 \text{ eV}$ at E equilibrium. However, these are rough estimations from the same problematic assumptions. New studies should evaluate ε_F from the electrostatic equilibrium at finite temperatures, treating valence band states as effective donor levels and conduction band states as effective acceptor levels together with O vacancy donor states, correctly describing a possible v_O^{2+} mechanism [99].

Chemical conditions control effectively selects the vacancy formation on the niobate: on O-rich conditions, such as the $\text{Nb}_2\text{O}_5 - \text{NaNbO}_3 - \text{O}$ equilibrium, v_{Na}^{1-} is leveraged against v_O^{2+} ; while on O-poor conditions, such as the $\text{Nb} - \text{NaNbO}_3 - \text{Na}$ equilibrium, v_O^{2+} is leveraged against v_{Na}^{1-} . Further studies can better describe the point defect's electronic properties on orthorhombic NaNbO_3 , including the ionization energy description, relevant for experimental defect identification and classification as a shallow or deep state. From our results, it is expected that both vacancies would insert deep defect levels on NaNbO_3 band structure.

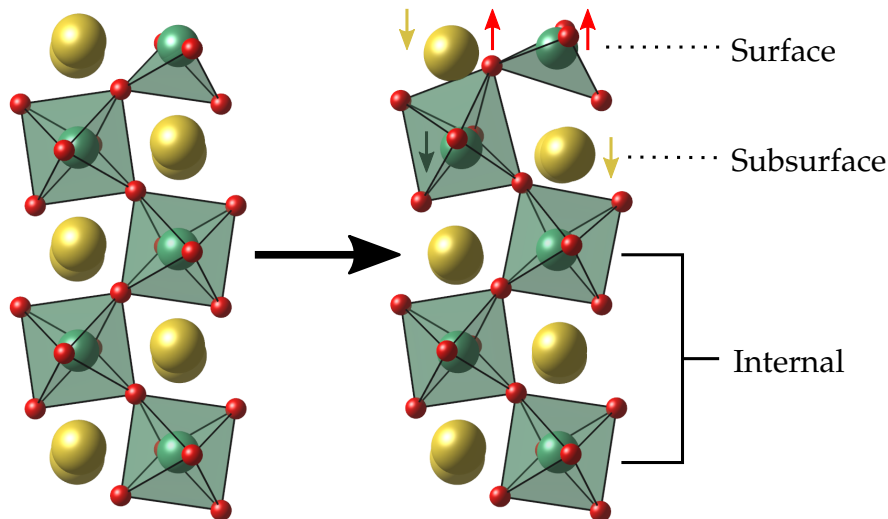
3.3 The [100]-oriented, NaNbO Terminated Thin-film

Ceramic processing into thin-films allows for electronic properties' modification through surface state formation. Also, it allows crystal lattice straining to fine-tune the ceramic properties. As expected, thin-film's response to surface formation after atomic positions' complete relaxation was more intense on outermost layers than on innermost ones. To quantitatively evaluate this effect, we grouped the thin-film atomic layers according to the depth from the cleavage plane (Fig 14):

- **Surface:** the outermost atomic plane;
- **Subsurface:** the atomic layer below the surface layer;
- **Internal:** the region between the third atomic plane from cleavage plane to slab's symmetry plane.

Key quantities chosen for comparisons to the bulk structure (Tab. 3) were: the average Nb–O bond distance $d_{\text{Nb-O}}$, angles between vertex-sharing Nb polyhedra (Fig. 4), deformation index Δ_d for NbO₆ octahedra (Eq. 2.9), and the planarity index P_L (Eq. 2.10) for surface tetrahedra. Ground state geometry was determined with full atomic relaxation of slabs with varying b and c lattice parameters (Fig. 40 in Appendix B): b and

Figure 14 – On the thin-film formation instant (left), outermost Na (yellow), Nb (green) and O (red) species rearranged (right) in new positions (colored small arrows). The outermost layers — labeled surface and subsurface — changed more than the innermost ones — labeled internal layers. As the bottom layer was the slab's symmetry plane, half of it was omitted for clarity.



c parameters 1% greater than bulk's minimized the slab's total energy. Discussion over thin-film effects was carried over the slab geometry, which gave the system's ground state instead of strain-free configuration. A slab built from three repetitions of the bulk's conventional cell was considered adequate to simulate surface effects on the ground state and strained thin-films. A study on the slab thickness's effect on crystal lattice and electronic structure properties was done in Section 3.3.1.

The internal region's response to surface formation closely resembled the bulk structure under tensile strain (Tab. 3). With this in mind, we focused on surface and sub-surface layers' response to the surface formation mechanism. Cleavage of two Nb–O bonds dislocated two O atoms, originally in-between the surface and subsurface layer, closer to the surface layer (Fig. 14). Hence, both layers' Nb–O polyhedra deformed to adjust O dislocation. Surface NbO₄ distorted from the butterfly geometry to an in-between the regular tetrahedron and the regular square planar geometries, equating the electrostatic repulsion from electrons previously associated with the Nb–O bonds with the prejudice on p – d orbital overlap on remaining Nb–O bonds. Also, subsurface NbO₆ octahedra became more deformed with an α angle decrease on [010] direction. From surface formation mechanisms on ionic solids' literature [29], atomic displacements occurs for electron density redistribution. Next, we employed the Atoms In Molecules (AIM) approach to evaluate this charge redistribution.

A perfectly Nb–O ionic bond would transfer all five valence electrons equally to the six O ligands. The cleavage of two Nb–O hypothetically ionic bonds on (100) sur-

Table 3 – Description of Nb–O bonds in the three thin-film's regions compared to bulk values (in parenthesis). Surface relaxation induced atomic displacements at the surface and subsurface layers, mostly preserving internal layers.

	Surface		Subsurface		Internal	
	$P_L = 75\%$		$\Delta_d = 6\%$		$\Delta_d = 3\%$	
$d_{\text{Nb-O}} (\text{\AA})$	1.97	(–2.2%)	2.06	(+2.3%)	2.03	(+1.0%)
$\alpha [010] (^{\circ})$	149	(–8.6%)	155	(–4.9%)	162	(–1.0%)
$\beta [10\bar{1}] (^{\circ})$	177	(+7.9%)	176	(+7.3%)	175	(+6.7%)
$\gamma [101] (^{\circ})$	177	(+7.9%)	176	(+7.3%)	175	(+6.7%)

face formation would add $2 \times \frac{5}{6} = 1.67$ electrons to the Nb valence. Valence electrons count would be higher when considering Ligand Field Theory, which predicts a covalent character to the Nb–O bonds. With AIM approach, we evaluated an average of 8.92 electrons on surface layer Nb (Fig. 15). As Nb $4p^6$ electrons were explicitly simulated from the atom's core-shell, subtracting them gave 2.92 valence electrons, expressing a contribution from ionic and covalent bonding. As Nb $4d$ orbitals have an antibonding character, weakly binding electrons to the cations, transferred charges became delocalized. This delocalization comes from a smaller Nb electronegativity compared to O, not enough to stabilize a localized charge excess, and also from small atomic displacements, which were not enough to form new bonds. Instead, electrons remained mobile, driving a profound charge redistribution which raised electron counting in the subsurface and internal regions. The (100) surface formation also cleaved Na–O bonds, altering Na and O charge counting relative to bulk (Fig. 31 in Appendix A), however they were secondary to the Nb changes. From the electronic structure's perspective, delocalization induced a surface metalization. Next, we analyzed the thin-film's pDOS and discussed surface metalization implications on photocatalytic activity.

Layer-resolved pDOS showed that surface (Fig. 16a) and subsurface energy levels

Figure 15 – Charge counting change on Nb (green) species at each thin-film's atomic layer compared to the average charge on bulk. Cleavage on (100) plane increased charge counting on the surface. Inner atomic layers also had more charge than bulk.

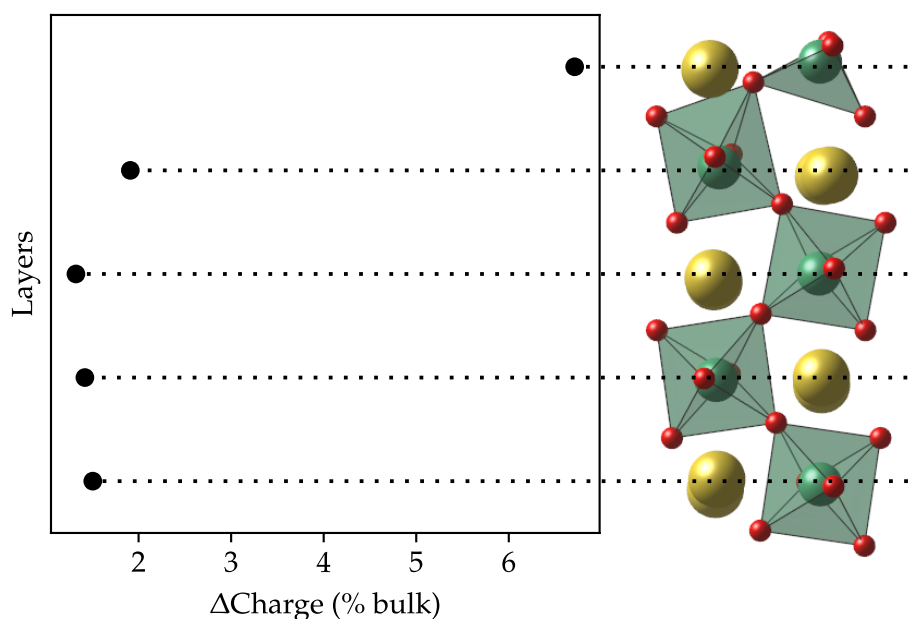
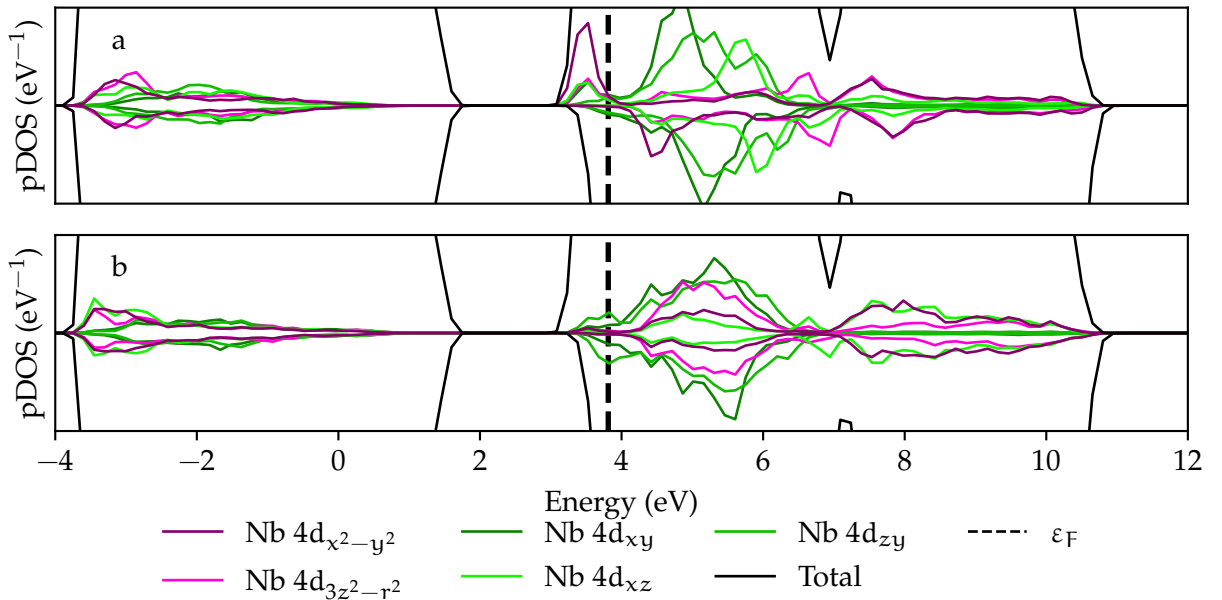


(Fig. 16b) were partially filled, giving the previously discussed surface metalization. As geometric changes on the surface and subsurface layers were more significant than on internal, we left the latter's region pDOS in Appendix A (Fig. 32) and focused on the first two's response. Surface, and to a minor extent also subsurface, energy levels developed a spin polarization. The surface Nb $4d_{x^2-y^2}$ up and down levels differs 1.75 eV in energy, giving a total spin momentum of $3.95 \mu_B$. Our slab had four Nb cations on the surface layer, each contributing $0.99 \mu_B/\text{at.}$ to the total. This electronic configuration can be understood with the Ligand Field Theory.

To explain this thin-film's electronic structure, we split its formation into two main events. In the first, two equatorial Nb–O bond cleavages from octahedral NbO_6 formed an butterfly-shaped NbO_4 [89], which stabilized $4d_{x^2-y^2}$ orbitals relative to $4d_{3z^2-r^2}$. Charge previously from O 2p orbitals then populated non-bonding $4(d_{xy} d_{xz} d_{yz})$, which remained degenerate in butterfly configuration. These orbitals' partial population made them susceptible to the Jahn-Teller effect, which spontaneously broke their degeneracy and geometry closer to the tetrahedral form. Finally, the new geometry induced a partial σ overlap between O $2(p_x p_y)$ and Nb $4(d_{xz} d_{yz})$ orbitals, which raised 4d energy levels well above the $4d_{xy}$ level, favoring the last's filling with electrons. In the second event, the NbO_4 rearrangement deformed underlying subsurface NbO_6 octa-

Figure 16 – Layer-resolved pDOS of Nb species in surface (a) and subsurface (b) layers. Energy levels aligned to bulk's lattice potential. The dashed lines mark the Fermi level. Lowermost surface up-states near the CBM were filled, while down-state pairs remained empty.



hedra, inducing an O $2p_x$ orbital overlap with Nb $4(d_{xy} d_{xz})$. Spatial and energy levels' proximities then favored a charge density transfer from surface Nb $4d_{xz}$ to subsurface Nb $4d_{xz}$. At last, subsurface Nb $4d_{xz}$ and internal Nb $4(t_{2g})$ energy levels' proximity and wavefunction overlap delocalized this transferred charge density across the thin-film's width.

The reduced energy difference between surface Nb $4d_{x^2-y^2}$ and $4d_{xz}$ orbitals favored the $4d_{x^2-y^2}^1 4d_{xz}^1$ (high-spin) electronic occupation. At the same time, charge transfer to subsurface Nb $4d_{xy}$ assumed a minority-spin orientation, suggesting an exchange interaction between surface and subsurface Nb. Nevertheless, a better understanding of the exchange mechanism depends on an adequate description of electron interaction, which requires either correction to DFT overestimated d orbital delocalization or a direct approach for the electronic interaction with a perturbation theory. Albeit spin polarization has been shown to reduce charge recombination, which improves the material's photocatalytic efficiency [100], this perovskite's surface metalization would restrict water-splitting activity.

The photocatalytic activity promotes a valence electron to the conduction band when both VBM and CBM are aligned with oxiredution potentials. Then, excited electron (hole) decays to hydrogen (oxygen) evolution reaction's level under adequate conditions, catalyzing the water-splitting reactions. On this thin-film surface orientation, this state is the ground state. Then there is no thermodynamic driving force for the thin-film's electron participation in water-splitting. In Section 3.3.2, we investigate the biaxial strain effect on the thin-film.

3.3.1 Surface Effects' Sensibility To Slab Width

Previously, we investigated how the orthorhombic NaNbO_3 crystal and electronic structures would change with nanometric thin-film processing with a slab build from three repetitions of bulk's conventional cell along $[100]$ direction. Herein, we compare these results to those obtained in varying slab widths and from an infinite surface model, reproducing the surface equilibrium with bulk's structure by fixing the slab's middle region atomic positions.

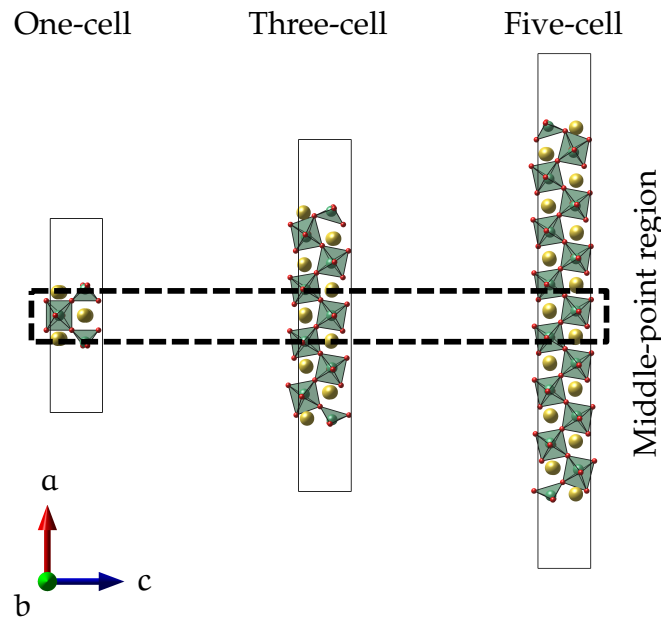
All atomic positions were allowed to relax on the slabs modeling one (26 atoms),

three (86 atoms), and five conventional cells (146 atoms) thin-films (Fig. 17). We refer to them as one-cell, three-cell, and five-cell slabs, respectively, from now on. Ground state lattice parameters were also obtained for the one-, three-, and five-cell width thin-films by minimizing their total energy in respect to volume (Figs. 39, 40 and 41 on Appendix B, respectively). All supercells shared the same 15 Å vacuum width, isolating slabs on a direction.

The slab modeling the infinite surface was obtained from repeating the bulk's conventional cell three times along the [100] direction with fixed lattice parameters. Before this surface slab's relaxation, atomic positions inside the conventional cell at the middle point region (Fig. 17) were fixed, retaining the relaxed bulk's crystal structure. Surface formation effects on ionic solids generally are concentrated in outermost layers, recovering the bulk configuration sufficiently far from the cleavage plane [101]. This behavior can be modeled on the supercell approach by either converging the surface energy in respect to the slab's width or by fixing the middle region's atomic positions [81], the latter being computationally less intensive.

The ground state's crystal structure changed with thin-film width. In a one-cell thin-film, total energy was minimal with lattice parameters identical to the bulk. In

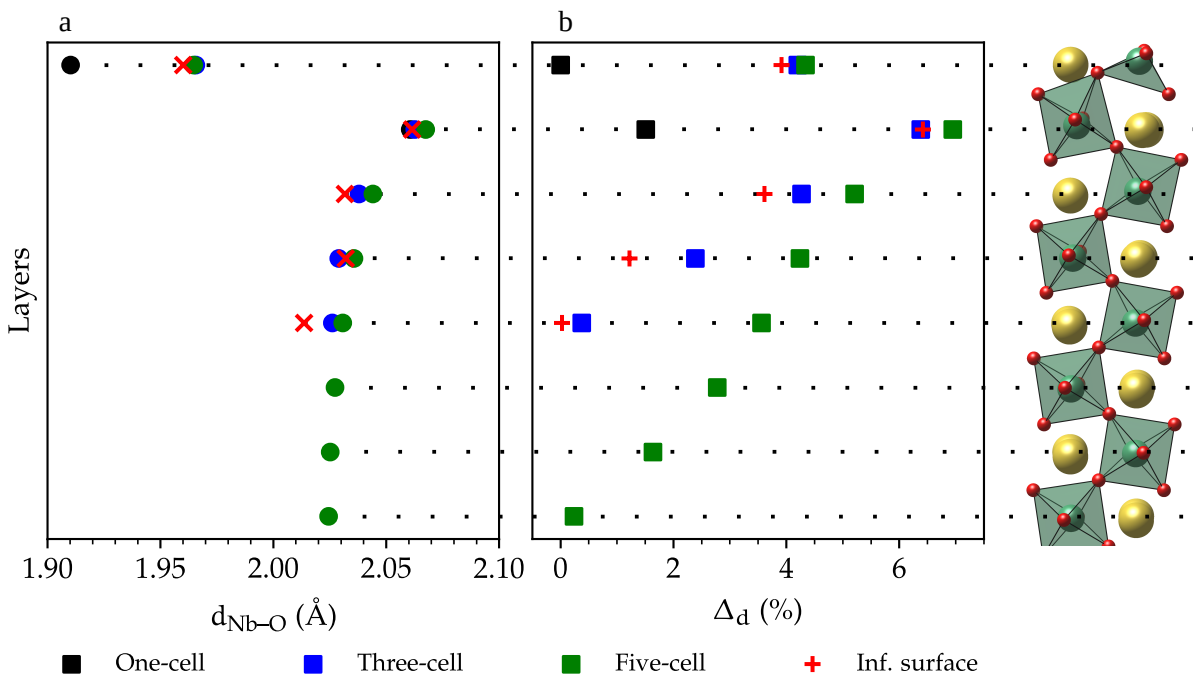
Figure 17 – Slabs were built to model the thin-film formation with varying widths in a relaxed state, where the dashed box demarks the middle-point atomic layer. The infinite surface slab had the exact dimensions as the three-cell slab, but its middle region's atomic positions were fixed.



both three- and five-cell thin-films, total energy was minimal with lattice parameters 1% greater than the bulk. Increased lattice parameters induced changes on average Nb–O bond lengths $d_{\text{Nb-O}}$ (Fig. 18a) and NbO_6 distortion index Δ_d (Fig. 18b). Surface NbO_4 deformation index and bond length increased with the thin-film's width, closing to the infinite surface's values. The same trend was observed with the planarity index (Eq. 2.10): from $P_L = 71\%$ on one-cell thin-film, it became 75% on all three-cell, five-cell, and infinite surface. Subsurface layers on three- and five-cell also had $d_{\text{Nb-O}}$ and Δ_d values close to the infinite surface's ones. At last, both parameters' change on three- and five-cell internal regions depended on slab width. Nevertheless, both approached infinite surface's $d_{\text{Nb-O}}$ and Δ_d values on the middle-region. From the geometrical perspective, the outermost layers on three- and five-cell thin-films behavior matches the infinite surface's as their lattice parameters were allowed to increase, hinting that surface formation were similar both at thin-film and infinite surface conditions. Next, we compared the slabs' electronic states to the infinite surface.

Except for the one-cell slab, spin polarization and surface state partial filling on thin-films' surface layer (Fig. 19a, b, and c) were similar to the infinite surface's (Fig. 19d). Subsurface atomic layers from three- and five-cell thin-films (Fig. 19e, f,

Figure 18 – Layer-averaged bond distances (a) and distortion index (b) evolutions with the atomic layers increase. $d_{\text{Nb-O}}$ and Δ_d layer values referenced to the slab at the right.

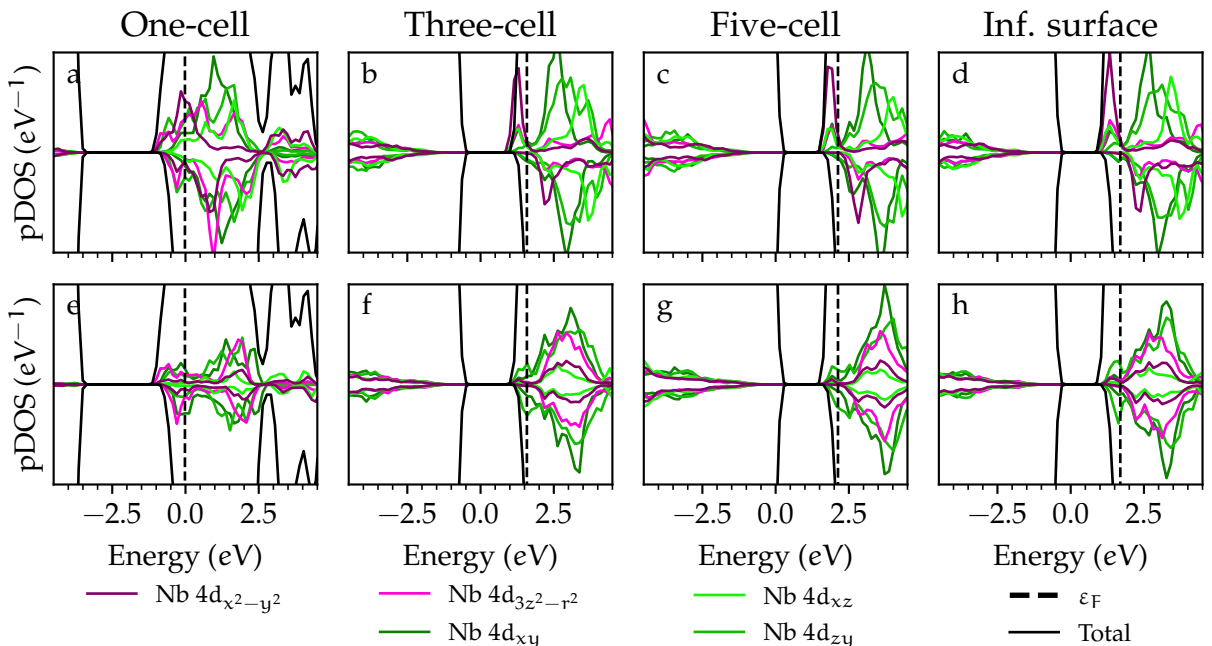


and g) were also similar to infinite surface response (Fig. 19h). The chosen cleavage plane removes two Nb–O bonds, stabilizing the Nb $4d_{x^2-y^2}$ energy levels below the Nb $4(d_{xy}, d_{xz}, d_{yz})$ -dominated CBM. Charge excess then occupied surface spin-up Nb $4d_{x^2-y^2}$ and spin-down Nb d_{xz} levels, raising the Fermi level. Thin-films' electronic structure resemblance to the infinite surface resulted from a well-behaved surface formation with width increase. Again, except for the one-cell slab, internal layers' increase in number did not influence surface effects. As so, the slab built from three conventional cells was sufficient and necessary to study surface states on both strained and unstrained thin-film configurations. If quantum confinement effects were relevant, we would observe more significant differences between occupied and empty states, as happened on the one-cell slab.

3.3.2 Biaxial Strain Effects

The properties' modulation with biaxial strain comes from atomic displacements imposed by elastic strain. Herein, the biaxial strain was simulated by changing the slab's perpendicular lattice parameters, b and c , in 1% steps between $[-5\%, 5\%]$. As done previously, we grouped results on the surface (Fig. 20a), subsurface (Fig. 20b) and internal regions (Fig. 20c). Globally, compressive (tensile) strain decrease (increase) the

Figure 19 – Surface (a, b, c, d) and subsurface (e, f, g, h) pDOS for each analyzed slab and infinite surface (columns) showing the width effect on Nb 4d states.



NbO_4 P_L while increase (decrease) the NbO_6 Δ_d parameters. The atomic rearrangement changes the $p - d$ orbital overlap, altering charge distribution over atomic planes and the thin-film's band structure.

Electron redistribution with strain occurred mainly on surface's and subsurface's Nb cations (Fig. 21). The observed decrease in surface's planarity with compressive strain came with an excess charge on the subsurface layer, while the opposite happened with tension. Besides, internal layers' charge weakly changed with strain. We also evaluated the biaxial strain effects on O and Na atoms (Fig. 33a and b), but their strain response were significantly smaller than the Nb.

In general, an increase in Δ_d — and a decrease in P_L — was followed by an energy level increase. As the distorted tetrahedral and octahedral symmetries describe the ground state configuration, symmetry-breaking compressive (tensile) strain increased (decreased) the $p - d$ overlap, globally increasing (decreasing) the surface's energy levels (Fig. 22). These surface electronic states were sensible to strain but not enough to change the thin-film's electronic character: compressive strain minimized surface charges, yet they remained non-zero. On -5% strain, the thin-film's magnetic momentum was $2.23 \mu_B$ and the energetic separation between opposite-spin energy levels was 0.18 eV , minimizing both (Fig. 22a). On the other hand, on 5% strain state, the thin-film's magnetic momentum was $4.48 \mu_B$ and opposite-spins energetic separation was 0.51 eV (Fig. 22c).

Figure 20 – Biaxial strain effects on NbO_4 and NbO_6 geometries described by surface's planarity P_L (a) and Baur's distortion index Δ_d for subsurface (b) and internal regions (c). In general, an increase of tensile (compressive) strain makes those atomic arrangements closer to (further from) the ideal geometry.

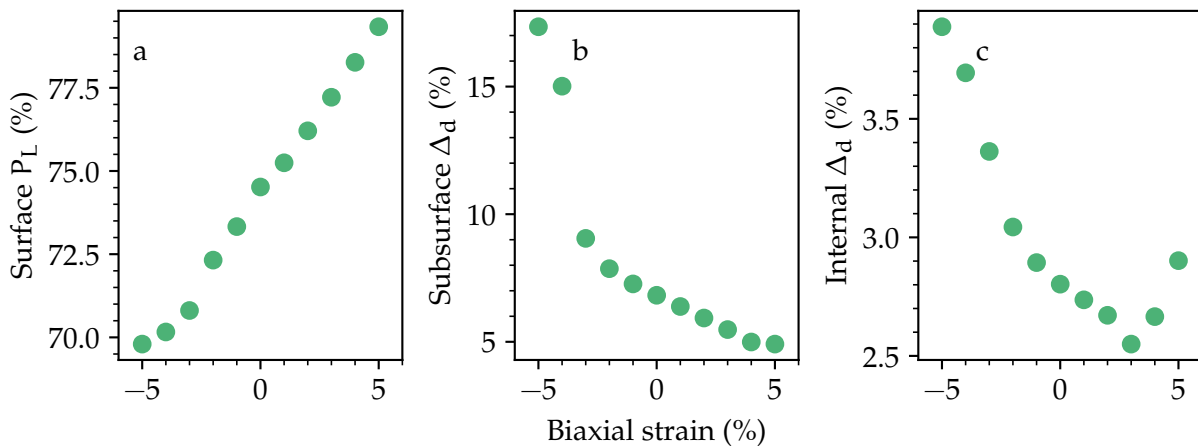
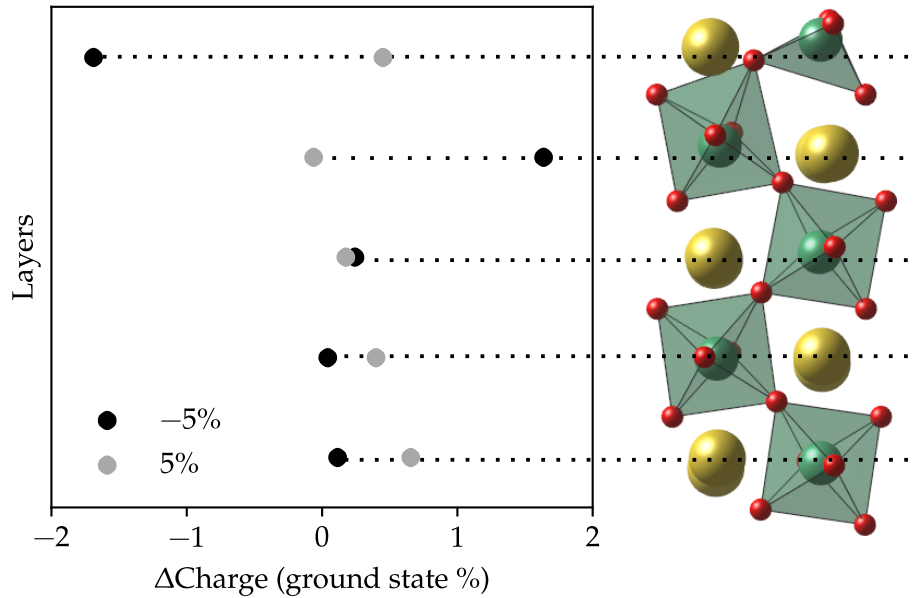


Figure 21 – Biaxial strain effect on layer-averaged charge over Nb (green) atoms. The layer-averaged charge as compared to the thin-film's ground state (1% tensile strain). With tension (compression) increase came the surface's charge increase (decrease) at the expense of subsurface's one.

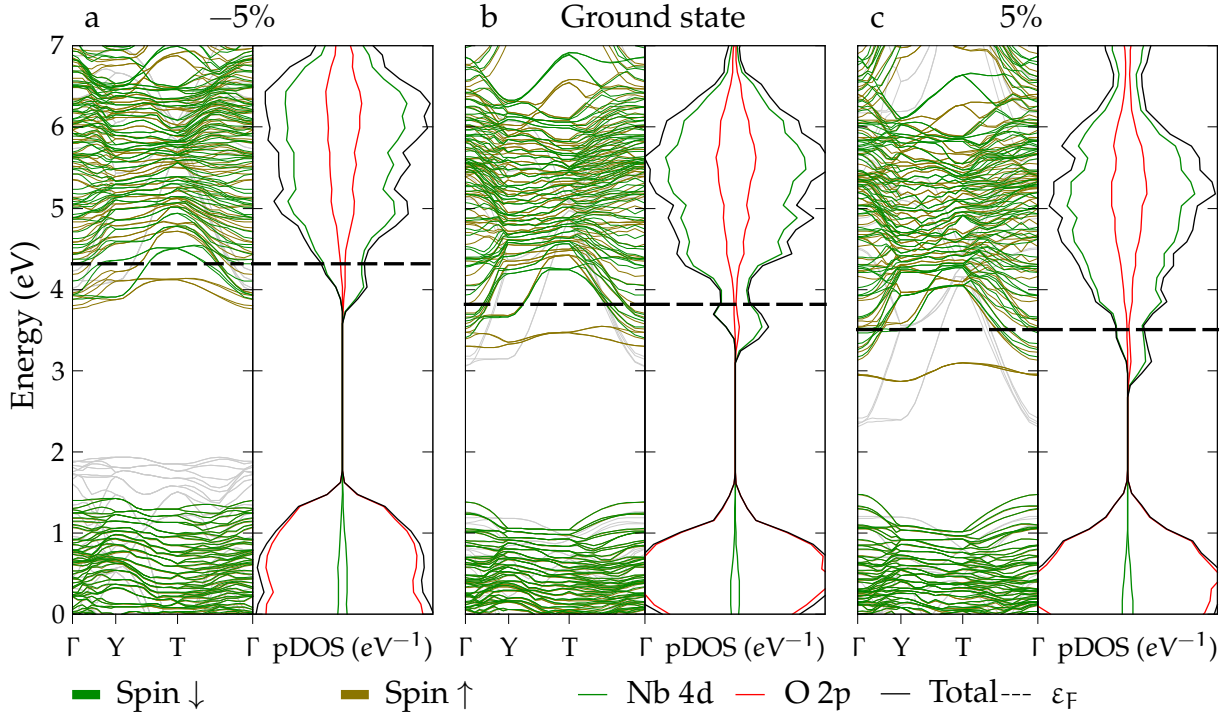


In conclusion, bulk's semiconductor character could not be recovered by biaxial strain alone. The vacancy examination on bulk revealed that this defect type could alter the system's Fermi level. Interaction between surface states with these defects could change the thin-film's electronic properties. Recent works had obtained improved photocatalytic methyl blue degradation by tailoring oxygen vacancy concentration on orthorhombic NaNbO_3 surface. Oxygen vacancy formation inserted defect levels which enhanced visible light absorption [25]. Further studies should characterize these defect levels and their alignment with water-splitting reaction potentials. Next, a comparison with orthorhombic NaNbO_3 was made, highlighting changes set off from the transition metal change.

3.3.3 Comparison With NaTaO_3 Thin-film

Perovskite properties heavily depend on the octahedron-centering transition metal's chemical nature. This dependence can be understood by comparing perovskites with the same alkali metal, equivalent crystal structure, and surface termination. Both Ta and Nb atoms are at the periodic table's group 5, sharing the same number of valence electrons. As Ta is in the row below Nb, its increased atomic volume better shields

Figure 22 – Band structure and pDOS of the thin-film on (a) $\epsilon = -5\%$, (b) ground state ($\epsilon = 1\%$) and (c) $\epsilon = 5\%$ strain states. Gray bands are projections of bulk bands at the thin-film's cleavage plane and strain state, referenced to the band alignment.



the nucleus electrostatic potential, resulting in an energetically more intensive electron addition and easier electron removal. Element's electronegativity is correlated to this interaction energy [102]: Ta atom's electronegativity is smaller than Nb. Herein, surface formation effects on orthorhombic NaTaO_3 and NaNbO_3 nanometric thin-films were compared to clarify the electronic structure changes on the ground and biaxially strained states.

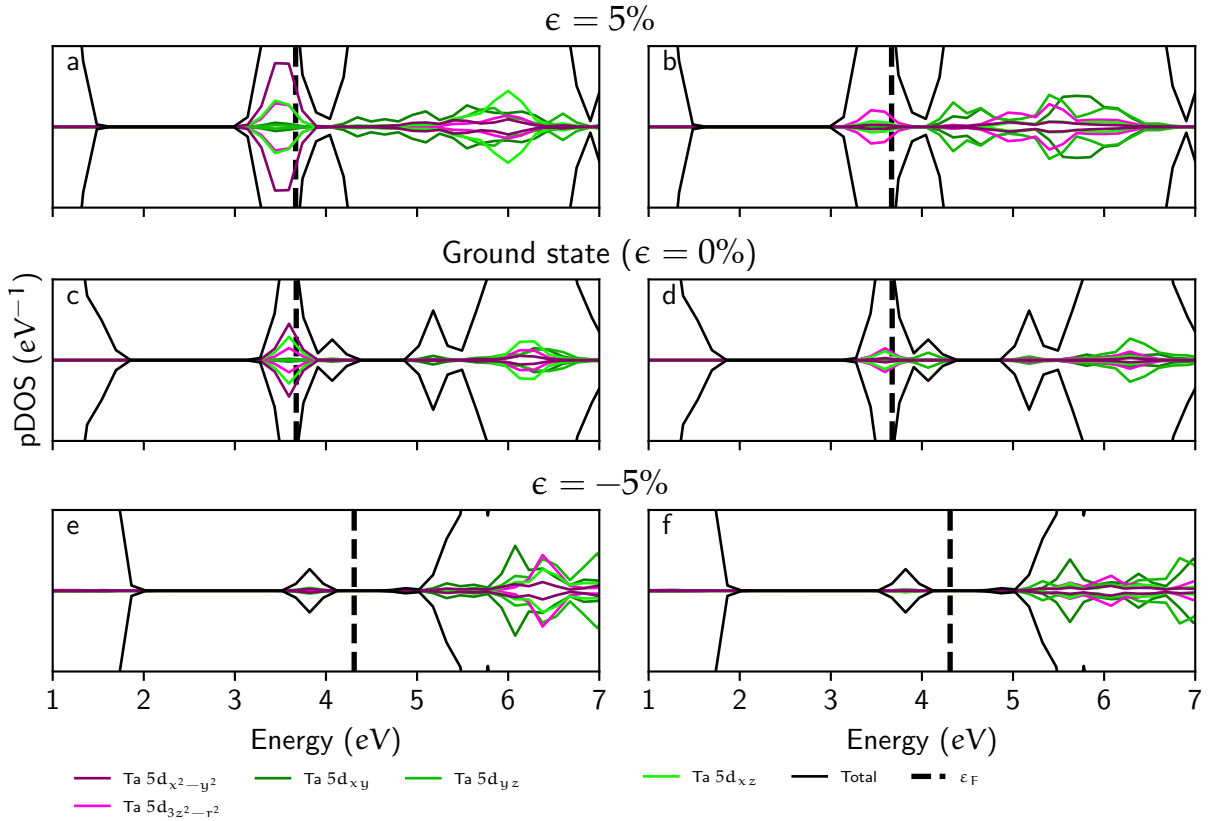
A three-times repeated conventional cell, (100)-oriented slab was build from previously relaxed orthorhombic (Cmcm) NaTaO_3 bulk supercell. Slab thickness choice was based on comparability with previously described NaNbO_3 thin-film. The slab's total energy variation with lattice parameters (Fig. 42 in Appendix B) has shown that minimization occurs with bulk's b and c parameters. The original bulk structure was relaxed with lattice parameters $a = 5.62$ (+2.0%), $b = 7.86$ (+0.9%), and $c = 5.58$ Å (+1.1%). Comparison in parenthesis shows good agreement with experimental measurements [103, 104]. Biaxial strains were modeled in the same way as previously described.

As previously done, the thin-film formation was analyzed on three regions: on

the surface, subsurface, and internal regions. We adopted the notation $M = \text{Ta}, \text{Nb}$ to describe attributes common for NaTaO_3 and NaNbO_3 thin-films, respectively. NaTaO_3 electronic properties' modulation for improved water-splitting was published elsewhere [23]. Band gap correction adopted on reference [23] was removed for comparison with the data obtained for NaNbO_3 on DFT level of theory.

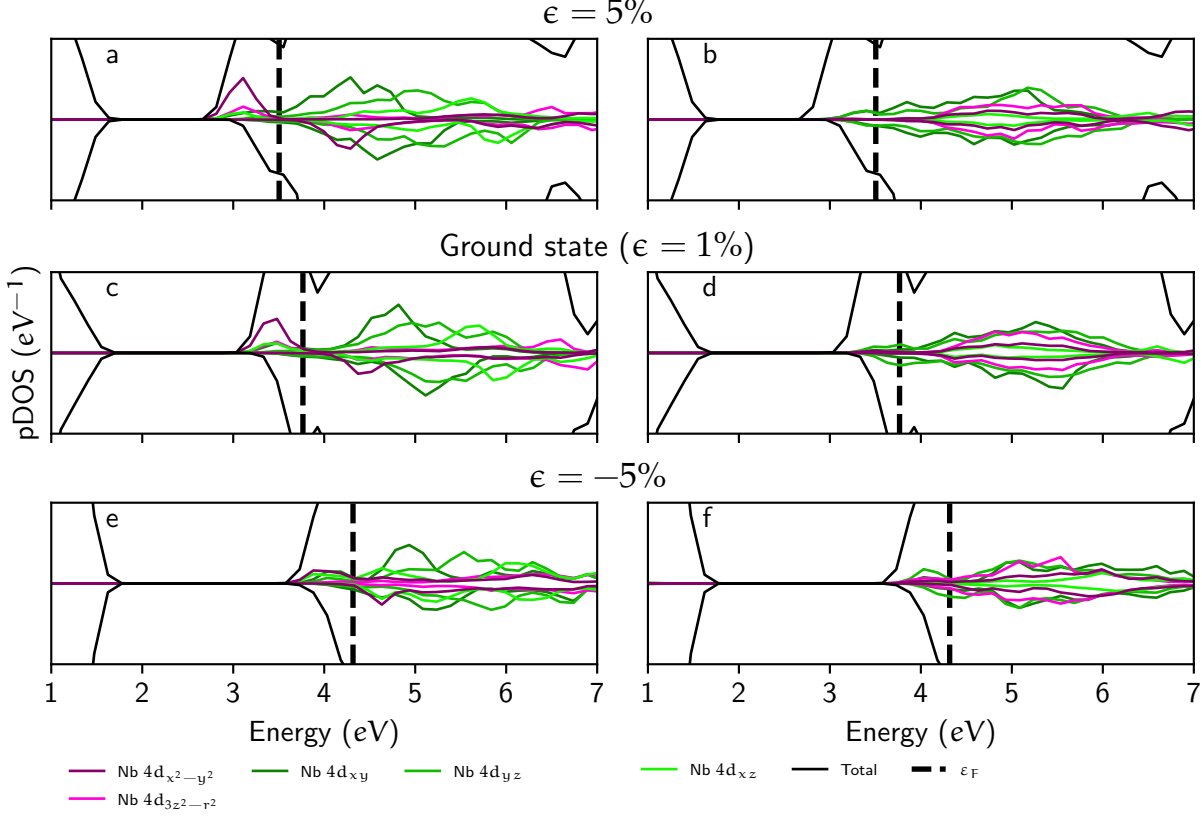
NaTaO_3 simulations shared the same calculus parameters with NaNbO_3 simulations, where the Ta PAW set explicitly simulated electrons from $5p^6 5d^3 6s^2$ orbitals, giving the same number of electrons used on Nb description. Also, Ta 4f electrons were included inside the core region to improve system's convergence with marginal impact on Ta properties description [31].

Figure 23 – NaTaO_3 surface (a, c, e) and subsurface pDOS (b, d, f) on ground state ($\epsilon = 0\%$), $\epsilon = -5\%$ and 5% biaxial strains. The vertical dashed line marks the Fermi level. States aligned with the bulk's lattice potential on the same biaxial strain.



After total relaxation, the thin-films presented surface levels both on the ground state and under biaxial strain. Overall NaTaO_3 surface (Fig. 23a, c, e) and subsurface (Fig. 23b, d, f) pDOS features were distinct from the NaNbO_3 (Fig. 24a, c, e, and b, d, f, respectively). Both perovskites had developed mid-band gap, surface layer-composed

Figure 24 – NaNbO₃ surface (a, c, e) and subsurface pDOS (b, d, f) on ground state ($\epsilon = 1\%$), $\epsilon = -5\%$ and 5% biaxial strains. The vertical dashed line marks the Fermi level. States aligned with the bulk's lattice potential on the same biaxial strain.



energy levels, making them surface levels. Nevertheless, the band's composition, population, energy level, and spin polarization differed. NaTaO₃ lowermost surface states were totally filled, with null magnetic polarization, and 1.0 eV below CBM. On the other hand, NaNbO₃ surface states were partially filled, developing a $3.95 \mu_B$ magnetic momentum, and hybridized with conduction band's edge states, delocalizing the surface states across the thin-film's width. Biaxial strain response also differed: both tensile and compressive strains on NaTaO₃ raised subsurface Ta $5d_{yz}$ energy levels away from filled surface states, while on NaNbO₃ the surface and subsurface states were preserved. Also, the tensile strain on NaNbO₃ raised surface levels further away from bonding O $2p_x$.

Removal of two equatorial O atoms left the surface transition metal cations from both thin-films with an equivalent excess of charge, as evaluated with the AIM approach [46] (Fig. 35 in Appendix A). Without overlap with O $2p_x$ orbitals, $d_{x^2-y^2}$ orbitals from both Ta and Nb surface cations became more stable than antibonding $d_{3z^2-r^2}$ and

Table 4 – Surface formation effects on NaNbO₃ and NaTaO₃ thin-films crystal lattices. The average M–O (M = Ta, Nb) bond distance on each thin-film region was compared to the bulk values (2.041 Å for NaTaO₃ and 2.014 Å for NaNbO₃). Planarity index P_L obtained from average surface O–M–O bond angles compared to ideal 180° value. Distortion index Δ_d obtained from the MO₆ octahedral bond distances variation.

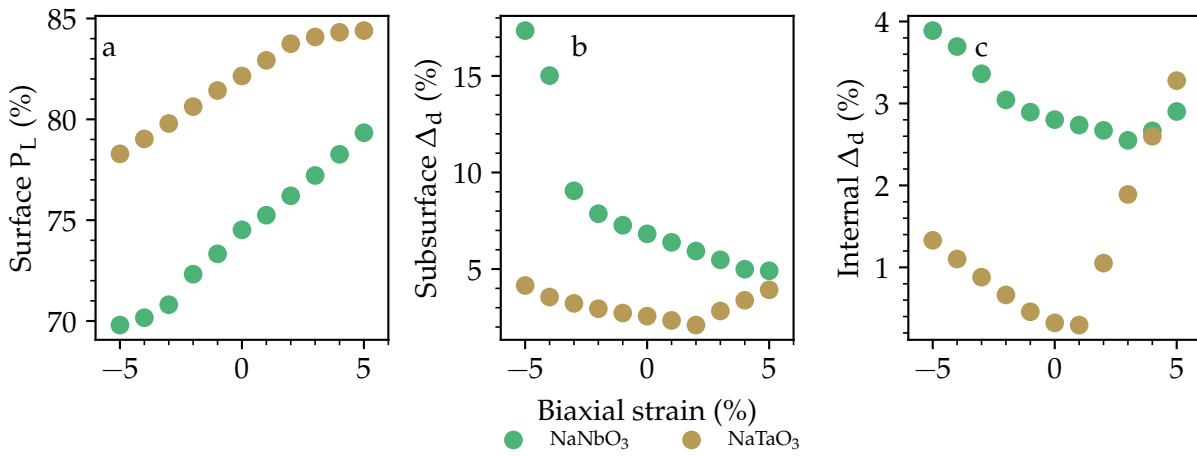
	Surface		Subsurface		Internal	
	NaNbO ₃	NaTaO ₃	NaNbO ₃	NaTaO ₃	NaNbO ₃	NaTaO ₃
Δd_{M-O} (bulk %)	–2.2	–2.3	+2.5	+2.1	+1.0	–0.1
P_L (%)	75	84	—	—	—	—
Δ_d (%)	—	—	6	3	3	0.3

non-bonding d_{xy} , d_{xz} , and d_{yz} , allowing the former's population. However, surface formation on NaTaO₃ was more effective on Ta $5d_{x^2-y^2}$ energy lowering, allowing its complete filling. On NaNbO₃, surface formation stabilized Nb $4d_{x^2-y^2}$ as partially filled, remaining metalized. Under biaxial strain, NaTaO₃ pDOS changed significantly with non-bonding energy levels lowering closer to surface levels. While on NaNbO₃ surface levels remained close to the non-bonding energy levels. Next, we compared geometrical parameters from both thin-films' crystal structures to fully describe the surface formation and compared biaxial response.

Surface formation was analyzed from the perspective of the changes on M–O bond distances Δd_{M-O} , planarity index P_L (Eq. 2.10), and distortion index Δ_d (Eq. 2.9) (Tab. 4). On general terms, atomic rearrangement trends were similar on both thin-films, as two M–O bond cleavages shortened remaining bonds and distorted O–M–O bond angles towards 180°, making the surface MO₄ closer to the square planar geometry. As a consequence, underlying octahedra elongated and distorted, with vanishing effects on internal layers. Nevertheless, strain response differed on magnitude: surface relaxation was more intense on NaTaO₃ and less intense on subsurface and internal regions, while on NaNbO₃ it was less intense on the surface and more intense on subsurface and internal layers.

Then, the surface formation mechanism differs: for the NaTaO₃ thin-film, an increased TaO₄ planarity allowed for favored interactions with the underlying TaO₆, placing the surface levels deep on the band gap, which induces related wavefunctions'

Figure 25 – Biaxial strain response from surface MO_4 planarity index P_L (a), subsurface MO_6 distortion index Δ_d (b) and internal MO_6 Δ_d (c).



localization. On the other hand, charge from cleaved bonds on NaNbO_3 did not achieve the same degree of atomic rearrangement, giving surface levels with energies similar to subsurface and internal layers' Nb 4d, resulting in hybridization and high charge mobility across the thin-film's width.

Thin-film processing allows for electronic structure modulation through biaxial strain, where changes on surface energy levels come from distorting the surface layer MO_4 ligand field. By following surface P_L (Fig. 25a), subsurface (Fig. 25b) and internal Δ_d changes (Fig. 25c) with biaxial strain on NaTaO_3 and NaNbO_3 , it was possible to assert the transition metal influence on lattice response. Common for both thin-films, compressive strain reduced surface P_L and increased both subsurface and internal Δ_d , while tensile strain increased surface P_L and Δ_d values over a critical value. TaO_4 planarity remained higher than NbO_4 on all strain states evaluated, while subsurface and internal TaO_6 distortion indexes remained smaller than NbO_6 values on most strain states evaluated. On Δ_d , small tensile strains — 2% for subsurface and 1% for internal — were enough to increase TaO_6 distortions but higher strains — 4% for subsurface and 3% — were required for NbO_6 octahedra. As observed on ground state surface formation, lattice deformation intensity changed with the transition metal change. Ground state NaTaO_3 surface formation process provoked small deformations on thin-film's TaO_6 , which eases further deformation through strain. On the other hand, the already-deformed NbO_6 response requires higher strain states as the relation between its total energy and volume is quadratic.

4 CONCLUSIONS

In general, a semiconductor's water-splitting activity simultaneously depends on its capability to generate charges with adequate energy and on its conduction properties for their transport to the surface with minimal losses. Herein, we have shown that vacancy formation control perhaps would not increase charge generation, as their transition energy levels are more significant than room conditions' thermal energy. Further investigations could focus on the band gap improved description through beyond-DFT first-principles methods. Besides, better quantitative predictions could further improve ionization energies for the O and Na vacancies, aiding experimental identification of these point defects and fine control over growth parameters.

The other standard approach for band structure engineering, thin-film processing, would also not improve water-splitting activity. Selecting the [100] orientation and NaNbO termination indeed inserted surface states inside the host's band gap, but cleavage of two Nb–O bonds were stable at a metallic, spin-polarized configuration. Thin-film's band structure positively responded to biaxial strain, moving surface states away from the conduction band by reducing p – d orbitals overlap. Nevertheless, even extreme biaxial strains could not revert the metalized electronic structure to the original semiconductor state.

Contrast to closely related sodium tantalate highlighted the role of Nb electronegativity on NaNbO₃ thin-film response. Similar to the NaNbO₃, NaTaO₃ [100]-oriented and NaTaO-terminated thin-film formation inserted surface states inside the band gap. In contrast, these surface states were closer to the band gap's middle point, localizing and filling them. The surface states' energy levels being closer to the band gap's middle point allowed for water-splitting partial reactions leverage with biaxial strain: under compression, the surface states would leverage hydrogen evolution reactions against oxygen evolution, while tension made surface states' energy levels compatible with the oxygen evolution reaction. Bulk vacancy's effects on perovskites' band structure stimulate the extension of thin-film studies to describe their effect on surface states. Vacancies' energy levels could shift surface formation mechanisms in such a way that surface energy levels could become more like the ones on NaTaO₃.

REFERENCES

- 1 FUJISHIMA, Akira; HONDA, Kenichi. Electrochemical Photolysis of Water at a Semiconductor Electrode. **Nature**, v. 238, n. 5358, p. 37–38, July 1972. ISSN 0028-0836, 1476-4687. DOI: 10.1038/238037a0.
- 2 OSTERLOH, Frank E. Inorganic Materials as Catalysts for Photochemical Splitting of Water. **Chemistry of Materials**, v. 20, n. 1, p. 35–54, Jan. 2008. ISSN 0897-4756, 1520-5002. DOI: 10.1021/cm7024203.
- 3 LI, Le; WANG, Minqiang. Advanced Nanomaterials for Solar Photocatalysis. In: NORENA, Luis Enrique; WANG, Jin-An (Eds.). **Advanced Catalytic Materials - Photocatalysis and Other Current Trends**. [S.l.]: InTech, 3 Feb. 2016. ISBN 978-953-51-2244-9. DOI: 10.5772/62206.
- 4 WALTER, Michael G. et al. Solar Water Splitting Cells. **Chemical Reviews**, v. 110, n. 11, p. 6446–6473, 10 Nov. 2010. ISSN 0009-2665, 1520-6890. DOI: 10.1021/cr1002326.
- 5 MILLS, Andrew; LE HUNTE, Stephen. An overview of semiconductor photocatalysis. **Journal of Photochemistry and Photobiology A: Chemistry**, v. 108, n. 1, p. 1–35, July 1997. ISSN 10106030. DOI: 10.1016/S1010-6030(97)00118-4.
- 6 LI, Yan et al. An electrochemically neutralized energy-assisted low-cost acid-alkaline electrolyzer for energy-saving electrolysis hydrogen generation. **Journal of Materials Chemistry A**, v. 6, n. 12, p. 4948–4954, 2018. ISSN 2050-7488, 2050-7496. DOI: 10.1039/C7TA10374C.
- 7 TURNER, J. A. A Realizable Renewable Energy Future. **Science**, v. 285, n. 5428, p. 687–689, 30 July 1999. ISSN 00368075, 10959203. DOI: 10.1126/science.285.5428.687.
- 8 NALDONI, Alberto et al. Photocatalysis with Reduced TiO_2 : From Black TiO_2 to Cocatalyst-Free Hydrogen Production. **ACS Catalysis**, v. 9, n. 1, p. 345–364, 4 Jan. 2019. ISSN 2155-5435, 2155-5435. DOI: 10.1021/acscatal.8b04068.

- 9 PHOON, Bao Lee et al. Recent developments of strontium titanate for photocatalytic water splitting application. **International Journal of Hydrogen Energy**, v. 44, n. 28, p. 14316–14340, May 2019. ISSN 03603199. DOI: 10.1016/j.ijhydene.2019.01.166.
- 10 KATO, Hideki; KUDO, Akihiko. Water Splitting into H₂ and O₂ on Alkali Tantalate Photocatalysts ATaO₃ (A = Li, Na, and K). **The Journal of Physical Chemistry B**, v. 105, n. 19, p. 4285–4292, May 2001. ISSN 1520-6106, 1520-5207. DOI: 10.1021/jp004386b.
- 11 LIN, Wan-Hsien et al. NaTaO₃ photocatalysts of different crystalline structures for water splitting into H₂ and O₂. **Applied Physics Letters**, v. 89, n. 21, p. 211904, 20 Nov. 2006. ISSN 0003-6951, 1077-3118. DOI: 10.1063/1.2396930.
- 12 SAITO, Kenji; KUDO, Akihiko. Niobium-Complex-Based Syntheses of Sodium Niobate Nanowires Possessing Superior Photocatalytic Properties. **Inorganic Chemistry**, v. 49, n. 5, p. 2017–2019, Mar. 2010. ISSN 0020-1669, 1520-510X. DOI: 10.1021/ic902107u.
- 13 RINGGAARD, Erling; WURLITZER, Thom. Lead-free piezoceramics based on alkali niobates. **Journal of the European Ceramic Society**, v. 25, n. 12, p. 2701–2706, Jan. 2005. ISSN 09552219. DOI: 10.1016/j.jeurceramsoc.2005.03.126.
- 14 WANG, Guangjin et al. A first-principle study of oxygen reduction reaction on monoclinic zirconia (-111), (-101) and (110) surfaces. **Catalysis Communications**, v. 69, p. 16–19, Sept. 2015. ISSN 15667367. DOI: 10.1016/j.catcom.2015.04.036.
- 15 ZHANG, Guan et al. Inorganic perovskite photocatalysts for solar energy utilization. **Chemical Society Reviews**, v. 45, n. 21, p. 5951–5984, 2016. ISSN 0306-0012, 1460-4744. DOI: 10.1039/C5CS00769K.
- 16 KANHERE, Pushkar; CHEN, Zhong. A Review on Visible Light Active Perovskite-Based Photocatalysts. **Molecules**, v. 19, n. 12, p. 19995–20022, 1 Dec. 2014. ISSN 1420-3049. DOI: 10.3390/molecules191219995.
- 17 GUERRERO, Antonio; BISQUERT, Juan. Perovskite semiconductors for photoelectrochemical water splitting applications. **Current Opinion in**

- Electrochemistry**, v. 2, n. 1, p. 144–147, Apr. 2017. ISSN 24519103. DOI: 10.1016/j.coelec.2017.04.003.
- 18 LL, Peng et al. The Effects of Crystal Structure and Electronic Structure on Photocatalytic H₂ Evolution and CO₂ Reduction over Two Phases of Perovskite-Structured NaNbO₃. **The Journal of Physical Chemistry C**, v. 116, n. 14, p. 7621–7628, 12 Apr. 2012. ISSN 1932-7447, 1932-7455. DOI: 10.1021/jp210106b.
- 19 SU, Yiguo et al. Tantalate-based Perovskite for Solar Energy Applications. In: PAN, Likun; ZHU, Guang (Eds.). **Perovskite Materials - Synthesis, Characterisation, Properties, and Applications**. [S.l.]: InTech, 3 Feb. 2016. ISBN 978-953-51-2245-6. DOI: 10.5772/61390.
- 20 PORTUGAL, Guilherme Ribeiro; SANTOS, Sydney Ferreira; ARANTES, Jeverson Teodoro. NaTaO₃ cubic and orthorhombic surfaces: An intrinsic improvement of photocatalytic properties. **Applied Surface Science**, v. 502, p. 144206, Feb. 2020. ISSN 01694332. DOI: 10.1016/j.apsusc.2019.144206.
- 21 ZHAO, Xunhua; SELLONI, Annabella. Structure and stability of NaTaO₃ (001) and KTaO₃ (001) surfaces. **Physical Review Materials**, v. 3, n. 1, p. 015801, 2 Jan. 2019. ISSN 2475-9953. DOI: 10.1103/PhysRevMaterials.3.015801.
- 22 PORTUGAL, Guilherme Ribeiro; ARANTES, Jeverson Teodoro. Strain modulation of TaO₄ planarity in tantalates ultrathin films: surface states engineering. **Scientific Reports**, v. 10, n. 1, p. 7828, Dec. 2020. ISSN 2045-2322. DOI: 10.1038/s41598-020-64315-7.
- 23 KRAUS, Alexandre Olivieri; PORTUGAL, Guilherme Ribeiro; ARANTES, Jeverson Teodoro. Modulation of band alignment with water redox potentials by biaxial strain on orthorhombic NaTaO₃ thin films. **Physical Chemistry Chemical Physics**, v. 22, n. 41, p. 23810–23815, 2020. ISSN 1463-9076, 1463-9084. DOI: 10.1039/D0CP04322B.
- 24 ZIELIŃSKA, Beata; KALEŃCZUK, Ryszard. Comparison of NaNbO₃ and NaTaO₃ as the photocatalysts in the reaction of hydrogen generation. **Polish**

- Journal of Chemical Technology**, v. 12, n. 3, p. 33–35, 1 Jan. 2010. ISSN 1899-4741, 1509-8117. DOI: 10.2478/v10026-010-0030-1.
- 25 YANG, Bian et al. Enhanced photocatalytic activity of perovskite NaNbO_3 by oxygen vacancy engineering. **Physical Chemistry Chemical Physics**, v. 21, n. 22, p. 11697–11704, 2019. ISSN 1463-9076, 1463-9084. DOI: 10.1039/C9CP01763A.
- 26 QUEISSER, H. J. Defects in Semiconductors: Some Fatal, Some Vital. **Science**, v. 281, n. 5379, p. 945–950, 14 Aug. 1998. DOI: 10.1126/science.281.5379.945.
- 27 MORRIS HOTSENPILLER, P. A. et al. Orientation Dependence of Photochemical Reactions on TiO_2 Surfaces. **The Journal of Physical Chemistry B**, v. 102, n. 17, p. 3216–3226, Apr. 1998. ISSN 1520-6106, 1520-5207. DOI: 10.1021/jp980104k.
- 28 IBACH, Harald. Structure of Surfaces. In: **PHYSICS of Surfaces and Interfaces**. 1. ed. New York: Springer, 2006. v. 1. P. 1–58. ISBN 978-3-540-34709-5.
- 29 NOGUERA, Claudine. Polar oxide surfaces. **Journal of Physics: Condensed Matter**, v. 12, n. 31, r367–r410, 7 Aug. 2000. ISSN 0953-8984, 1361-648X. DOI: 10.1088/0953-8984/12/31/201.
- 30 KRESSE, G.; FURTHMÜLLER, J. Efficient iterative schemes for *ab initio* total-energy calculations using a plane-wave basis set. **Physical Review B**, v. 54, n. 16, p. 11169–11186, 15 Oct. 1996. ISSN 0163-1829, 1095-3795. DOI: 10.1103/PhysRevB.54.11169.
- 31 KRESSE, G.; JOUBERT, D. From ultrasoft pseudopotentials to the projector augmented-wave method. **Physical Review B**, v. 59, n. 3, p. 1758–1775, 15 Jan. 1999. ISSN 0163-1829, 1095-3795. DOI: 10.1103/PhysRevB.59.1758.
- 32 MARTIN, Richard M. **Electronic Structure: Basic Theory and Practical Methods**. 2. ed. New York: Cambridge University Press, Oct. 2020. v. 1. ISBN 978-1-108-42990-0. DOI: 10.1017/CB09780511805769.
- 33 CAPELLE, Klaus. A bird’s-eye view of density-functional theory. **arXiv:cond-mat/0211443**, 18 Nov. 2006. arXiv: cond-mat/0211443.
- 34 KOHN, W.; SHAM, L. J. Self-Consistent Equations Including Exchange and Correlation Effects. **Physical Review**, v. 140, n. 4, a1133–a1138, 15 Nov. 1965. ISSN 0031-899X. DOI: 10.1103/PhysRev.140.A1133.

- 35 HOHENBERG, P.; KOHN, W. Inhomogeneous Electron Gas. **Physical Review**, v. 136, n. 3, b864–b871, 9 Nov. 1964. ISSN 0031-899X. DOI: 10.1103/PhysRev.136.B864.
- 36 FEYNMAN, R. P. Forces in Molecules. **Physical Review**, v. 56, n. 4, p. 340–343, 15 Aug. 1939. ISSN 0031-899X. DOI: 10.1103/PhysRev.56.340.
- 37 GEORGE, R. T. et al. Effect of NiO substitution on the structural and dielectric behaviour of NaNbO_3 . **Journal of Applied Physics**, v. 123, n. 5, p. 054101, 7 Feb. 2018. ISSN 0021-8979, 1089-7550. DOI: 10.1063/1.5013643.
- 38 PERDEW, John P.; BURKE, Kieron; ERNZERHOF, Matthias. Generalized Gradient Approximation Made Simple. **Physical Review Letters**, v. 77, n. 18, p. 3865–3868, 28 Oct. 1996. ISSN 0031-9007, 1079-7114. DOI: 10.1103/PhysRevLett.77.3865.
- 39 STOLIAROFF, Adrien; LATOUCHE, Camille. Accurate Ab Initio Calculations on Various PV-Based Materials: Which Functional to Be Used? **The Journal of Physical Chemistry C**, v. 124, n. 16, p. 8467–8478, 23 Apr. 2020. ISSN 1932-7447, 1932-7455. DOI: 10.1021/acs.jpcc.9b10821.
- 40 YU, Maituo et al. Machine learning the Hubbard U parameter in DFT+ U using Bayesian optimization. **npj Computational Materials**, v. 6, n. 1, p. 1–6, 27 Nov. 2020. ISSN 2057-3960. DOI: 10.1038/s41524-020-00446-9.
- 41 BLÖCHL, P. E. Projector augmented-wave method. **Physical Review B**, v. 50, n. 24, p. 17953–17979, 15 Dec. 1994. ISSN 0163-1829, 1095-3795. DOI: 10.1103/PhysRevB.50.17953.
- 42 MONKHORST, Hendrik J.; PACK, James D. Special points for Brillouin-zone integrations. **Physical Review B**, v. 13, n. 12, p. 5188–5192, 15 June 1976. ISSN 0556-2805. DOI: 10.1103/PhysRevB.13.5188.
- 43 SHIM, Jihye et al. Density-functional calculations of defect formation energies using the supercell method: Brillouin-zone sampling. **Physical Review B**, v. 71, n. 24, p. 245204, 27 June 2005. ISSN 1098-0121, 1550-235X. DOI: 10.1103/PhysRevB.71.245204.
- 44 PUSKA, M. J. et al. Convergence of supercell calculations for point defects in semiconductors: Vacancy in silicon. **Physical Review B**, v. 58, n. 3, p. 1318–1325, 15 July 1998. ISSN 0163-1829, 1095-3795. DOI: 10.1103/PhysRevB.58.1318.

- 45 CASTLETON, C. W. M.; MIRBT, S. Finite-size scaling as a cure for supercell approximation errors in calculations of neutral native defects in InP. **Physical Review B**, v. 70, n. 19, p. 195202, 8 Nov. 2004. ISSN 1098-0121, 1550-235X. DOI: 10.1103/PhysRevB.70.195202.
- 46 BADER, R.F.W.; NGUYEN-DANG, T.T. Quantum Theory of Atoms in Molecules–Dalton Revisited. In: **ADVANCES in Quantum Chemistry**. [S.l.]: Elsevier, 1981. v. 14. P. 63–124. ISBN 978-0-12-034814-5. DOI: 10.1016/S0065-3276(08)60326-3.
- 47 TANG, W; SANVILLE, E; HENKELMAN, G. A grid-based Bader analysis algorithm without lattice bias. **Journal of Physics: Condensed Matter**, v. 21, n. 8, p. 084204, 25 Feb. 2009. ISSN 0953-8984, 1361-648X. DOI: 10.1088/0953-8984/21/8/084204.
- 48 SANVILLE, Edward et al. Improved grid-based algorithm for Bader charge allocation. **Journal of Computational Chemistry**, v. 28, n. 5, p. 899–908, 15 Apr. 2007. ISSN 01928651, 1096987X. DOI: 10.1002/jcc.20575.
- 49 HENKELMAN, Graeme; ARNALDSSON, Andri; JÓNSSON, Hannes. A fast and robust algorithm for Bader decomposition of charge density. **Computational Materials Science**, v. 36, n. 3, p. 354–360, June 2006. ISSN 09270256. DOI: 10.1016/j.commatsci.2005.04.010.
- 50 YU, Min; TRINKLE, Dallas R. Accurate and efficient algorithm for Bader charge integration. **The Journal of Chemical Physics**, v. 134, n. 6, p. 064111, 14 Feb. 2011. ISSN 0021-9606, 1089-7690. DOI: 10.1063/1.3553716.
- 51 RONDINELLI, James M.; SPALDIN, Nicola A. Structure and Properties of Functional Oxide Thin Films: Insights From Electronic-Structure Calculations. **Advanced Materials**, v. 23, n. 30, p. 3363–3381, 9 Aug. 2011. ISSN 09359648. DOI: 10.1002/adma.201101152.
- 52 CAMMARATA, Antonio; RONDINELLI, James M. Covalent dependence of octahedral rotations in orthorhombic perovskite oxides. **The Journal of Chemical Physics**, v. 141, n. 11, p. 114704, 21 Sept. 2014. ISSN 0021-9606, 1089-7690. DOI: 10.1063/1.4895967.

- 53 BAUR, W. H. The geometry of polyhedral distortions. Predictive relationships for the phosphate group. **Acta Crystallographica Section B Structural Crystallography and Crystal Chemistry**, v. 30, n. 5, p. 1195–1215, 1 May 1974. ISSN 0567-7408. DOI: 10.1107/S0567740874004560.
- 54 KRÖGER, F.A.; VINK, H.J. Relations between the Concentrations of Imperfections in Crystalline Solids. In: **SOLID State Physics**. [S.l.]: Elsevier, 1956. v. 3. P. 307–435. ISBN 978-0-12-607703-2. DOI: 10.1016/S0081-1947(08)60135-6.
- 55 SHIGEMI, Akio; WADA, Takahiro. Enthalpy of Formation of Various Phases and Formation Energy of Point Defects in Perovskite-Type NaNbO_3 by First-Principles Calculation. **Japanese Journal of Applied Physics**, v. 43, n. 9, p. 6793–6798, 22 Sept. 2004. ISSN 0021-4922, 1347-4065. DOI: 10.1143/JJAP.43.6793.
- 56 EGLITIS, R. I. *Ab initio* calculations of SrTiO_3 , BaTiO_3 , PbTiO_3 , CaTiO_3 , SrZrO_3 , PbZrO_3 and BaZrO_3 (001), (011) and (111) surfaces as well as F centers, polarons, KTN solid solutions and Nb impurities therein. **International Journal of Modern Physics B**, v. 28, n. 17, p. 1430009, 10 July 2014. ISSN 0217-9792, 1793-6578. DOI: 10.1142/S0217979214300096.
- 57 ZHANG, S B. The microscopic origin of the doping limits in semiconductors and wide-gap materials and recent developments in overcoming these limits: a review. **Journal of Physics: Condensed Matter**, v. 14, n. 34, r881–r903, 2 Sept. 2002. ISSN 0953-8984. DOI: 10.1088/0953-8984/14/34/201.
- 58 SHIGEMI, Akio; WADA, Takahiro. Evaluations of Phases and Vacancy Formation Energies in KNbO_3 by First-Principles Calculation. **Japanese Journal of Applied Physics**, v. 44, n. 11, p. 8048–8054, 9 Nov. 2005. ISSN 0021-4922, 1347-4065. DOI: 10.1143/JJAP.44.8048.
- 59 BECHER, Carsten et al. Strain-induced coupling of electrical polarization and structural defects in SrMnO_3 films. **Nature Nanotechnology**, v. 10, n. 8, p. 661–665, Aug. 2015. ISSN 1748-3387, 1748-3395. DOI: 10.1038/nnano.2015.108.
- 60 KITTEL, Charles. In: **INTRODUCTION to Solid State Physics**. 8th ed. New York: Wiley, 2005. v. 1 chap. 6, p. 131–160. ISBN 9780471415268.

- 61 SHEGELSKI, Mark R.A. New result for the chemical potential of intrinsic semiconductors: Low-temperature breakdown of the Fermi-Dirac distribution function. **Solid State Communications**, v. 58, n. 6, p. 351–354, May 1986. ISSN 00381098. DOI: 10.1016/0038-1098(86)90803-3.
- 62 CASTLETON, C. W. M.; HOGLUND, A.; MIRBT, S. Managing the supercell approximation for charged defects in semiconductors: finite size scaling, charge correction factors, the bandgap problem and the ab initio dielectric constant. **Physical Review B**, v. 73, n. 3, p. 035215, 25 Jan. 2006. ISSN 1098-0121, 1550-235X. DOI: 10.1103/PhysRevB.73.035215. arXiv: cond-mat/0512311.
- 63 VAN DE WALLE, Chris G.; NEUGEBAUER, Jörg. First-principles calculations for defects and impurities: Applications to III-nitrides. **Journal of Applied Physics**, v. 95, n. 8, p. 3851–3879, 15 Apr. 2004. ISSN 0021-8979, 1089-7550. DOI: 10.1063/1.1682673.
- 64 LANY, Stephan; ZUNGER, Alex. Assessment of correction methods for the band-gap problem and for finite-size effects in supercell defect calculations: Case studies for ZnO and GaAs. **Physical Review B**, v. 78, n. 23, p. 235104, 4 Dec. 2008. ISSN 1098-0121, 1550-235X. DOI: 10.1103/PhysRevB.78.235104.
- 65 REIN, S. et al. Lifetime spectroscopy for defect characterization: Systematic analysis of the possibilities and restrictions. **Journal of Applied Physics**, v. 91, n. 4, p. 2059–2070, 2002. DOI: 10.1063/1.1428095.
- 66 FREYSOLDT, Christoph et al. First-principles calculations for point defects in solids. **Reviews of Modern Physics**, v. 86, n. 1, p. 253–305, 28 Mar. 2014. ISSN 0034-6861, 1539-0756. DOI: 10.1103/RevModPhys.86.253.
- 67 SAAL, James E. et al. Materials Design and Discovery with High-Throughput Density Functional Theory: The Open Quantum Materials Database (OQMD). **JOM**, v. 65, n. 11, p. 1501–1509, Nov. 2013. ISSN 1047-4838, 1543-1851. DOI: 10.1007/s11837-013-0755-4.
- 68 KIRKLIN, Scott et al. The Open Quantum Materials Database (OQMD): assessing the accuracy of DFT formation energies. **npj Computational Materials**, v. 1, n. 1, p. 15010, Dec. 2015. ISSN 2057-3960. DOI: 10.1038/npjcompumats.2015.10.

- 69 BARRETT, C. S. X-ray study of the alkali metals at low temperatures. **Acta Crystallographica**, v. 9, n. 8, p. 671–677, 1 Aug. 1956. ISSN 0365-110X. DOI: 10.1107/S0365110X56001790.
- 70 ZINTL, E; HARDER, A; DAUTH, B. Gitterstruktur der Oxyde, Sulfide, Selenide und Telluride des Lithiums, Natriums und Kaliums. **Zeitschrift für Elektrochemie und angewandte physikalische Chemie**, v. 40, n. 8, p. 588–593, 1934. DOI: 10.1002/bbpc.19340400811.
- 71 FOPPL, Hermann. Die Kristallstrukturen der Alkaliperoxyde. **Zeitschrift für anorganische und allgemeine Chemie**, v. 291, n. 1, p. 12–50, Sept. 1957. ISSN 0044-2313, 1521-3749. DOI: 10.1002/zaac.19572910104.
- 72 ZHURAVLEV, Yu. N.; OBOLONSKAYA, O. S. Structure, mechanical stability, and chemical bond in alkali metal oxides. **Journal of Structural Chemistry**, v. 51, n. 6, p. 1005–1013, Dec. 2010. ISSN 0022-4766, 1573-8779. DOI: 10.1007/s10947-010-0157-1.
- 73 BOLLINGER, R. K. et al. Observation of a Martensitic Structural Distortion in V, Nb, and Ta. **Physical Review Letters**, v. 107, n. 7, p. 075503, 10 Aug. 2011. ISSN 0031-9007, 1079-7114. DOI: 10.1103/PhysRevLett.107.075503.
- 74 BOWMAN, A. L. et al. The crystal structure of niobium monoxide. **Acta Crystallographica**, v. 21, n. 5, p. 843–843, 1 Nov. 1966. ISSN 0365-110X. DOI: 10.1107/S0365110X66004043.
- 75 SCHMIDT, Rainer et al. Bi containing multiferroic perovskite oxide thin films. In: **PEROVSKITE: crystallography, chemistry and catalytic performance**. New York: Nova Science Publishers, 2013. P. 39. ISBN 978-1-62417-800-9.
- 76 KLEIN, Wilhelm; ARMBRUSTER, Klaus; JANSEN, Martin. Synthesis and crystal structure determination of sodium ozonide. **Chemical Communications**, n. 6, p. 707–708, 1998. ISSN 13597345, 1364548X. DOI: 10.1039/a708570b.
- 77 FREYSOLDT, Christoph; NEUGEBAUER, Jörg; VAN DE WALLE, Chris G. Fully *Ab Initio* Finite-Size Corrections for Charged-Defect Supercell Calculations. **Physical Review Letters**, v. 102, n. 1, p. 016402, 5 Jan. 2009. ISSN 0031-9007, 1079-7114. DOI: 10.1103/PhysRevLett.102.016402.

- 78 BARONI, Stefano; RESTA, Raffaele. *Ab initio* calculation of the macroscopic dielectric constant in silicon. **Physical Review B**, v. 33, n. 10, p. 7017–7021, 15 May 1986. ISSN 0163-1829. DOI: 10.1103/PhysRevB.33.7017.
- 79 GAJDOŠ, M. et al. Linear optical properties in the projector-augmented wave methodology. **Physical Review B**, v. 73, n. 4, p. 045112, 17 Jan. 2006. ISSN 1098-0121, 1550-235X. DOI: 10.1103/PhysRevB.73.045112.
- 80 ASCHAUER, Ulrich et al. Strain controlled oxygen vacancy formation and ordering in CaMnO_3 . **arXiv:1303.4749 [cond-mat]**, 19 Mar. 2013. DOI: 10.1103/PhysRevB.88.054111. arXiv: 1303.4749.
- 81 SUN, Wenhao; CEDER, Gerbrand. Efficient creation and convergence of surface slabs. **Surface Science**, v. 617, p. 53–59, Nov. 2013. ISSN 00396028. DOI: 10.1016/j.susc.2013.05.016.
- 82 TYUNINA, M.; LEVOSKA, J. Unstable state in epitaxial films of sodium niobate. **Applied Physics Letters**, v. 95, n. 10, p. 102903, 7 Sept. 2009. ISSN 0003-6951, 1077-3118. DOI: 10.1063/1.3222900.
- 83 BAEISSA, E.S. Photocatalytic degradation of malachite green dye using Au/NaNbO_3 nanoparticles. **Journal of Alloys and Compounds**, v. 672, p. 564–570, July 2016. ISSN 09258388. DOI: 10.1016/j.jallcom.2016.02.024.
- 84 ZHANG, Xue-Jing; LIU, Bang-Gui. Strain-driven sign interchange of surface two-dimensional electron and hole gases in KTaO_3 thin film. **Physical Chemistry Chemical Physics**, v. 20, n. 37, p. 24257–24262, 2018. ISSN 1463-9076, 1463-9084. DOI: 10.1039/C8CP03650K. arXiv: 1804.07147.
- 85 XU, Zhiping; BUEHLER, Markus J. Interface structure and mechanics between graphene and metal substrates: a first-principles study. **Journal of Physics: Condensed Matter**, v. 22, n. 48, p. 485301, 8 Dec. 2010. ISSN 0953-8984, 1361-648X. DOI: 10.1088/0953-8984/22/48/485301.
- 86 PETRIE, Jonathan R. et al. Strain Control of Oxygen Vacancies in Epitaxial Strontium Cobaltite Films. **Advanced Functional Materials**, v. 26, n. 10, p. 1564–1570, Mar. 2016. ISSN 1616301X. DOI: 10.1002/adfm.201504868.

- 87 LI, Peng et al. Constructing cubic–orthorhombic surface-phase junctions of NaNbO_3 towards significant enhancement of CO_2 photoreduction. **J. Mater. Chem. A**, v. 2, n. 16, p. 5606–5609, 2014. ISSN 2050-7488, 2050-7496. DOI: 10.1039/C4TA00105B.
- 88 BAGAYOKO, Diola. Understanding density functional theory (DFT) and completing it in practice. **AIP Advances**, v. 4, n. 12, p. 127104, Dec. 2014. ISSN 2158-3226. DOI: 10.1063/1.4903408.
- 89 JEAN, Yves. Principal Ligand Fields: σ interactions. In: MOLECULAR orbitals of transition metal complexes. New York: OUP Oxford, 2005. P. 37–96. ISBN 0-19-853093-5.
- 90 _____. π -type interactions. In: MOLECULAR orbitals of transition metal complexes. New York: OUP Oxford, 2005. P. 97–140. ISBN 0-19-853093-5.
- 91 FANG, Wen Qi et al. Manipulating solar absorption and electron transport properties of rutile TiO_2 photocatalysts via highly n-type F-doping. **Journal of Materials Chemistry A**, v. 2, n. 10, p. 3513, 2014. ISSN 2050-7488, 2050-7496. DOI: 10.1039/c3ta13917d.
- 92 CZOSKA, A. M. et al. The nature of defects in fluorine-doped TiO_2 . **The Journal of Physical Chemistry C**, v. 112, n. 24, p. 8951–8956, 2008. DOI: 10.1021/jp8004184.
- 93 ACKER, Jérôme et al. Microstructure of sodium-potassium niobate ceramics sintered under high alkaline vapor pressure atmosphere. **Journal of the European Ceramic Society**, v. 34, n. 16, p. 4213–4221, Dec. 2014. ISSN 09552219. DOI: 10.1016/j.jeurceramsoc.2014.06.021.
- 94 SHIGEMI, Akio; WADA, Takahiro. First-principles Studies of Phase Stability and the Neutral Atomic Vacancies in LiNbO_3 , NaNbO_3 and KNbO_3 . **MRS Proceedings**, v. 902, 0902–t10–46, 2005. ISSN 0272-9172, 1946-4274. DOI: 10.1557/PROC-0902-T10-46.
- 95 XI, Jianqi et al. Strain effects on oxygen vacancy energetics in KTaO_3 . **Physical Chemistry Chemical Physics**, v. 19, n. 8, p. 6264–6273, 2017. ISSN 1463-9076, 1463-9084. DOI: 10.1039/C6CP08315C.

- 96 JANOTTI, A. et al. Hybrid functional studies of the oxygen vacancy in TiO_2 . **Phys. Rev. B**, American Physical Society, v. 81, p. 085212, 8 Feb. 2010. DOI: 10.1103/PhysRevB.81.085212.
- 97 OBA, Fumiyasu et al. Point defects in ZnO : an approach from first principles. **Science and Technology of Advanced Materials**, v. 12, n. 3, p. 034302, June 2011. ISSN 1468-6996, 1878-5514. DOI: 10.1088/1468-6996/12/3/034302.
- 98 MARTIN, Richard M. Functionals for Exchange and Correlation II. In: **ELECTRONIC Structure: Basic Theory and Practical Methods**. 2. ed. New York: Cambridge University Press, Oct. 2020. v. 1 chap. 9, p. 188–213. ISBN 978-1-108-42990-0. DOI: 10.1017/CB09780511805769.
- 99 YANG, Ji-Hui et al. Self-regulation of charged defect compensation and formation energy pinning in semiconductors. **Scientific Reports**, v. 5, n. 1, p. 16977, Dec. 2015. ISSN 2045-2322. DOI: 10.1038/srep16977.
- 100 PAN, Lun et al. Manipulating spin polarization of titanium dioxide for efficient photocatalysis. **Nature Communications**, v. 11, n. 1, p. 418, Dec. 2020. ISSN 2041-1723. DOI: 10.1038/s41467-020-14333-w.
- 101 HAMEEUW, K. J. et al. The rutile TiO_2 (110) surface: Obtaining converged structural properties from first-principles calculations. **The Journal of Chemical Physics**, v. 124, n. 2, p. 024708, 14 Jan. 2006. ISSN 0021-9606, 1089-7690. DOI: 10.1063/1.2136158.
- 102 BOEYENS, Jan C. A. The Periodic Electronegativity Table. **Zeitschrift für Naturforschung B**, v. 63, n. 2, p. 199–209, 1 Feb. 2008. ISSN 1865-7117. DOI: 10.1515/znb-2008-0214.
- 103 HU, Che-Chia; TENG, Hsisheng. Influence of structural features on the photocatalytic activity of NaTaO_3 powders from different synthesis methods. **Applied Catalysis A: General**, v. 331, p. 44–50, Jan. 2007. ISSN 0926860X. DOI: 10.1016/j.apcata.2007.07.024.
- 104 KENNEDY, Brendan J; PRODJOSANTOSO, A K; HOWARD, Christopher J. Powder neutron diffraction study of the high temperature phase transitions in NaTaO_3 . **Journal of Physics: Condensed Matter**, v. 11, n. 33, p. 6319–6327, 23 Aug. 1999. ISSN 0953-8984, 1361-648X. DOI: 10.1088/0953-8984/11/33/302.

-
- 105 RUMBLE, John R; LIDE, David R; BRUNO, Thomas J. **CRC handbook of chemistry and physics**. 97. ed. Boca Raton: CRC Press, 2017. v. 1. 2643 pp. ISBN 978-1-4987-5429-3.
- 106 KOBERTZ, Dietmar; MÜLLER, Michael; MOLAK, Andrzej. Vaporization and caloric studies on sodium niobate. **Calphad**, v. 48, p. 55–71, Mar. 2015. ISSN 03645916. DOI: 10.1016/j.calphad.2014.10.007.

Appendix

APPENDIX A – SUPPORTING INFORMATION

Table 5 – The geometrical properties of the relaxed, strain-free bulk orthorhombic (Pmna) NaNbO₃. Values used in the comparisons at Tab. 3.

$\langle d \rangle$	Δ_d	α [010]	β [10 $\bar{1}$]	γ [101]
2.014 Å	0.03 %	163°	164°	164°

Table 6 – Comparison between calculated and experimental formation enthalpies.

	ΔE_f (eV/ un.)									
	Na	Na ₂ O	Na ₂ O ₂	NaO ₂	Nb	NbO	NbO ₂	Nb ₂ O ₅	$\frac{1}{2}$ O ₂	o-NaNbO ₃
Calculated	−1.3	−3.7	−4.3	−2.3	−10.1	−3.9	−7.4	−17.9	−9.8	−12.1
Experimental	—	−4.3*	−5.3*	−2.7*	—	−4.2*	−8.0*	−19.7*	—	−13.0 [†]
Divergence	—	−14%	−18%	−16%	—	−7%	−8%	−9%	—	−6%

* ref. [105].[†] ref. [106].

Table 7 – Charged vacancy formation effects on first neighbors' geometry compared to unrelaxed (pristine) structure.

	v_O^{2+}			v_{Na}^{1-}		
	Unrelaxed	Relaxed	Change	Unrelaxed	Relaxed	Change
d(v-Na) (Å)	2.810	2.881	+3%	3.951	2.961	+0.2%
d(v-Nb) (Å)	2.013	2.268	+13%	3.421	3.387	−1%
d(v-O) (Å)	2.847	2.702	−5%	2.803	2.852	+2%
α [010] (°)	163	165	+1%	163	167	+2%
β [10 $\bar{1}$] (°)	164	152	−7%	164	165	+0.4%
γ [101] (°)	164	176	+7%	164	164	0%

Table 8 – Differences between defected and pristine supercell’s total energies for each supercell size. Band dispersion corrections were added to the total energy differences.

	v_{Na}^0	v_{Na}^{1-}	v_{O}^0	v_{O}^{2+}
$1 \times 1 \times 1$	5.36	6.48	10.12	2.85
$2 \times 2 \times 2$	5.58	6.88	8.36	2.07
$3 \times 3 \times 3$	5.97	7.29	8.76	2.35

Figure 26 – Pristine bulk's (black), defected supercell's (red) crystal potentials, and the difference (blue) between them in $2 \times 2 \times 2$ supercells. Potential correction depends on the pristine bulk's potential recovery far from the defect center (vertical dashed lines). Potentials calculated from plane-average with [100], [010] and [001] crystallographic directions normal to each one of them.

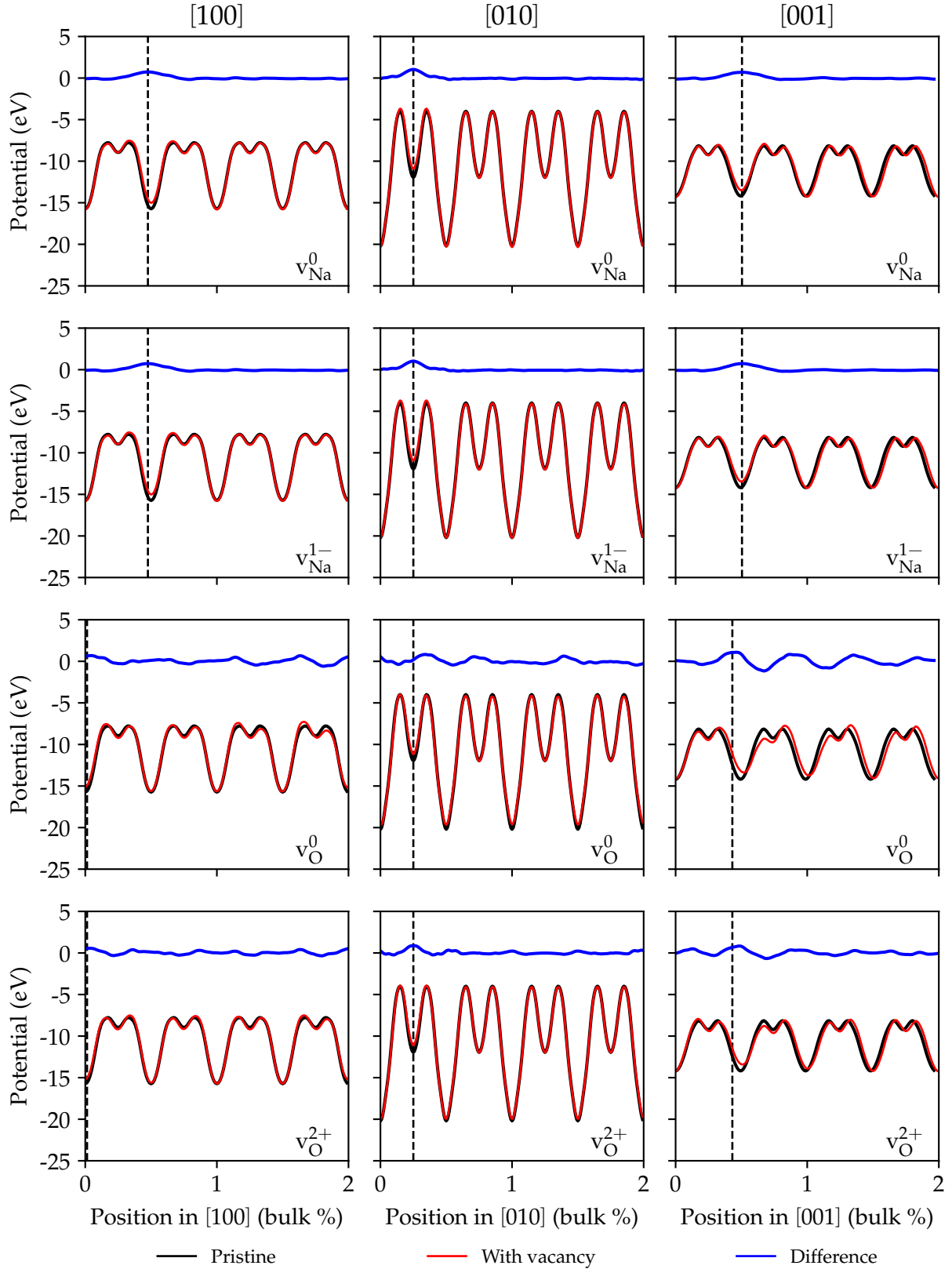


Figure 27 – Pristine bulk's (black), defected supercell's (red) crystal potentials, and the difference (blue) between them in $3 \times 3 \times 3$ supercells. Potential correction depends on the pristine bulk's potential recovery far from the defect center (vertical dashed lines). Potentials calculated from plane-average with [100], [010] and [001] crystallographic directions normal to each one of them.

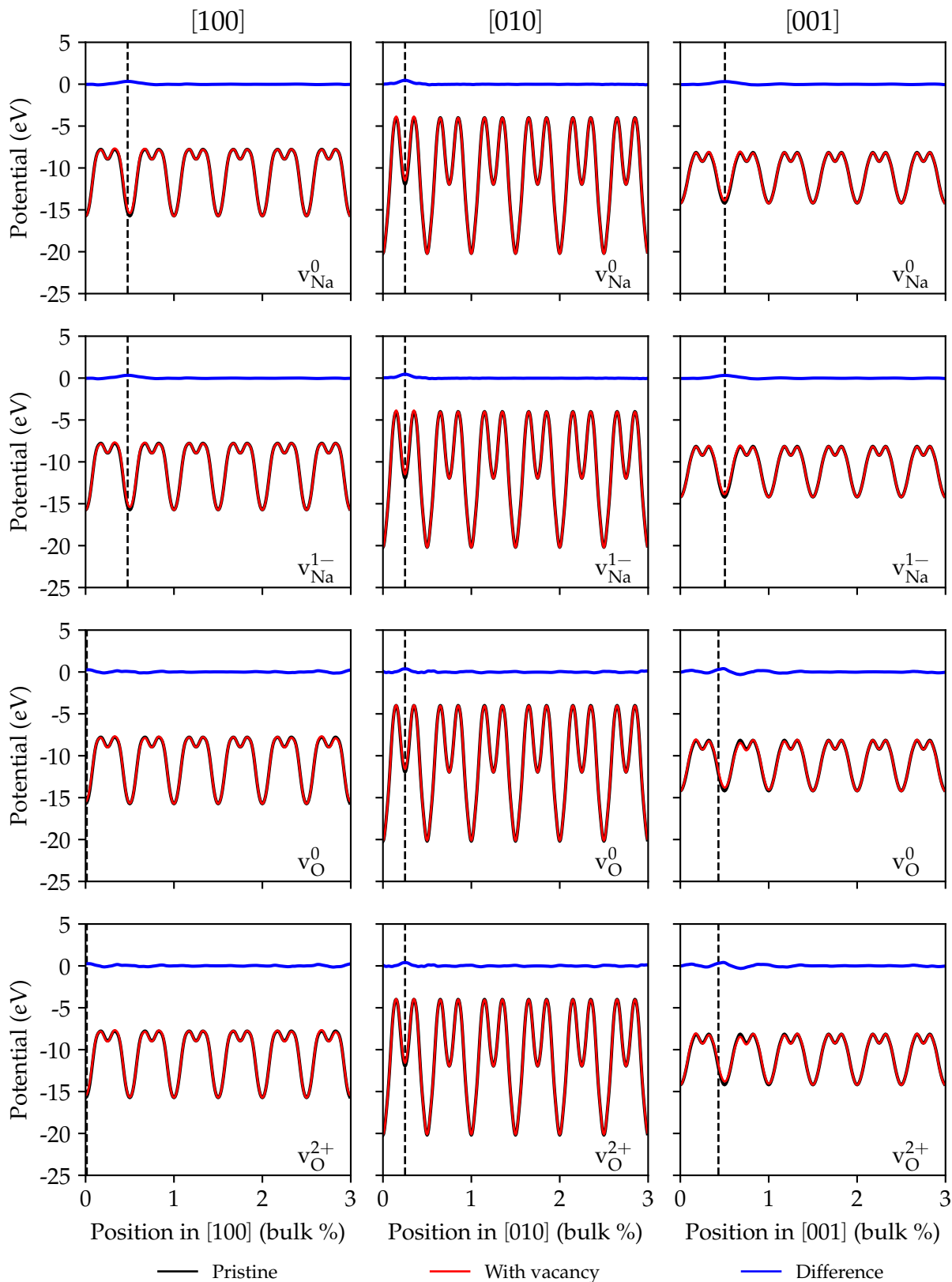


Figure 28 – Pristine bulk's (black), defected supercell's (red) crystal potentials, and the difference (blue) between them in $1 \times 1 \times 1$ supercells. Potential correction depends on the pristine bulk's potential recovery far from the defect center (vertical dashed lines). Potentials calculated from plane-average with [100], [010] and [001] crystallographic directions normal to each one of them.

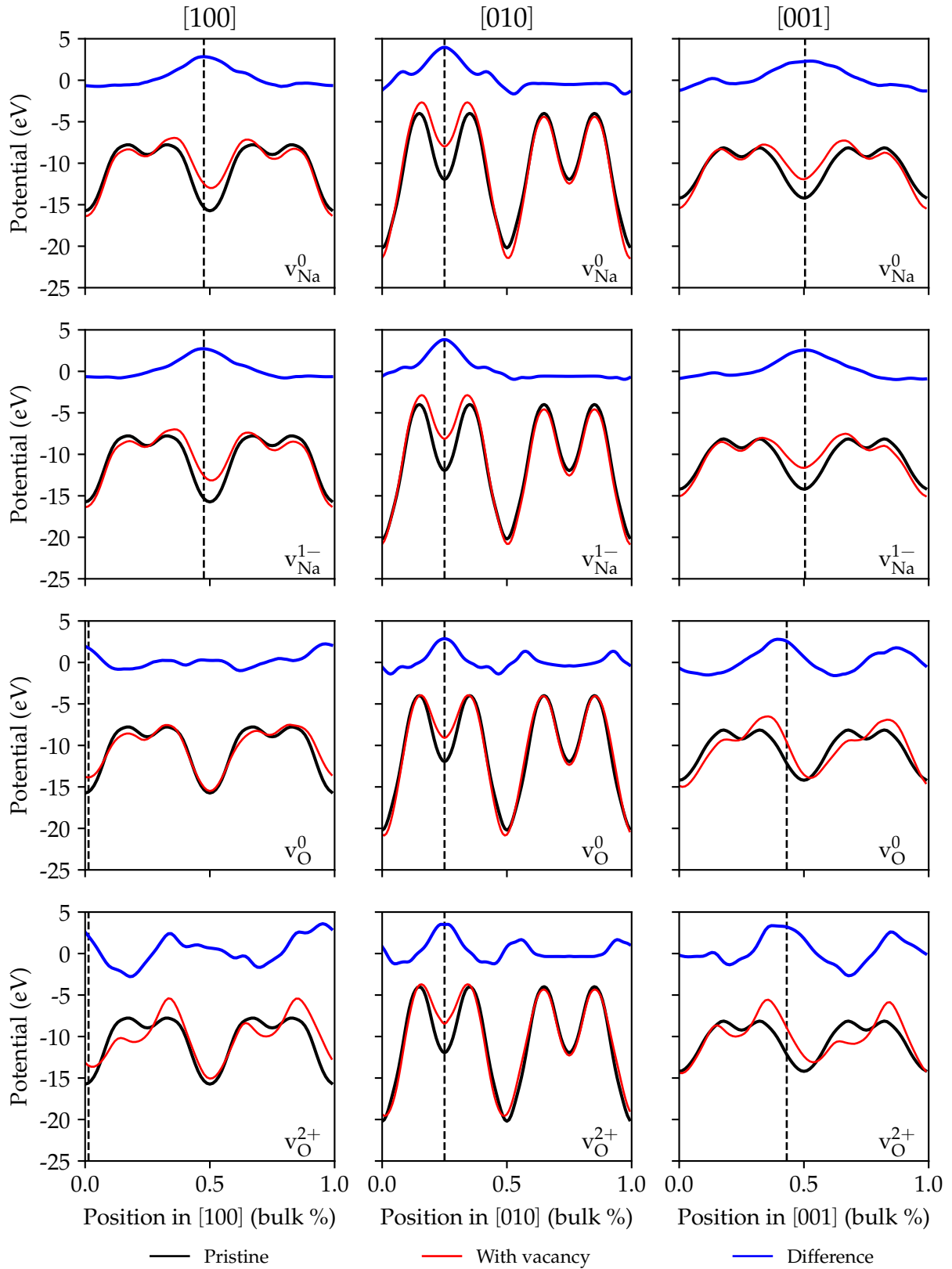


Figure 29 – Formation energies for v_{Na}^0 (a), v_{O}^0 (b), v_{Na}^{1-} (c), v_{O}^{2+} (d) defects simulated on $1 \times 1 \times 1$, $2 \times 2 \times 2$, and $3 \times 3 \times 3$ supercells in O-rich chemical equilibrium. Dashed line shows fitted $\Delta E_f(v_X^q; L)$ scaling equation.

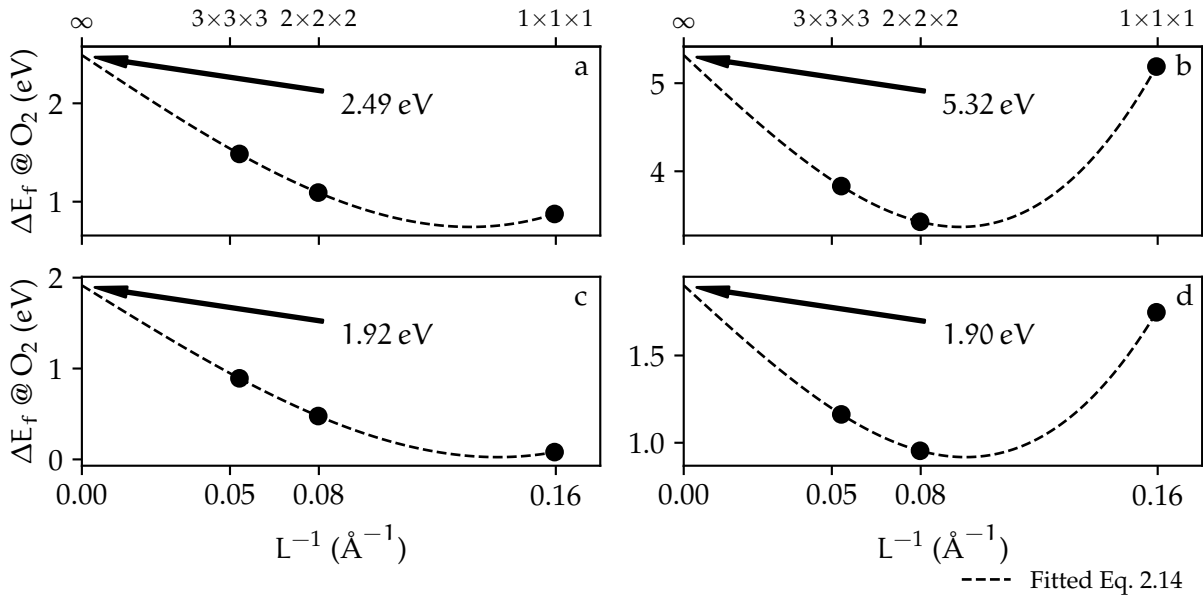


Figure 30 – Calculated v_{Na}^0 and v_{O}^0 formation energies on orthorhombic NaNbO_3 compared to literature values on cubic phase NaNbO_3 and KNbO_3 , and tetragonal LiNbO_3 . Chemical equilibrium notation follows our ternary phase diagram. Values from literature in-between letters have chemical equilibria approximately placed in reference to our work. * ref. [94].

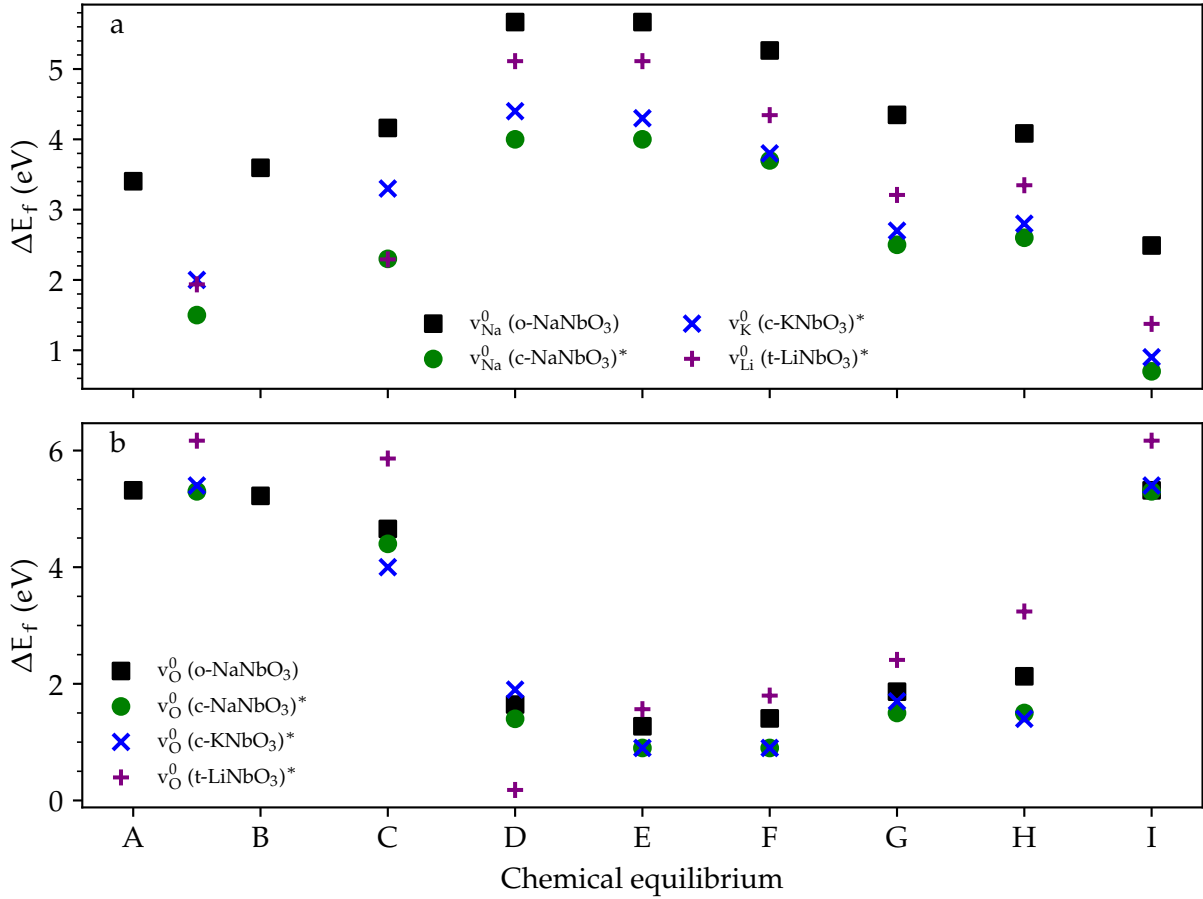


Figure 31 – The change of total charge on the Na (a) and O (b) atoms in each thin film's layer compared to the averaged charge in the relaxed bulk. The surface relaxation imposes minor changes on both species when compared to the Nb changes.

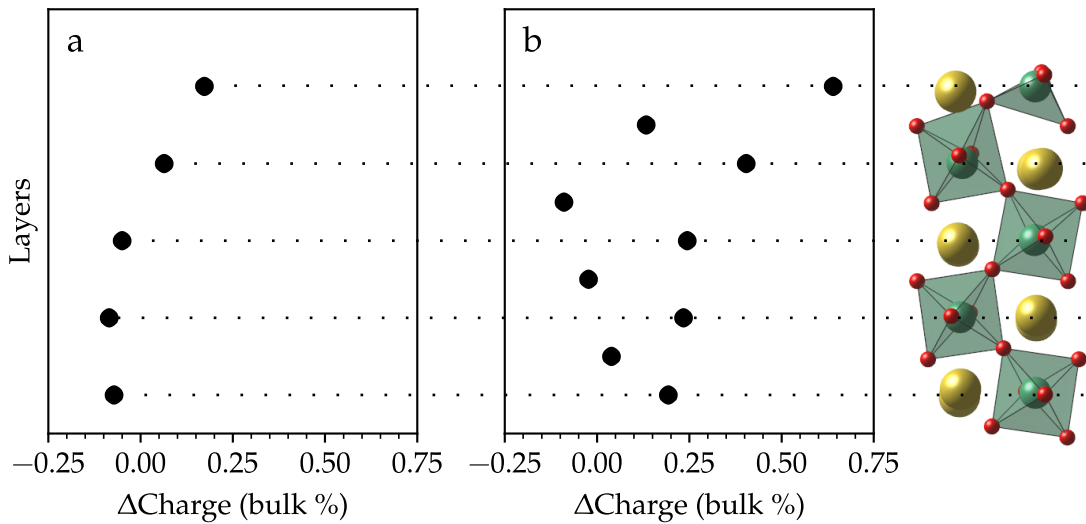


Figure 32 – Internal layers' pDOS of the NaNbO_3 thin film. Region's electronic response is similar to bulk's response.

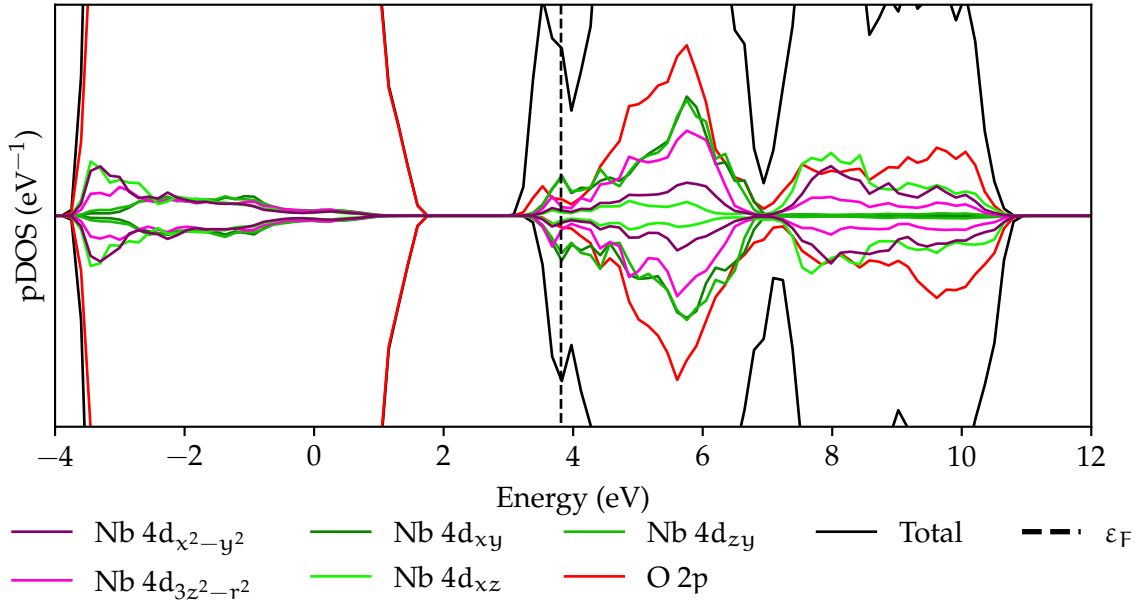


Figure 33 – Layer-averaged charge evolution on Na (a) and O (b) atoms by inducing biaxial strain on the thin film. The lines are for eye-guide only. The comparison is made with the strain-free thin film in Fig. 31. The charge evolution on these atoms is small compared to Nb one.

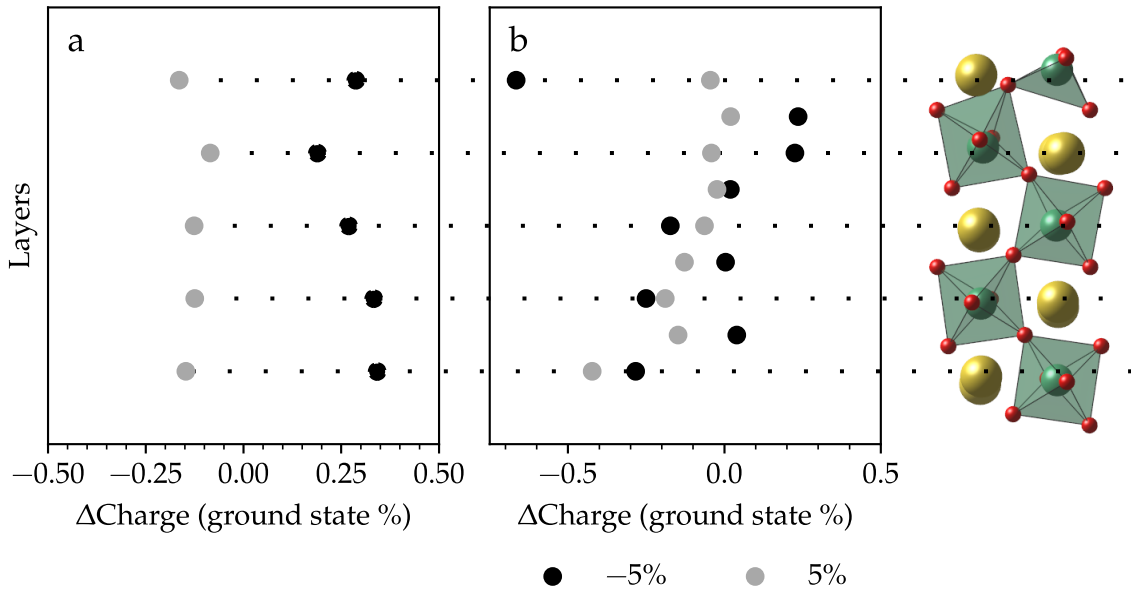


Figure 34 – NaTaO₃ (a, M = Ta) and NaNbO₃ (b, M = Nb) internal regions' pDOS describing their minority contribution to the lowermost antibonding electronic states.

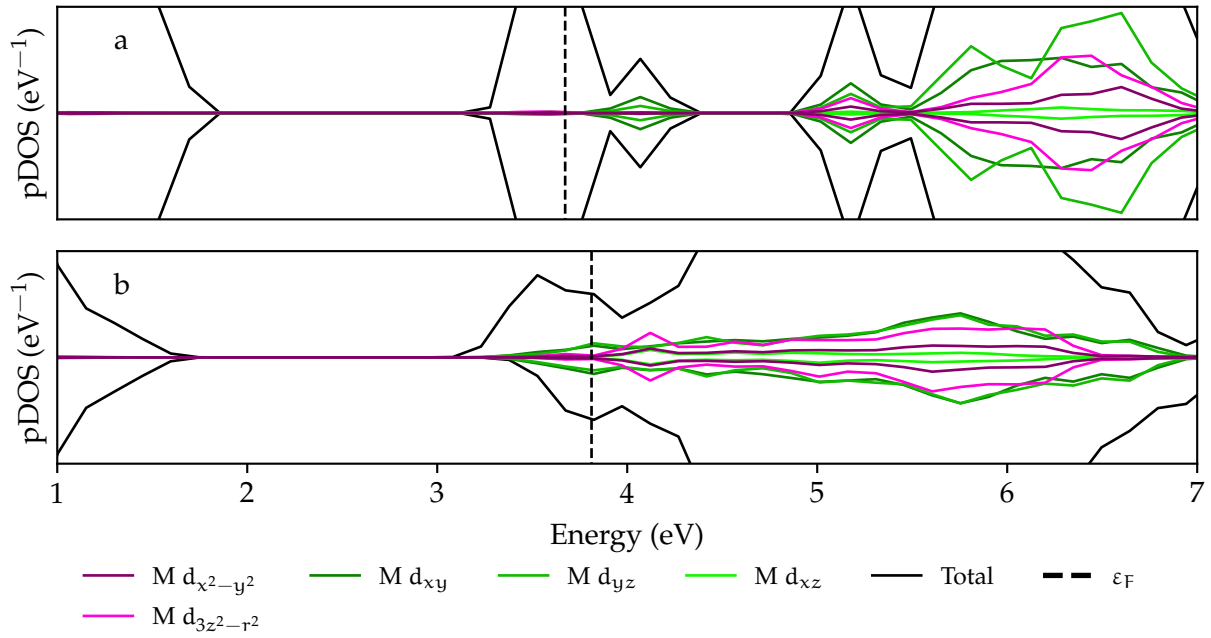
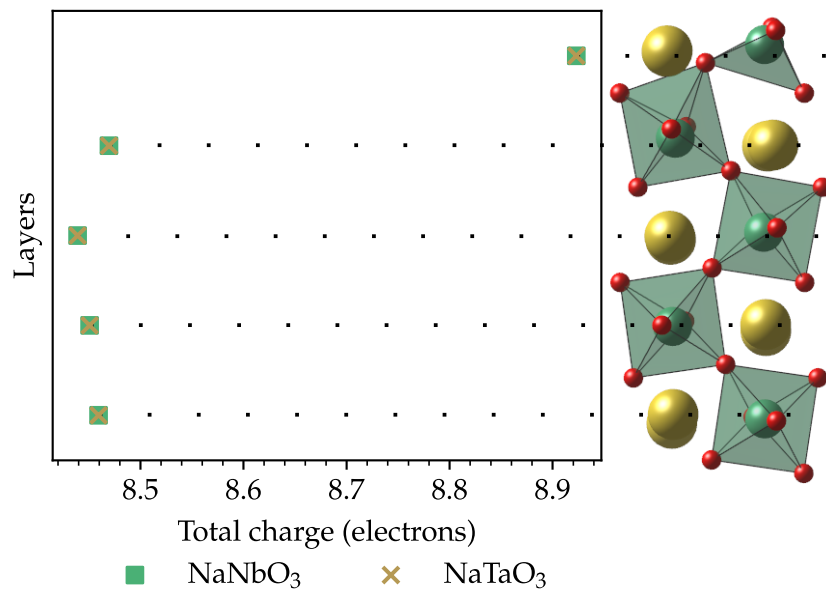


Figure 35 – Layer averaged total charge for the NaTaO₃ and NaNbO₃ thin-films. At right, a schematic half-slab indicating correspondence between Δ Charge values and atomic layers.



APPENDIX B – NUMERICAL CONVERGENCES

Figure 36 – The total energy's variation with the volume for the Pmna crystal of the NaNbO_3 showing the lattice parameters of the relaxed strain-free bulk within the numerical precision.

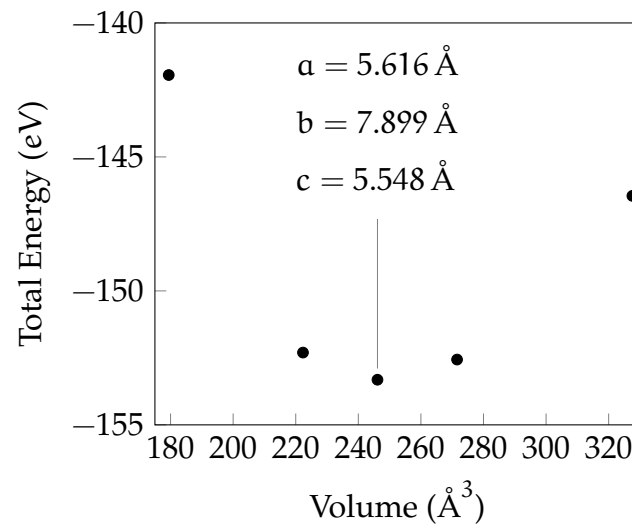


Figure 37 – Total energy convergence of bulk NaNbO_3 in respect to the k-points mesh. The Y axis indicates the position of the changing digit: smaller than -3 ($1 \times 10^{-3} \text{ eV}$) is considered converged.

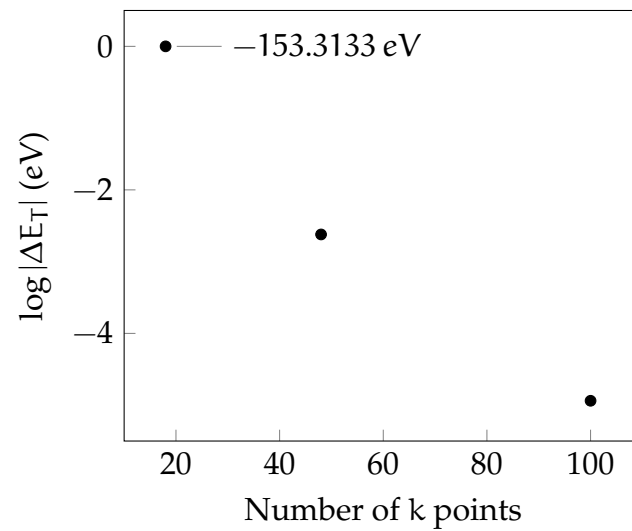


Figure 38 – Energy variation with the k-point change. The lines are for eye-guide only. The Y axis indicates the position of the changing digit: smaller than -3 (1×10^{-3} eV) is considered converged.

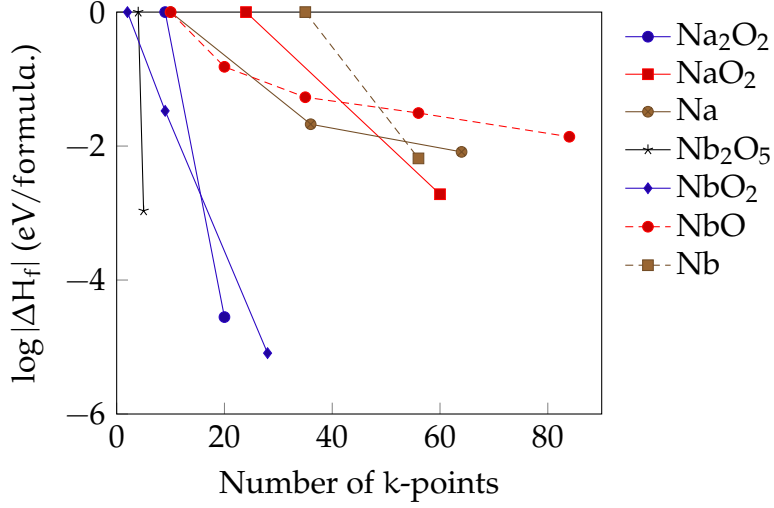


Figure 39 – Single NaNbO_3 conventional cell slab's total energy variation with volume. From minimal point, the supercell's lattice parameters which were considered relaxed within numerical precision.

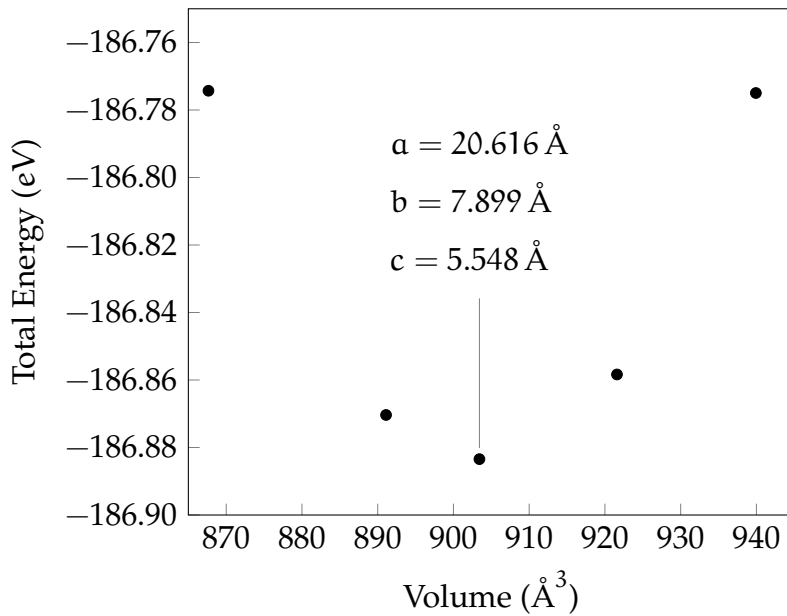


Figure 40 – Three NaNbO₃ conventional cell slab's total energy variation with volume showing the lattice parameters of relaxed strain-free slab within numerical precision.

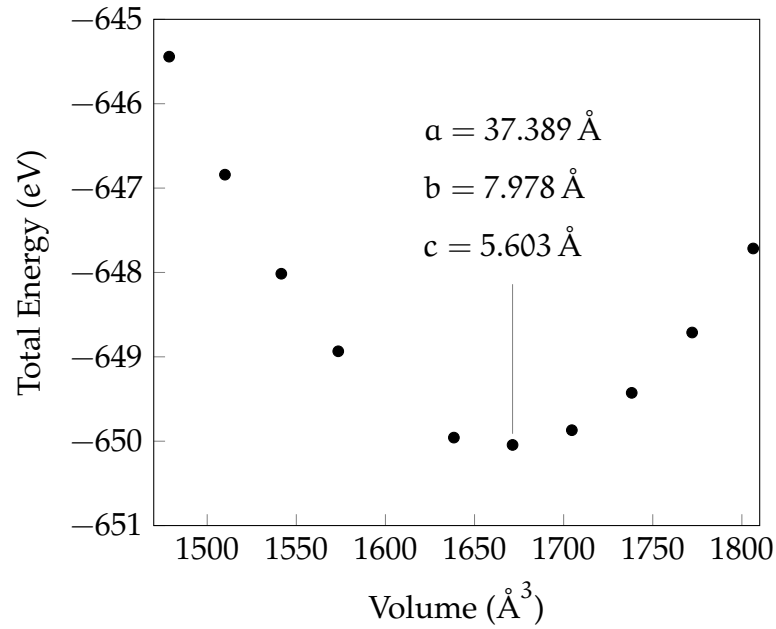


Figure 41 – Five NaNbO₃ conventional cell slab's total energy variation with volume showing the lattice parameters of relaxed strain-free slab within numerical precision.

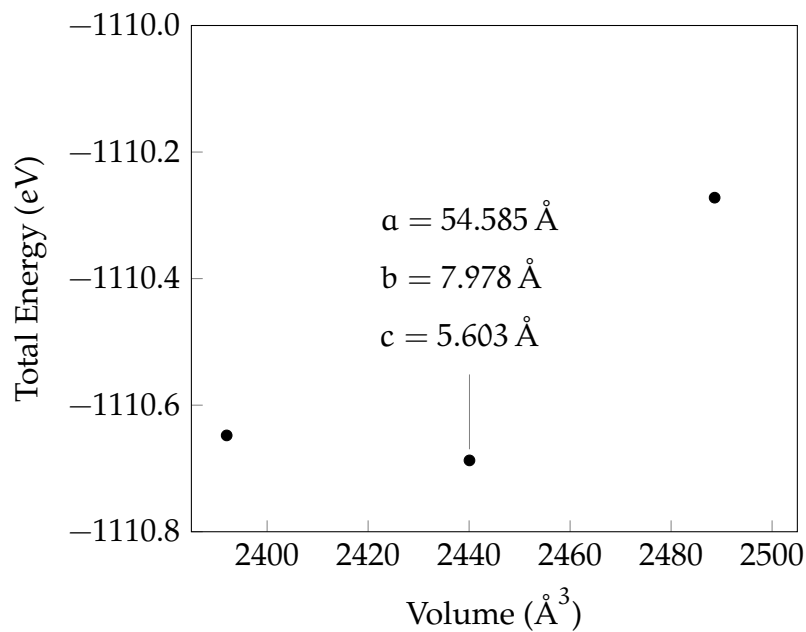


Figure 42 – Three NaTaO₃ conventional cell slab's total energy variation with volume showing the strain-free lattice parameters within numerical precision.

